Mercury

Francis M. McCubbin[1] & Brendan A. Anzures[2,3]

[1]NASA Johnson Space Center, Astromaterials Research & Exploration Science Division, mailcode XI, 2101 NASA Pkwy, Houston TX, 77058, USA (email: francis.m.mccubbin@nasa.gov)

[2]Lunar and Planetary Institute, 3600 Bay Area Boulevard, Houston, TX 77058, USA

[3]Jacobs, NASA Johnson Space Center, Astromaterials Research & Exploration Science Division, mailcode XI, 2101 NASA Pkwy, Houston TX, 77058, USA (email: brendan.a.anzures@nasa.gov)

This is a post print of a book chapter submitted to EarthArXiv that was published in:

Treatise on Geochemistry, 3rd Edition, Volume 7

Editors: Ariel Anbar, and Dominique Weis

Publisher: Elsevier

Year: 2025

Chapter DOI: https://doi.org/10.1016/B978-0-323-99762-1.00109-1

Cite as: McCubbin, F.M. and Anzures, B.A. (2025) Mercury. In: Weis, D. and Anbar, A. (eds.) Treatise on Geochemistry, 3e. vol. 7, pp. 257-287. UK: Elsevier.

Abstract

Data from the Mercury Surface, Space Environment, Geochemistry and Ranging (MESSENGER) spacecraft, the Mariner 10 spacecraft, and decades of ground-based observations have revealed a wealth of information about the geochemistry of Mercury, the inner most planet in our Solar system. These data indicate that Mercury is an endmember among the terrestrial planets with a core mass fraction of ~71–78% of the planet's mass, a surface that is low in Fe and rich in S, and a surface that is darkened by 1–4% graphitic carbon that may have been sourced from an ancient primary flotation crust. Mercury has an interior oxygen fugacity (fO_2) that is more reduced than the other terrestrial planets. In fact, the interior of Mercury is so reduced, the geochemical behavior of the elements on Mercury deviates from the expected behavior based on studies of Earth, Moon, and Mars. Moreover, Mercury is a volatile-rich planet with moderately volatile element abundances similar to Mars and possibly enriched relative to Earth. The origin of Mercury's endmember status is still an open question, but there are two broad classes of hypotheses for the origin of Mercury, including 1) impact erosion models consisting of either a single giant mantle-stripping impact or series of smaller impacts that preferentially removed silicate material from Mercury without re-accretion; and 2) formation of Mercury from highly reduced and broadly chondritic metal-rich precursor materials that are not well represented by chondritic meteorites. Both of these formation models have highly contrasting implications for the thermochemical evolution of Mercury and its bulk composition. However, from the data available, both models remain viable. Many open questions about Mercury's geochemistry remain unanswered. These questions require additional experimental and modeling work that can be completed today, but they also require the continued exploration of planet Mercury. The European Space Agency's BepiColombo spacecraft will reach orbital insertion around Mercury in late 2025, and it has a suite of geochemical instruments that will gather data from across the surface of Mercury. Looking beyond BepiColombo, a Mercury lander could provide detailed insights into the surface of Mercury that are not possible from orbit, and studies of samples, either through the identification of a meteorite from Mercury or from a Mercury sample return mission would revolutionize our understanding of Mercury's geochemistry.

Introduction

Mercury is the closest planet to the Sun, and the earliest known reference to this planet by human beings dates back to Mesopotamia in the 7th century BCE (Prockter and Bedini, 2010). The English name Mercury is derived from the Roman messenger god Mercurius, which is the Roman equivalent of the Greek god Hermes (Prockter and Bedini, 2010). Consequently, references to something from Mercury are often expressed as hermean or mercurian, and we have adopted the former throughout this text. The planet Mercury was first observed through a telescope, contemporaneously, in the 17th century by Galileo Galilei and Thomas Harriott. That event marked a key advancement in our ability to study Mercury as an object of scientific interest, and that interest persists to this day. Centuries of study have led to Mercury being dubbed the "enigmatic innermost planet" in our solar system (Solomon, 2003). In fact, Mercury has perplexed scientists at least as early as the 19th Century when it was discovered that the rate of Mercury's precession of the perihelion deviated from that predicted by Newton's law of universal gravitation. It was not until the early 20th Century, with the formulation of Einstein's general theory of relativity (Einstein, 1915), that Mercury's rate of precession of the perihelion could be explained quantitatively. In the 20th and 21st Centuries, the study of Mercury continued with both telescopic and spacecraft observations, and from those observations, the portrait of a planetary endmember in our solar system emerged (Ebel and Stewart, 2018; McCoy et al., 2018; Nittler et al., 2018; Solomon, 2003; Taylor and Scott, 2003). The observed characteristics of Mercury have expanded the parameters of what we know to be possible for the physicochemical nature of terrestrial planets in our solar system, and it serves as an important test for both dynamical and chemical models of terrestrial planet formation (e.g., Asphaug and Reufer, 2014; Benz et al., 2007; Ebel and Stewart, 2018; Vander Kaaden et al., 2019). Furthermore, Mercury represents an important analog for exoplanetary systems as some exoplanets have characteristics that are more similar to Mercury than other terrestrial planets in our solar system (e.g., Lam et al., 2021; Santerne et al., 2018). In this contribution, we summarize what is known about hermean geochemistry, and we highlight some of the important questions that can only be answered through continued investigation and exploration of Mercury.

Much of our knowledge about Solar System geochemistry comes from the study of astromaterials, either collected and brought to Earth during sample return missions or delivered naturally to Earth as meteorites or cosmic dust. We have yet to identify a piece of Mercury amongst

the world's meteorite collections, so everything we know about hermean geochemistry has come from remote sensing data, either telescopic observations or data collected from spacecraft. Ground-based telescopic observations of Mercury have occurred since the invention of the telescope, but such observations are often challenging given the proximity of Mercury to the Sun. The primary types of ground-based telescopic observations that have informed our knowledge of hermean geochemistry include radar measurements of Mercury (Ash et al., 1967; Ash et al., 1971), measurements of the spectral reflectance of Mercury's surface in the ultraviolet, visible, and near infrared (UV-VIS-NIR) (e.g., Blewett et al., 1997; McCord and Adams, 1972; McCord and Clark, 1979; Vilas, 1988; Vilas and McCord, 1976), and measurements of thermal emission in the mid-IR (Sprague et al., 2009; Sprague et al., 1994; Sprague and Roush, 1998; Vilas, 1988). These ground-based observations provide key insights into Mercury's density, as well as some constraints on the surface composition and mineralogy.

The first spacecraft to explore Mercury was Mariner 10, which made three flybys of Mercury in 1974–1975. The Mariner 10 spacecraft was equipped with a suite of instruments, including a magnetometer that detected a weak global magnetic field on Mercury (Ness et al., 1974). The instruments on Mariner 10 measured Mercury's gravitational field and determined that the density of Mercury matched the density determined by earlier ground-based observations (Howard et al., 1974). Mariner 10 was also equipped with two cameras that captured color images of the surface of Mercury and revealed a heavily cratered terrain on the portion of the surface (i.e., ~45%) that could be imaged by Mariner 10 (Murray et al., 1974). Mariner 10 had a UV airglow spectrometer and UV occultation spectrometer that discovered a very thin atmosphere on Mercury with a total surface pressure of less than 2×10^{-9} mbar (Broadfoot et al., 1974). Despite the advancement of Mariner 10 data over telescopic observations, a large majority of the planet remained unexamined.

It was another 33 years before Mercury was visited by another spacecraft. In 2008, the MErcury Surface, Space ENvironment, GEochemistry and Ranging (MESSENGER) spacecraft completed its first of three flybys of Mercury before orbital insertion in 2011. The MESSENGER spacecraft was equipped with a suite of instruments that could be used to understand hermean geochemistry, including an X-Ray spectrometer (XRS) and combined gamma-ray and neutron spectrometers (GRNS) that were capable of chemical mapping on the surface, a combined UV-VIS-NIR spectrometer to analyze both surface mineralogy and exospheric species, a dual imaging

system for monochrome, color, and stereo imaging for both wide and narrow fields of view, an energetic particle and plasma spectrometer to analyze charged species in the magnetosphere, a magnetometer, and a laser altimeter (Solomon et al., 2001). The data from these instruments revolutionized our understanding of hermean geochemistry and Mercury as a whole. The MESSENGER mission collected data until its propellants were depleted and the spacecraft made a planned descent into the surface of Mercury in 2015 (Solomon and Byrne, 2019). In this work we synthesize our knowledge of hermean geochemistry from decades of observations, and we look with anticipation of forthcoming results from BepiColombo as it enters orbital insertion around Mercury in late 2025, as well as future endeavors to study and explore Mercury.

Hermean Geochemistry from Observations

The primary basis of modern geochemistry is built on an understanding of several key intrinsic properties of the elements within natural systems, namely volatility, compatibility, and affinity. Element volatility describes the relationship between temperature and the physical state (solid, liquid, gas) of a particular element, and volatility is most commonly expressed through an element's condensation temperature (i.e., the temperature at which 50% of an element would condense from a vapor of solar composition at nebular pressure; Lodders, 2003), although other measures of volatility are also used (e.g., Albarède et al., 2015; Wood et al., 2019). Geochemical compatibility describes whether a particular element is more likely to partition into a silicate melt or remain in a solid residue during partial melting (e.g., Hofmann, 1988). Geochemical affinity defines the natural tendencies of element bonding within natural systems (Goldschmidt, 1937). For example, most elements are characterized as lithophile (rock-loving; tendency to bond with O^{2-}), siderophile (iron-loving; tendency to bond within metallic phases), chalcophile (sulfur-loving; tendency to bond with S^{2-}), or atmophile (gas-loving; tendency to exist in a gas phase). All of these properties are used to build a geochemical intuition of how elements are distributed within a planetary body during its thermochemical evolution, including processes such as planetary differentiation and secondary crust production. However, it is important to acknowledge that much of this intuition is built from studying the Earth and meteorites, and the physicochemical conditions under which Mercury operates may not be encompassed by the conditions from which our baseline geochemical intuition has developed.

Mercury's core fraction

With a radius of ~2440 km, Mercury is the smallest of the terrestrial planets, yet it has an anomalously high density for its size (mean density of ~5.4 g/cm^3; Howard et al., 1974). This high density is the result of its large core that makes up ~71–78% of the planet's mass (computed from data in Margot et al., 2019), which is a larger core fraction than any of the other terrestrial planets in our Solar System, the Moon, or even 4-Vesta (Figure 1). Data returned from the Mariner 10 and MESSENGER missions indicate that Mercury has a weak magnetic field (Hauck and Johnson, 2019; Ness et al., 1974), which has been used to infer that Mercury's metallic core may be partially molten (Hauck II et al., 2013; Margot et al., 2007). The origin of Mercury's high metal/silicate ratio is thought to be key to understanding the planet's origin (e.g., Siegfried and Solomon, 1974), and it is one of the primary features that define Mercury as an endmember terrestrial planet.

Mercury's surface composition

Before the arrival of MESSENGER at Mercury, orbital and telescopic observations indicated that Mercury iss distinct from the other terrestrial planets. The surface lacked spectral absorption features in the UV-VIS region, so direct constraints on surface mineralogy were not possible. However, a similar lack of spectral absorption features in the NIR at 1 μm (i.e., diagnostic of FeO (Fe^{2+}) in silicate mineral phases) led to predictions that Mercury's surface has ≤2–3 wt.% FeO in silicates (Blewett et al., 1997; Izenberg et al., 2014; McCord and Clark, 1979; Riner et al., 2010; Robinson and Lucey, 1997; Robinson and Taylor, 2001; Vilas, 1988). Mercury also has a low albedo that is consistent with a prevalent opaque component on the surface (Denevi and Robinson, 2008; Robinson et al., 2008). The identity of the opaque component was hypothesized to be Fe-Ti oxides since they could darken the surface without exhibiting a 1 μm absorption feature (Denevi and Robinson, 2008; Robinson et al., 2008), but exotic mechanisms were needed for abundant Fe-rich Fe-Ti oxide phases to coexist with silicate phases that do not exhibit a 1 μm absorption feature (Denevi et al., 2009; Riner et al., 2010). With the arrival of MESSENGER at Mercury, quantitative constraints could be established on the surface composition, and better inferences about surface mineralogy were subsequently possible.

The composition of Mercury's surface was determined by MESSENGER using X-ray and gamma ray spectroscopy, yielding estimates for the abundance of Si, Ti, Al, Cr, Fe, Mn, Mg, Ca, Na, K, S, Cl, C, O, U, and Th (Cartier et al., 2020; Evans et al., 2015; Evans et al., 2012; Frank et al., 2017; Klima et al., 2018; McCubbin et al., 2017; Nittler et al., 2023; Nittler et al., 2018; Nittler

et al., 2011; Peplowski et al., 2011; Peplowski et al., 2014; Peplowski et al., 2016; Peplowski et al., 2015a; Peplowski et al., 2012; Weider et al., 2015; Weider et al., 2014; Weider et al., 2012). The global coverage and analysis footprint for each element at each location on Mercury is different and dependent upon several factors including detection sensitivity and resolution of the instrument and global latitude (due to highly elliptical orbit of the MESSENGER spacecraft around Mercury). Additionally, for XRS data in particular, data collection was dependent on energy required to produce X-rays (i.e., quiet Sun conditions could produce X-rays for Al, Mg, and Si, but solar flares were needed to generate X-rays of high mass elements like S, Ca, Cr, Ti, Fe, and Mn), among other factors (Evans et al., 2012; Nittler et al., 2020; Nittler et al., 2011; Peplowski et al., 2011). The details of these analyses are covered at depth in other reviews (e.g., Evans et al., 2012; Nittler et al., 2018; Nittler et al., 2020), so we focus here on a summary of the geochemical data that were obtained from MESSENGER. The global average surface composition of Mercury from MESSENGER data is provided in Table 1.

The orbital path of MESSENGER was highly elliptical, with a closest pass at the north pole and furthest pass at the south pole (Solomon et al., 2001). This orbit allowed for higher spatial resolution measurements of surface elemental abundances in the northern hemisphere, with the highest resolution at the north pole. In contrast, surface measurements of the southern hemisphere yield a hemispheric average composition. The higher resolution northern hemisphere measurements exhibit spatial heterogeneities in the distribution of elements across the surface of Mercury (Evans et al., 2012; Nittler et al., 2020; Nittler et al., 2011; Weider et al., 2015; Weider et al., 2012). These heterogeneities were coupled, in some cases, with morphological surface features and/or variations in neutron absorption properties of the surface (using data from the neutron spectrometer portion of the MESSENGER GRNS instrument) to establish distinct geochemical terranes or deposits on Mercury (Lawrence et al., 2017; Peplowski et al., 2015b; Peplowski and Stockstill-Cahill, 2019; Vander Kaaden et al., 2017; Weider et al., 2015; Figure 2). These terranes and deposits have distinct geochemistry, inferred mineralogy, and inferred geologic origins (McCoy et al., 2018; Namur and Charlier, 2017; Peplowski and Stockstill-Cahill, 2019; Vander Kaaden et al., 2017). Peplowski et al. (2015b) identified three terranes based on neutron spectroscopy (NS) and Mg/Si values; Weider et al. (2015) defined six terranes on the basis of Mg/Si versus Al/Si; Vander Kaaden et al. (2017) identified nine geochemical regions consisting of deposits and terranes on the basis of GRS and XRS data, and Lawrence et al. (2017) identified

an additional terrane by NS added onto the three identified by Peplowski et al. (2015b). McCoy et al. (2018) consider five geochemical terranes on the basis of a terrane being 1) spatially continuous, 2) geochemically distinct from the crustal average, and 3) spatially extensive with at least 1000 km width. Smaller distinct geochemical units are thus classified as deposits. For example, a large pyroclastic feature that is Northeast of Rachmaninoff basin is an example of a distinct deposit (Vander Kaaden et al., 2017; Weider et al., 2016). The distribution and locations of eight terranes and deposits are provided in Figure 2. The intercrater plains and highly cratered terrain (IcP-HCT) represents the space that is not occupied by other geochemical terranes and deposits that reside primarily in the northern hemisphere (Peplowski and Stockstill-Cahill, 2019; Vander Kaaden et al., 2017; Weider et al., 2015; Figure 2). The IcP-HCT Terrane is combined with the southern hemisphere to represent an intermediate terrane after Vander Kaaden et al (2017). Compositions for eight different terranes and deposits are summarized in Table 2.

Volatile elements in the hermean interior

Of the elements measured on the surface of Mercury by MESSENGER, Na, K, Cl, C, and S are considered volatile elements and can be used to constrain the degree of volatile depletion in the hermean interior. In particular, planetary surface measurements of K/U and K/Th ratios provide a rough estimate on the magnitude of volatile depletion in the bulk silicate portion of a planet. The magnitude of volatile depletion within a planetary body is considered to be a key observation in determining a planet's origin because it can provide clues to the thermal history of the parent body and/or the thermal history of its building blocks (e.g., Halliday 2013; Braukmüller et al., 2018; Boyce et al., 2024). Potassium, thorium, and uranium are all large-ion lithophile elements (LILE), which are known to be highly incompatible in the solid residue during partial melting of silicates (Jochum et al., 1983; McLennan, 2003). Consequently, the ratios of these elements are not likely to change during melting processes, and the surface ratios can be presumed to represent the bulk silicate portion of the planet (McCubbin et al., 2012; Peplowski et al., 2011; Taylor et al., 2006; Taylor and McLennan, 2008). Furthermore, U and Th are both refractory elements (i.e., 50% condensation temperatures of 1610 K and 1659 K, respectively; Lodders, 2003) and K is a moderately volatile element (K has a 50% condensation temperatures of 1006 K; Lodders, 2003), so comparison of K/Th and K/U ratios with chondritic K/Th and K/U ratios allows one to determine volatile depletion of a planetary surface relative to chondrite. There are many possible

combinations of incompatible refractory-volatile element ratios that could serve this same purpose, but K/U and K/Th are primarily used because these three elements are radioactive and naturally emit gamma rays that can be detected by orbital gamma ray spectrometers, making this a high-fidelity measurement that is accessible to a wide array of spacecraft missions (e.g., Boynton et al., 2007; Jolliff et al., 2000; Peplowski, 2016; Peplowski et al., 2011; Prettyman et al., 2006).

Mercury has an average surface K/Th ratio of 5700 ± 2600 (Peplowski et al., 2012) and surface K/U ratio of 12800 ± 3700 (Peplowski et al., 2011), which are lower than CI chondrite by a factor of ~3 and ~5, respectively (Lodders and Fegley, 1998). The depletions relative to CI chondrite are similar to the other terrestrial planets, with the magnitude of Mercury's volatile depletion being between that of Earth and Mars (Figure 3). Furthermore, the northern hemisphere K/Cl ratio of Mercury's surface is 1.22 (Evans et al., 2015), which is similar to the CI chondrite K/Cl ratio of 1.3 (Lodders and Fegley, 1998). Although both K and Cl are moderately volatile incompatible elements, Cl is more susceptible to loss during planetary accretion compared with S, K, and Na (Sharp and Draper, 2013). Consequently, the K/Cl ratio can provide additional constraints on the volatile inventory of a planetary body. The chondritic K/Cl ratio on Mercury indicates that moderately volatile elements do not show evidence of differential volatile depletion at Mercury's surface and further supports evidence that Mercury has a volatile inventory comparable to the other terrestrial planets. The global average Na abundance on the surface of Mercury is 3 ± 0.25 wt.%, which results in a global Na/K ratio of 23.3 ± 4.7. This value is K-depleted relative to CI chondrite (Na/K = 9 for CI chondrite; Lodders and Fegley, 1998); moreover, Na is more compatible than K, so Na is likely retained to a greater extent than K within the mantle (Hofmann, 1988).

Two of the most striking geochemical discoveries about the surface of Mercury during the MESSENGER mission were the elevated abundance of S and C. The average S/Si ratio determined by MESSENGER for the hermean surface ranges from 0.076 (XRS; Nittler et al., 2018) to 0.092 (GRS; Evans et al., 2012), with a full range in S/Si of 0.02–0.16 (Nittler et al., 2020). The average S/Si ratio corresponds to an average of 1.9–2.3 wt.% S for the hermean surface on the basis of an average surface Si abundance of 25 wt.% (Evans et al., 2012). The full range of S/Si ratios corresponds to a range in surface S of 0.5–4.0 wt.%. As discussed in the following section, the elevated S abundance on Mercury's surface has important implications for the oxygen fugacity of

the hermean interior, but it also further supports other observations that moderately volatile elements are retained at the surface of Mercury.

On the basis of MESSENGER GRS, the surface of Mercury has a global average of 1.4 ± 0.9 wt.% C (Peplowski et al., 2015a), with local enrichments of 2.5 wt.% above the global average within low-reflectance material (LRM) and up to 4 wt% above the global average in some places (Klima et al., 2018; Peplowski et al., 2016). The correlation between C and low-reflectance material is consistent with graphitic carbon being the primary darkening agent (i.e., opaque component) on the surface of Mercury, as proposed by Murchie et al. (2015). In fact, graphite became the leading hypothesis as the primary opaque phase responsible for Mercury's low surface albedo after XRS measurements of the surface indicated low abundances of Fe and Ti, ruling out an earlier hypothesis that Fe-Ti oxides were the primary darkening agent (Murchie et al., 2015; Nittler et al., 2011; Weider et al., 2014). The origin of the graphitic carbon is hypothesized to be the remnants of an ancient primary flotation crust that formed on a hermean magma ocean and that lies at the base of the younger secondary volcanic crust (Vander Kaaden and McCubbin, 2015). This hypothesis is supported by MESSENGER NS data that show global-scale C-enrichments within the LRM-rich rims of craters that are likely sourced from depth (Peplowski et al., 2016). The abundance of C and its potential source as a primary crust may be unique among the terrestrial planets and could have important implications for the thermochemical evolution of Mercury and its bulk composition (e.g., Lark et al., 2023; Vander Kaaden et al., 2020).

Oxygen fugacity of the hermean interior

In addition to K/U and K/Th ratios, one of the key observations for understanding the geochemistry of a planetary surface is the abundance of Fe (Dreibus et al., 1977; McDonough and Sun, 1995; Morgan and Anders, 1980; Taylor, 2013; Taylor and Wieczorek, 2014). The abundance of Fe at the surface of a planet can provide constraints on the oxygen fugacity (fO_2) of the silicate portion of that planet, particularly when this information is coupled with knowledge that the planetary body is differentiated and has a metallic core. Although oxygen fugacity defines the partial pressure of O_2 in a system, in a more practical sense, it affects the valence states of the elements in that system, which in turn can change their volatility and compatibility (e.g., Cartier and Wood, 2019; Malavergne et al., 2007a; Malavergne et al., 2007b; McCubbin et al., 2012; McCubbin et al., 2017; Papike et al., 2005; Steenstra et al., 2019; Steenstra et al., 2016; Zolotov,

2011; Zolotov et al., 2013). Information about fO_2 can be gleaned from surface Fe abundances for several reasons 1) Fe is the ninth most abundant element in the Solar System (Lodders, 2003; Palme et al., 2014), making its abundance detectable without high-precision measurements; 2) The oxidation state of Fe changes from Fe^{3+} to Fe^{2+} to metallic Fe (Fe^0) over a range of fO_2 that is intrinsic to many planetary bodies (Ehlmann et al., 2016; Herd, 2008; Kelley and Cottrell, 2009; McCubbin et al., 2012; Wadhwa, 2008); 3) Fe is inferred to be the primary constituent in planetary metallic cores (McDonough, 2003; Righter and Drake, 1996); 4) metallic Fe and FeO are efficiently separated during partial melting, given the immiscibility between silicate and metallic melts and the large density contrast between metallic phases and silicate melt (e.g., McCubbin et al., 2017; Taylor and McLennan, 2008); and 5) Fe has a solid-melt partition coefficient of approximately one (Hofmann, 1988; Taylor and McLennan, 1985), so the surface Fe abundance is expected to be broadly reflective of its silicate source at depth (McCubbin et al., 2012; Robinson and Taylor, 2001). The latter point assumes that the surface of the planet is comprised of a volcanic secondary crust because partial melting of a mantle source would fractionate FeO from Fe-rich metal that was not efficiently separated during planetary differentiation. Importantly, the latter point is true for Mercury (Byrne et al., 2016; Byrne et al., 2018; Head et al., 2009; Robinson and Lucey, 1997; Thomas et al., 2014b).

The surface of Mercury has an average Fe/Si ratio of 0.06 (XRS; Nittler et al., 2020) to 0.077 (GRS; Evans et al., 2012), with a full range in Fe/Si of 0.02–0.10 (Nittler et al., 2020). The average Fe/Si ratio corresponds to an average of 1.5–2 wt.% Fe (or 2-2.5 wt.% FeO) for the hermean surface on the basis of an average surface Si abundance of 25 wt.% (Evans et al., 2012). This Fe abundance is consistent with many of the pre-MESSENGER predictions of surface FeO abundance (Blewett et al., 1997; McCord and Clark, 1979; Riner et al., 2010; Robinson and Lucey, 1997; Robinson and Taylor, 2001; Vilas, 1988). The full range of Fe/Si ratios corresponds to a range in surface Fe of 0.5–2.5 wt.%. Assuming that all Fe was once Fe^{2+} (i.e., FeO) dissolved in a silicate melt, this range in average FeO (0.64–3.2 wt.% FeO) implies that the maximum fO_2 for Mercury's interior is at a value of 3.1 log units below the fO_2 of the Iron-Wüstite (IW) reaction (i.e., $Fe^0 + ½O_2 \leftrightarrow FeO$), using the methods reported by McCubbin et al. (2012). This value is considered an upper limit based on the endmember activity coefficients used for FeO (1.3; from O'Neill and Eggins, 2002) and Fe metal (0.85 computed from Wade et al., 2012) and the

assumption that all surface Fe was once bonded to oxygen. The full range of fO_2 implied by the range in FeO abundances on the hermean surface is 4.9 to 2.9 log units below IW.

Another observation in support of Mercury being highly reduced is the elevated abundance of S on the hermean surface. Although sulfide solubility in silicate melts is limited to a few thousand parts per million (ppm) in typical planetary basalts (Mavrogenes and O'Neill, 1999; Wallace and Carmichael, 1992) over the fO_2 range of IW–2 to that defined by the fayalite-magnetite-quartz (FMQ) reaction (i.e., $3Fe_2SiO_4 + O_2 \leftrightarrow 3SiO_2 + 2Fe_3O_4$), the solubility of sulfide in silicate melts reaches values approaching 10 wt. % at fO_2 values below about IW–3 (Malavergen et al., 2014; Anzures et al., 2020; McCubbin et al., 2012; Namur et al., 2016a). On the basis of the sulfide capacity at sulfide saturation (SCSS) of silicate melts, Namur et al. (2016a) estimated the fO_2 of hermean lavas, and hence the interior of Mercury, to be at IW–5.4 ± 0.4. This SCSS-based fO_2 is even lower than estimates on the basis of Fe at the surface of Mercury and further reinforces the case that Mercury is a highly reduced terrestrial planet. The abundances of Cr on the surface of Mercury have also been used to constrain the fO_2 of Mercury's interior, and those efforts resulted in values that are broadly consistent with the range in possible fO_2 yielded by the abundances of Fe and S on the surface (Nittler et al., 2023).

MESSENGER GRS measurements of the surface O/Si ratio (estimated to be 1.2 ± 0.1) indicate that O is depleted on the surface of Mercury relative to the surfaces of other planetary bodies and of meteorites (McCubbin et al., 2017). Although this O/Si ratio cannot be used as a direct estimate of fO_2, mass balance calculations indicate that the surface O/Si (estimated to be 1.2 ± 0.1) is insufficient for all the other measured elements to be accounted for as oxides and sulfides, implying that the surface of Mercury may be comprised of 12–20% Si-rich Fe-bearing alloys (McCubbin et al., 2017). The formation of such alloys through magmatic processes would imply an fO_2 of lavas from IW–8.7 to IW–12.1 (McCubbin et al., 2017). However, this low O/Si ratio can be explained through secondary processes at the surface involving graphite-melt smelting reactions on the airless surface where O is lost by the oxidation of graphite to make C-O gas species, resulting in reduction of the residual melt and formation of metals (Iacovino et al., 2023; McCubbin et al., 2017) as the fO_2 of the graphite-CO (GCO) reaction (i.e., $C + ½O_2 \leftrightarrow CO$) is highly dependent on pressure (French and Eugster, 1965; Hirschmann and Withers, 2008; Li et al., 2017; McCubbin et al., 2017; Saxena and Fei, 1987). This process is made possible by the

ubiquitous presence of graphite in Mercury's crust, which is hypothesized to be the globally distributed opaque component on the hermean surface (Klima et al., 2018; Murchie et al., 2015; Peplowski et al., 2016; Peplowski et al., 2015a; Vander Kaaden and McCubbin, 2015). Thus, the low O/Si ratio on the surface of Mercury likely represents a secondary process and does not reflect the fO_2 of Mercury's interior.

A preponderance of evidence points to Mercury having a highly reduced interior in the range of 3 to 6 log units below the IW buffer. In fact, the upper limit fO_2 is about two orders of magnitude more reducing than the crusts and upper mantles of any other terrestrial planets (Cartier and Wood, 2019; Ehlmann et al., 2016; McCubbin et al., 2017; Figure 4), and the lower end overlaps with some highly reduced meteorites, including the aubrites and enstatite chondrites (Casanova et al., 1993; Fogel et al., 1989; Keil, 2010; Udry et al., 2019; Wilbur et al., 2022; Figure 4). Oxygen is the primary element that defines a lithophile affinity, so the geochemical affinities of elements on Mercury could deviate from those expected on the basis of terrestrial systems. Furthermore, such shifts in geochemical affinity have been demonstrated in numerous experimental and natural systems at low fO_2 (Boujibar et al., 2019; Ebel and Sack, 2013; Keil, 2010; McCoy et al., 1999; Steenstra et al., 2020a; Steenstra et al., 2020b; Steenstra and van Westrenen, 2020; Udry et al., 2019; Vander Kaaden and McCubbin, 2016; Wilbur et al., 2022; Wohlers and Wood, 2015, 2017; Wood and Kiseeva, 2015).

Portrait of a geochemical endmember emerges

The measurements of Fe abundances, K/Th, and K/U ratios, coupled with decades of observations from ground-based telescopes and orbital observations, all indicate that Mercury is geochemically enigmatic and a geochemical endmember among the terrestrial planets in our Solar System. Mercury has the largest core mass fraction (Figure 1) and is the most reduced of the terrestrial planets (Figure 4). However, it has an inventory of volatile elements that is similar to other terrestrial planets (Figure 3) and may even be enriched in volatiles relative to Earth. Models for the origin and evolution of Mercury need to account for all of these observations.

Some Mercury formation models have been described at length in earlier volumes of this chapter (McCoy and Nittler, 2014; Taylor and Scott, 2003) and in more recent reviews (Ebel and Stewart, 2018), but the remaining plausible hypotheses are summarized here for reference. Two broad classes of hypotheses for the origin of Mercury's high metal-silicate ratio include: 1) impact

erosion models consisting of either a single giant mantle-stripping impact or series of smaller impacts that preferentially removed silicate material from Mercury without re-accretion (Asphaug and Reufer, 2014; Benz et al., 2007; Benz et al., 1988; Cameron et al., 1988; Ebel and Stewart, 2018; Helffrich et al., 2019; Smith, 1979; Wetherill, 1988); and 2) formation of Mercury from highly reduced and broadly chondritic metal-rich precursor materials that are not well represented by chondritic meteorites (Cartier and Wood, 2019; Ebel and Stewart, 2018; McCoy and Nittler, 2014). Both of these formation models have highly contrasting implications for the thermochemical evolution of Mercury and its bulk composition. In the next sections, we will explore several models of the bulk composition of Mercury considering the observational constraints on hermean geochemistry. Mercury is different enough from the other terrestrial planets that elemental behavior under Mercury conditions must first be reappraised before such models can be developed and/or evaluated.

Elemental Behavior Under Highly Reducing Conditions

Mercury formed under at least 2–3 orders of magnitude lower oxygen fugacity (fO_2) compared to the Earth, Moon, and Mars, thus affecting the valence state and bonding behavior of many elements. This significant difference has a fundamental effect on almost all aspects of the physicochemical properties of minerals and melts because O^{2-} is the dominant rock-forming anion and is a defining characteristic of lithophile behavior. Volatility and geochemical compatibility are also affected by oxygen fugacity. Differences in fO_2 are important because they exert a first order effect on the petrogenetic evolution of planetary bodies, including the initial distribution of elements in the interior, crystallization paths of magmas, stability of phases, and mineral chemistry. Here, we explore what is known from experimental data and natural observations of highly reduced meteorites to build a geochemical framework for element behavior under highly reducing conditions relevant to Mercury.

Geochemical affinity from reduced meteorite mineralogy

Although we have not yet identified any samples of Mercury amongst the world's meteorite collections, the aubrites and enstatite chondrites have been suggested as possible geochemical analogs of Mercury based on similarities in spectral properties, as well as their low intrinsic fO_2 that overlaps with estimates of Mercury fO_2 (Burbine et al., 2002; Fogel et al., 1989; Keil, 2010;

Udry et al., 2019; Weisberg and Kimura, 2012; Wilbur et al., 2022). Enstatite chondrites and aubrites are primarily composed of major orthopyroxene (Mg-endmember enstatite rather than ferrosilite) and minor olivine (Mg-endmember forsterite rather than fayalite) as well as minor Na-rich plagioclase (albite as opposed to Ca-endmember anorthite). Aubrites also contain rare diopside (rather than hedenbergite), which is uncommon in thermally metamorphosed enstatite chondrites (Fogel, 1997). Aubrites and enstatite chondrites also contain numerous metallic and sulfide phases that make up trace to major components of the modal mineralogy of these samples. In particular, they have Si-bearing Fe-rich metal (kamacite), Fe_3P (schreibersite), TiN (osbornite), and $(Ni,Fe)_5(Si,P)_2$ (perryite), indicating that Si, P, and N may exhibit siderophile behavior in highly reduced systems as they are hosted in silicide, phosphide, and nitride metallic phases, respectively (Keil, 2010; Mittlefehldt et al., 1998; Weisberg and Kimura, 2012). In contrast, P is hosted primarily by phosphate phases like apatite and merrillite in terrestrial, martian, and lunar systems (McCubbin and Jones, 2015), and N is typically an atmophile in these same systems (Füri and Marty, 2015; Mikhail and Sverjensky, 2014).

Sulfides in aubrites and enstatite chondrites include titanium-bearing FeS (troilite), CaS (oldhamite), (Fe,Mg)S (keilite), (Mg,Fe)S (niningerite), (Mn,Fe)S (alabandite), $FeCr_2S_4$ (daubréelite), and rarely TiS (wassonite), $NaCrS_2$ (caswellsilverite), $K_6Na(Fe^{2+},Cu,Ni)_{25}S_{26}Cl$ (djerfisherite), and $(Fe,Cr)(Ti,Fe)_2S_4$ (heideite) (Casanova et al., 1993; Fuchs, 1966; Keil, 2010; Keil and Brett, 1974; Keil et al., 2011; McCoy, 1998; Mittlefehldt et al., 1998; Nakamura-Messenger et al., 2012; Okada and Keil, 1982; Shimizu et al., 2002; Udry et al., 2019; Weisberg and Kimura, 2012; Wheelock et al., 1994; Wilbur et al., 2022). These sulfide phases are stable at fO_2 below IW–3, but they rapidly oxidize to sulfate and/or produce sulfurous gases under oxidizing terrestrial conditions (Keil, 2010; Vander Kaaden et al., 2019; Weisberg and Kimura, 2012). The sulfide mineralogy of reduced meteorites indicate that Mn, Ti, Ca, Mg, Na, Cr, K, and Cl have the potential to exhibit chalcophile behavior in highly reduced systems. Moreover, oldhamite is the primary host of rare earth elements (REE) in some aubrites (Dickinson and McCoy, 1997; Floss and Crozaz, 1993; Floss et al., 1990), indicating that REE may also exhibit chalcophile behavior under highly reducing conditions. A more complete listing of minerals in reduced meteorites can be found in review papers on enstatite chondrites (Weisberg and Kimura, 2012) and aubrites (Keil, 2010), but the mineralogy of these highly reduced meteorites indicates that the affinity of elements on Mercury may differ from those of terrestrial, lunar, and martian systems.

Geochemical affinity from experimental studies and bulk distribution coefficients

Numerous experimental studies have evaluated the geochemical affinities of elements under highly reducing conditions, and many of these studies were motivated, at least in part, by the discovery of highly reducing conditions on Mercury (e.g., Anzures et al., 2020; Boujibar et al., 2019; Chabot et al., 2014b; Dasgupta et al., 2022; Iacovino et al., 2023; Malavergne et al., 2014; Malavergne et al., 2010; Mouser et al., 2021; Namur et al., 2016a; Namur et al., 2016b; Pirotte et al., 2023; Pommier et al., 2023; Renggli et al., 2022; Steenstra et al., 2020a; Steenstra et al., 2020b; Steenstra and van Westrenen, 2020; Vander Kaaden and McCubbin, 2016; Vander Kaaden et al., 2020; Wohlers and Wood, 2017). However, a limited number of experimental studies under highly reduced conditions were conducted prior to, or not otherwise motivated by, discoveries about Mercury to better understand aubrites and enstatite chondrites (e.g., Dickinson and McCoy, 1997; Fogel, 2005; McCoy et al., 1999) or core formation on Earth and other terrestrial planets (e.g., Berthet et al., 2009; Bouhifd et al., 2007; Boujibar et al., 2014; Gessmann et al., 2001; Malavergne et al., 2007b; Righter et al., 2019; Rose-Weston et al., 2009; Wade and Wood, 2005; Wade et al., 2012; Wood et al., 2006). Quantitatively, lithophile – chalcophile – siderophile element behavior in highly reduced systems can be explored through an assessment of sulfide-silicate and metal-silicate partition coefficients. Element behavior can be visualized by plotting $D^{\text{sulfide-silicate}}$ vs. $D^{\text{metal-silicate}}$ (Figure 5), where elemental affinities are depicted by the region in which the data plot: siderophile > lithophile > chalcophile ($D^{\text{metal-silicate}}$ >1 and a $D^{\text{sulfide-silicate}}$ <1), chalcophile > lithophile > siderophile ($D^{\text{metal-silicate}}$ <1 and a $D^{\text{sulfide-silicate}}$ >1), as well as lithophile ($D^{\text{metal-silicate}}$ and $D^{\text{sulfide-silicate}}$ <1) and not lithophile ($D^{\text{metal-silicate}}$ and $D^{\text{sulfide-silicate}}$ >1) where siderophile > chalcophile and chalcophile > siderophile behavior are above and below the 1:1 line of $D^{\text{sulfide-silicate}}$ vs. $D^{\text{metal-silicate}}$, respectively (Vander Kaaden & McCubbin, 2016). The geochemical behavior of elements can be gleaned from highly reduced experiments containing sulfide, silicate, and metallic phases (e.g., Boujibar et al., 2019; Pirotte et al., 2023; Steenstra et al., 2022; Steenstra et al., 2020a,b,c; Vander Kaaden and McCubbin, 2016) or using the modal mineralogy and phase compositions of highly reduced meteorites (e.g., Wilbur et al., 2022).

On the basis of experimental and empirical data, most nominally lithophile elements (Mg, Ca, K, Na, Sr, Sc, Zr, Cl, Br, I, Mn, Y, Zr, Zn, Hf, Th, U, and REEs) become more chalcophile than siderophile at reducing conditions (Boujibar et al., 2019; Crozaz and Lundberg 1995; Floss

and Crozaz, 1993; McCubbin et al., 2012; Pirotte et al., 2023; Steenstra et al., 2020b,c; Vander Kaaden and McCubbin, 2016; Wilbur et al., 2022; Wohlers and Wood, 2017). However, a subset of nominally lithophile elements develop dual chalcophile and siderophile affinities at low fO_2, including Ti, V, Cr, Nb, Ta, and P (Pirotte et al., 2023; Steenstra et al., 2020a,b; Vander Kaaden and McCubbin, 2016; Wilbur et al., 2022). One complication to assigning a geochemical affinity at reducing conditions, however, is multiple sulfides are stable in the same equilibrium assemblage, and the partitioning behavior of elements varies as a function of sulfide composition (Pirotte et al., 2023). For example, Mg, Ca, Sr, Sc, Y, Zr, Hf, and REE preferentially partition into Mg- and/or Ca-dominant sulfides over Fe-dominant sulfides (Pirotte et al., 2023; Crozaz and Lundberg 1995; Floss and Crozaz, 1993; Wilbur et al., 2022; Figures 5–6), and Na, K, and Cl exhibit chalcophile behavior when hosted by the sulfide mineral djerfisherite (Ebel and Sack, 2013; Wilbur et al., 2022). In fact, some reduced meteorite assemblages include Ti-bearing troilite, oldhamite (CaS with minor Mg and Mn), djerfisherite, and either a Mg-rich niningerite (Mg,Fe,Ca)S or Mn-rich alabandite (Mn,Fe,Ca)S, respectively (Skinner and Luce, 1971; Wilbur et al., 2022). Furthermore, oldhamite concentrates REEs, with REEs naturally following Ca where CaS is the most REE-rich phase in enstatite chondrites and aubrites (Crozaz and Lundberg, 1995; Dickinson and McCoy, 1997; Floss and Crozaz, 1993; Floss et al., 1990; Gannoun et al., 2011; Hammouda et al., 2022). Although REE exhibit strong chalcophile behavior in Ca-rich sulfides at low fO_2, experimental data on sulfide-silicate systems indicate partitioning of REE's into FeS also increases at reducing conditions (Pirotte et al., 2023; Wohlers and Wood, 2017; Wood and Kiseeva, 2015).

The dominantly lithophile elements Si, P, Ti and Cr all become more siderophile under highly reducing conditions (McCubbin et al., 2017; Pasek, 2019; Steenstra et al., 2020b; Vander Kaaden and McCubbin, 2016; Wilbur et al., 2022). In addition, P, Ti, V, Cr, Fe, Ni, Ga, Ge, Nb, Ta, and Co lose their lithophile affinity altogether under highly reducing conditions (McCubbin et al., 2017; Pasek, 2019; Pirotte et al., 2023; Steenstra et al., 2020b; Vander Kaaden and McCubbin, 2016; Wilbur et al., 2022). Some elements that exhibit some degree of chalcophile affinity based on the Goldschmidt classification (Goldschmidt, 1937; Lee, 2018; Figure 6) also become more siderophile under highly reducing conditions, including Ge, Mo, Ag, Re, Ir, Bi, Sn, Sb, and In (Steenstra et al., 2022; Steenstra et al., 2020b; Figure 6). In contrast, the nominally siderophile elements Au, W, Ni, Co, and Pd demonstrate an increase in chalcophile behavior under highly

reducing conditions compared to typical fO_2 exhibited by Earth, Moon, and Mars (Steenstra et al., 2022; Steenstra et al., 2020b; Figure 6). Experimental studies at highly reducing conditions and bulk distribution coefficients from highly reduced meteorites demonstrate that the geochemical affinities of elements on Mercury deviate from those in terrestrial, lunar, and martian systems (Figure 5), consistent with the observations from the mineralogy of reduced aubrite and enstatite chondrite meteorites.

Goldschmidt's affinity classification for highly reduced systems

The Goldschmidt classification of element affinity is a powerful tool that groups elements within the Earth according to their preferred host phases (e.g., lithophile, chalcophile, siderophile, and atmophile ; Goldschmidt, 1937). This Goldschmidt classification shown in periodic table form in Figure 6 is useful to determine the initial distribution of elements into the mantle (lithophile), core (siderophile), and atmosphere (atmophile) of a planetary body, as well as glean how elements may partition during crystallization, decompression, oxidation, and other magmatic processes. However, at reducing conditions, nominally lithophile elements become more chalcophile and/or siderophile as summarized in the previous section. We have developed a modified Goldschmidt classification that is applicable to highly reducing systems and was established on the basis of both experimental and empirical observations of element distribution amongst silicate/oxide, metallic, and sulfide phases (Figure 6). This Mercury-relevant depiction of geochemical affinity, along with information about geochemical compatibility and volatility in the subsequent two sections, allows one to use the observations of Mercury surface compositions to make inferences about the bulk composition of the mantle and core, as well as infer the mineralogy of Mercury.

Valence of ions in geochemical systems and geochemical compatibility

The valence state of an element affects its geochemical compatibility because its ionic radius changes as it goes from a ground state to a +1, +2, +3, etc, cation (or conversely, negatively charged anion) state (Shannon, 1976). Its compatibility in various mineral and melt phases, therefore, are affected by the fO_2 of the system. Elements that change their valence state in geochemical systems as a function of oxygen fugacity are considered to be multivalent elements. At typical terrestrial, martian, and lunar fO_2, these multivalent elements include S, Fe, Cr, V, and Eu. At terrestrial and martian conditions near FMQ, S is present as 6+ and 2–, Fe exists as 3+ and

2+, V exists as 4+ and 3+, Eu as 3+ and 2+, while at lunar conditions near IW–1, Fe exists at 2+ and 0, Cr as 3+ and 2+, and V as 3+ and 2+ (Brounce et al., 2022; Cottrell et al., 2009; Hanson and Jones, 1998; Herd et al., 2002; Karner et al., 2007; Karner et al., 2010; Kelley and Cottrell, 2009; Kress and Carmichael, 1991; Papike et al., 2004; Papike et al., 2016; Wadhwa, 2001, 2008; Wallace and Carmichael, 1992). If we consider the reduced fO_2 in hermean systems, an even larger array of elements are considered to be multivalent, including H, Ti, Mn, P, and Si. Under the hermean fO_2 conditions discussed above (≤IW–3), S is 2–, Fe is 0 (except for 2+ in sulfides), Cr is 2+ or 0, P is either 5+ or 0, V is 2+, Eu is 2+, Si exists as both 4+ and 0, Mn as 2+ and 0, H is primarily 0 instead of 1+, and Ti exists as both 4+ and 3+ (McCubbin and Barnes, 2019; McCubbin et al., 2017; Papike et al., 2016; Pasek, 2015, 2019). For those elements that exhibit different valence states under hermean conditions than they do under terrestrial, martian, and lunar conditions, it is reasonable to hypothesize that these elements may also have differing geochemical compatibilities under these low fO_2 conditions. This potentially different geochemical behavior is particularly important for computing a planet's bulk silicate composition or core composition on the basis of elemental abundances at the surface because mantle-crust compatibility is the primary basis for inferring mantle geochemistry from crustal geochemistry (Hofmann, 1988).

Element volatility under highly reducing conditions

The oxidation state and geochemical affinity of an element has important implications for the volatility of that element because the physical properties vary across many substances with similar composition. For example, sodium oxide (Na_2O), which has $2Na^+$ bonded to O^{2-}, has a melting point of 1132 °C and a boiling point of 1950 °C (Chase, 1998). In contrast, sodium metal (Na^0) has a melting point of 98 °C and a boiling point of 898 °C (Chase, 1998). This example shows an extreme, but relevant, case in which the volatility of an element can be affected greatly by its oxidation state. Specific to Mercury, Na, K, and P are likely to be more volatile under hermean fO_2 compared to terrestrial, lunar, or martian conditions (McCubbin et al., 2017; Pasek, 2015). However, not all elements become more volatile as a function of decreasing fO_2. The sulfide phases oldhamite and niningerite are both stable under highly reducing conditions, but their melting temperatures are much higher than Fe, Ni, or Mn-sulfide phases (Lodders, 1996; Skinner and Luce, 1971), making S refractory when hosted by oldhamite and niningerite. In addition, N in terrestrial, lunar, and martian systems is considered a volatile and resides primarily in the

atmosphere, within volatile organic compounds, as ammonium in minerals, and/or as salts like nitrates (Marty, 2012; Mathew and Marti, 2001a, b, 2002; McCubbin et al., 2015; Mikhail and Sverjensky, 2014; Mortimer et al., 2016; Mysen, 2019). At hermean fO_2, nitrogen can be hosted in nitride minerals, many of which have very high melting points (Ettmayer et al., 1974), making nitrogen stored as nitrides a refractory form of N on Mercury and in aubrite and enstatite chondrite meteorites (Mittlefehldt et al., 1998). In addition, N solubility in silicate melts increases under highly reducing conditions (Dasgupta et al., 2022; Libourel et al., 2003), which will impact its overall compatibility. Carbon is hosted by graphite and carbides on Mercury and in reduced meteorites (Keil, 2010; Klima et al., 2018; McCubbin et al., 2017; Murchie et al., 2015; Vander Kaaden and McCubbin, 2015; Weisberg and Kimura, 2012), which are far more refractory than carbonates, organics, and fluid/gas phases that represent the primary hosts for C in terrestrial and martian systems (Ehlmann et al., 2008; Kelemen and Manning, 2015; Marty, 2012; Scheller et al., 2022; Steele et al., 2022; Steele et al., 2016; Taylor and McLennan, 1985). For every element that has a change in its oxidation state or geochemical affinity under highly reducing conditions, its volatility must be reassessed on the basis of those changes. Importantly, the presence of a refractory host for a nominally volatile element on Mercury does not imply the element cannot be volatile on Mercury. An example of this point is the graphite-melt smelting process discussed above that has been proposed as a mechanism to explain the low O/Si ratio on the surface of Mercury. In that process, refractory graphite reacts with components in its host silicate melt to produce volatile CO-gas species, which could account for over 75% of pyroclastic deposits on Mercury (Iacovino et al., 2023).

Mercury Bulk Composition

Several models of Mercury's bulk composition have been developed using telescopic and orbital observations of Mercury. These models include estimates for the bulk composition of the core as well as the composition of the bulk silicate portion of Mercury (i.e., primitive mantle). In this section, we synthesize the compositions reported in previous studies as well as develop our own models on the basis of hermean geochemical observations and the insights gained from our reappraisal of the geochemical behavior of the elements under highly reducing conditions.

Crust composition

The bulk silicate portion of every terrestrial planet is comprised of a mantle and a crust. The mantle makes up a much larger fraction of the bulk silicate, but the crust is exposed at the surface, making it the most accessible portion for direct measurement of its chemical composition (Taylor and McLennan, 2008). Much like the Moon, Mercury is reported to have a primary crust and a secondary crust. The global distribution of an opaque phase on Mercury (Murchie et al., 2015), the enrichment of that opaque phase in the LRM sourced from depth (Klima et al., 2018), the neutron absorption properties associated with the LRM (Peplowski et al., 2016), and the detection of carbon across the hermean surface by GRS (Peplowski et al., 2015a) all support the hypothesis that Mercury had a graphitic primary crust (Vander Kaaden and McCubbin, 2015). The thickness of the primary crust is unknown, but if the average C abundance of 1.4 wt% for the average surface composition is considered to be representative of the bulk crust, it would correspond to a thickness of approximately 1 km at the base of the 35–53 km crust (Margot et al., 2019; Vander Kaaden and McCubbin, 2015). This primary crust thickness estimate is likely to represent a lower bound because the LRM sourced from depth shows even larger enrichments in C compared to the bulk crust (Klima et al., 2018), indicating that the primary and secondary crusts are poorly mixed and that the primary crust is likely underrepresented in the bulk crust composition reported here (Table 1). The remainder of the crust is comprised of secondary crust produced through volcanism on Mercury (Byrne et al., 2016; Byrne et al., 2018; Denevi et al., 2013; Denevi et al., 2009; Head et al., 2011; Head et al., 2008; Head et al., 2009; Marchi et al., 2013; Robinson and Lucey, 1997; Thomas et al., 2014b; Thomas et al., 2014c). In fact, Mercury has been completely resurfaced by volcanic activity, with a surface age that spans 4.1 to 3.5 Ga (Byrne et al., 2016; Marchi et al., 2013). In addition to volcanism, the surface of Mercury has been reworked by impact processes (Blewett et al., 2016; Cintala, 1992; Domingue et al., 2014; Frank et al., 2017; Marchi et al., 2013; Mojzsis et al., 2018). Although the surface exhibits lateral heterogeneities (Denevi et al., 2009; Lawrence et al., 2017; Peplowski et al., 2015b; Peplowski and Stockstill-Cahill, 2019; Vander Kaaden et al., 2017; Weider et al., 2015), the average surface composition of Mercury represents our best estimate, at this time, of the bulk composition of Mercury's crust (Table 1).

Core composition

Mercury's high density and weak magnetic field indicates the presence of a large solid inner and liquid metallic outer core that makes up a majority of the planet. Mercury's core makes up a larger fraction of its mass, at ~71–78% (Hauck II et al., 2013; Margot et al., 2019), than any of the other terrestrial planets at 30-40% mass fraction (Anderson et al., 1987). Planetary cores are composed mostly of Fe (the most abundant heavy element in the Solar System), Ni as a minor element (nickel present in iron meteorites as likely samples of differentiated meteorite cores), and a combination of light elements like H, C, O, Si, and S (Nittler et al., 2018). The highly reducing conditions on Mercury indicate that Ti, Cr, Mn, and P may also reside in the core (Figure 6). Mercury exhibits evidence of a molten outer core (Margot et al., 2007), which implies that Mercury's core is not pure Fe-Ni, otherwise it would have fully solidified by present time (Schubert et al., 1988). The specific identity and combination of light elements in Mercury's core has proven difficult to constrain from bulk geophysical parameters such as radius, bulk density, and moment of inertia (Hauck II et al., 2013; Margot et al., 2019). Prior to MESSENGER, S was proposed as the main light element (Chabot et al., 2014b; Chen et al., 2008; Malavergne et al., 2010; Riner et al., 2008), however the highly reduced nature of Mercury, as exposed by MESSENGER results, prompted renewed questions about the contributions from other light elements, like Si, O, H, and C, to Mercury's highly reduced core (Berrada et al., 2022; Chabot et al., 2014b; Deng et al., 2013; Edmund et al., 2022; Knibbe et al., 2021; Knibbe and van Westrenen, 2018; Malavergne et al., 2014; Margot et al., 2019; Nittler et al., 2018; Steenstra et al., 2020b; Steenstra and van Westrenen, 2020; Vander Kaaden et al., 2020).

Mercury's core composition likely lies between an Fe-Ni-Si endmember and a mixture of Fe, Ni, Si, C, and S (Chabot et al., 2014b; Knibbe et al., 2021; Margot et al., 2019; Nittler et al., 2018; Vander Kaaden et al., 2020), with minor and trace contributions from many other elements. Chabot et al. (2014b) showed that a core with up to 5 wt.% S and 8 wt.% Si may be in equilibrium with an S-rich hermean silicate mantle. Vander Kaaden et al. (2020) focused on Si and C at the reduced conditions relevant to Mercury and found an anti-correlation between Si and C solubility in Fe-rich metal. They reported that an Fe-rich hermean core at carbon-saturation has 0.5–6.4 wt.% C, where 0.5 wt.% C corresponds to 25 wt.% Si and 6.4 wt.% C corresponds to an Si-free core. Experiments in Fe-Ni systems have demonstrated, however, that Ni can also affect C, S, O, and Si solubility in Fe-rich metallic melts (Chabot et al., 2015; Dasgupta et al., 2013; Kim et al., 2014; Malavergne et al., 2014; Zhang and Fei, 2008; Zhang et al., 2018). Vander Kaaden et al. (2020)

used their results and those from previous studies to estimate that Mercury has an Fe-rich core with a chondritic Fe/Ni ratio, up to 5% each of C and S, and 0.3–25 wt% Si (Table 3). Models of Mercury's interior structure that are consistent with core dynamo simulations (i.e., with an inner core radius below 1200 km; Christensen and Wicht, 2008; Takahashi et al., 2019)indicate <7.5 wt.% Si in the core (Knibbe et al., 2021). A compilation of proposed Mercury core compositions (major and minor elements only) is provided in Table 3. On the basis of mantle fO_2, elemental behavior under hermean conditions, and experimental studies of core formation on Mercury, our preferred model for the composition of the hermean core is composed of Fe and Ni in chondritic proportions with some combination of Si, S, C, Cr, P, Ti, and Mn in lower abundances (≤5 wt.% S and C, up to 7 wt.% Si, and ≤1% each of P, Ti, Cr, and Mn; Table 3). Additional experimental studies are needed to assess the potential contributions of H and O to the light-element-component of Mercury's core.

All of the core compositions in Table 3, with relatively low Si, imply that bulk Mercury has a superchondritic Fe/Si ratio regardless of its bulk silicate composition, unless bulk Mercury has a composition similar to the most metal-rich CB meteorites (Brown and Elkins-Tanton, 2009; Cartier and Wood, 2019; Vander Kaaden et al., 2020). Mercury's core would need ≥27 wt% Si to have a bulk Fe/Si ratio that matches enstatite chondrites (Vander Kaaden et al., 2020). A process that enriches Fe-rich metal relative to silicate is likely required to explain the Fe/Si ratio of bulk Mercury, and this observation is a key factor in unraveling the origin of Mercury. Although the impact origin models are designed to explain the anomalous metal:silicate ratio of Mercury (Asphaug and Reufer, 2014; Benz et al., 2007; Benz et al., 1988; Cameron et al., 1988; Ebel and Stewart, 2018; Helffrich et al., 2019; Smith, 1979; Wetherill, 1988), formation from highly reduced precursor materials that are not well represented in chondrite meteorites remains a plausible explanation (Cartier and Wood, 2019; Ebel and Stewart, 2018; McCoy and Nittler, 2014), particularly given the highly reduced nature of Mercury (Malavergne et al., 2010; McCubbin et al., 2012; McCubbin et al., 2017; Namur et al., 2016a; Zolotov et al., 2013).

Bulk silicate composition

The bulk silicate composition of a terrestrial planet is inescapably linked to its origin and subsequent thermochemical evolution. Much of the bulk silicate portion of a planet is comprised

of its mantle, which is typically concealed by its crust. Although direct measurement of the entire mantle is not possible, constraints can be placed on mantle composition using the composition of the crust (i.e., surface lavas), upper mantle (e.g., mantle xenoliths), the core (when possible), meteorites thought to represent the building blocks of planets, and/or mass balance constraints derived from geophysical data (Dreibus et al., 1977; Dreibus and Wänke, 1985; Hofmann, 1988; McDonough and Sun, 1995; Morgan and Anders, 1980; Righter et al., 2006; Taylor, 2013; Taylor and Wieczorek, 2014). Compositional and geophysical data obtained from MESSENGER have been used in combination with chondrite meteorite compositions and/or phase equilibrium studies to develop compositional models for the bulk silicate portion of Mercury. It is important to note, however, that there is a dearth of geochemical data for Mercury relative to Earth, Moon, and Mars because we have no samples of Mercury, and all data are from orbital and ground-based remote sensing instruments. Consequently, the compositional models of bulk silicate Mercury are poorly constrained.

A central tenet to models of the bulk silicate portions of planets is that their bulk silicate compositions exhibit chondritic abundance ratios for refractory lithophile elements. Furthermore, for refractory elements that exhibit both lithophile and siderophile tendencies, their bulk planet ratios (core + bulk silicate) are presumed to be chondritic. In contrast, models assuming initially chondritic refractory ratios for the bulk silicate compositions of planets has been challenged on the basis of ε^{142}Nd measurements that imply superchondritic Sm/Nd ratios (e.g., Boyet and Carlson, 2006; Caro et al., 2008), so Mercury may also exhibit non-chondritic ratios for some refractory elements. In fact, the presumption of chondritic abundance ratios for refractory lithophile elements is already problematic for Mercury because its large core that is mostly Fe with some Si necessitates either a superchondritic Fe/Si ratio for bulk Mercury or chondritic Fe/Si and superchondritic abundances of Si in bulk Mercury (Righter et al., 2006; Vander Kaaden et al., 2020). A superchondritic Fe/Si for bulk Mercury can be explained through either giant impact models (Benz et al., 2007) or metal-enrichment models (Cartier and Wood, 2019; Ebel and Stewart, 2018; McCoy and Nittler, 2014), but plausible models for Si-enrichment in bulk Mercury have not been put forward. There is evidence from metal-rich primitive meteorites that metal-enrichment processes operated early in Solar System history (Weisberg et al., 1988), although the metal is typically Si-poor and many of the metal-enrichment processes likely involved impacts (Lauretta et al., 2009; Weisberg et al., 2001). Nonetheless, it is presumed in models of Mercury's

bulk composition that it hosts chondritic abundance ratios of refractory major and minor elements, exclusive of Fe/Si and X/Si where X is represented by other dominantly siderophile elements.

The abundances of refractory major elements determined by MESSENGER include Si, Mg, Al, and Ca. All four of these elements are dominantly lithophile (Figure 5-6), but Si exhibits slight siderophile behavior and Mg and Ca exhibit slight chalcophile behavior in highly reduced systems. Given that Si, Mg, Al, and Ca remain largely lithophile under hermean fO_2, the bulk silicate portion of Mercury can be estimated by examining key compositional relationships between terrestrial planets and meteorites for major refractory lithophile elements, including Mg/Si, Al/Si, and Ca/Si ratios (Righter et al., 2006). In particular, a plot of Mg/Si vs. Al/Si can be used to interrogate magmatic fractionation processes where the partial melting of major mantle minerals (e.g. olivine, orthopyroxene, clinopyroxene, and garnet) result in lower Mg/Si and higher Al/Si in a partial melt relative to its source. On the other hand, chondritic meteorites display a linear trend of increasing Mg/Si with increasing Al/Si referred to as the "cosmochemical fractionation" line (Jagoutz et al., 1979). The intersection of the "cosmochemical fractionation" line with a magmatic fractionation line derived from primitive ultramafic lava compositions can thus be used as an estimate of the bulk silicate Mg/Si and Al/Si of a planet as shown in Figure 7. In particular, this diagram can help distinguish a pyroxene-dominated from an olivine-dominated mantle source for these lavas. The broad range of surface compositions exhibited by Mercury could be consistent with either model (i.e., pyroxene- or olivine-dominant); however, given the large mass fraction of Mercury's core and the possibility that Si may be a minor or major light element in the core, the abundance of SiO_2 in the bulk silicate portion of Mercury (i.e., pyroxene dominant vs olivine dominant) will be highly influenced by the core Si abundance.

Numerous primitive mantle compositions of Mercury (i.e., prior to any melting and representative of bulk silicate portion of Mercury) have been estimated, including several that were developed prior to MESSENGER arriving at Mercury (Lodders and Fegley, 1998 and references therein). The first of the MESSENGER-era estimates were based on phase equilibrium experiments on two endmember surface lavas (northern smooth plains and IcP-HCT) coupled with a batch adiabatic decompression melting model (Namur et al., 2016b; Nittler et al., 2018). These results were combined with mass balance calculations to estimate two model compositions for Mercury's primitive mantle. Both compositions yielded similar mantle compositions, with small

differences in CaO and Na_2O (Nittler et al., 2018). The average of the two mantle compositions is listed in Table 4 as PMM-MB. The PMM-MB model is a pyroxene-dominant model (Figure 7) and implies a core with about 1.5–3.5 wt% Si on the basis of bulk Mercury having a chondritic Mg/Si ratio. The lower bound of core Si abundances corresponds to Mercury's large core (mass fraction of 0.74) being a primordial feature of Mercury, and the higher bound presumes that proto-Mercury had a core mass fraction of 0.4, closer to other terrestrial planets in our solar system (Anderson et al., 1987). All other ranges in core Si abundance discussed below represent the same two upper and lower boundary conditions.

Numerous researchers have drawn comparisons between Mercury and some metal-rich and/or highly reduced meteorites, including enstatite chondrites, bencubbinites, CH chondrites, and aubrites (Anzures et al., 2020; Brown and Elkins-Tanton, 2009; Cartier and Wood, 2019; Malavergne et al., 2010; McCoy et al., 1999; Nittler et al., 2018; Taylor and Scott, 2003; Udry et al., 2019; Wasson, 1988; Wilbur et al., 2022). In fact, several MESSENGER-era estimates of Mercury's bulk silicate composition are derived from chondrite compositions. Nittler et al. (2018) demonstrated that EH, EL, and CB chondrite compositions with 20% of their SiO_2 reduced and sequestered into the core would yield bulk silicate compositions that are very similar to the PMM-MB composition in Table 4. The model bulk silicate composition of Mercury based on average enstatite chondrite with 20% of the total SiO_2 removed is reported in Table 4 as EC-Si80%. Similar to the PMM-MB composition, the EC-Si80% composition results in a pyroxene-dominant mantle (Figure 7). Furthermore, the reduction of 20% of the total SiO_2 from an EC into the core results in about 1.5–3.5 wt% Si in the core given the large core mass fraction of Mercury (Table 4).

In addition to E chondrite-based models, the bulk silicate composition of Mercury has also been estimated from the CH chondrite ALH 85085 (Anzures et al., 2020). ALH 85085 has Al/Si and Mg/Si ratios similar to those of other models of bulk silicate Mercury, but it also has one of the highest chondrite metal abundances at 40 wt.% Si-bearing Fe-rich metal (with an average Si content in metal of 0.38% with analyses ranging from below detection to 7.5 wt% Si; Weisberg et al., 1988). This higher metal content is consistent with Mercury's internal structure with a large core, and is much closer to expected Fe/Si and Ni/Si ratios of Mercury compared to other chondrite-based compositional models; however, the CH composition is still Fe-depleted compared to bulk Mercury. Unlike other metal-rich chondrites, which tend to be more oxidized

than Mercury (i.e., CB chondrites), ALH85085 formed under highly reducing conditions within the range of fO_2 estimates of Mercury (fO_2 at IW–5 from Petaev et al., 2003). The model bulk silicate composition of Mercury based on CH chondrite ALH 85085 is reported in Table 4 as CH. The CH composition has a pyroxene:olivine ratio near unity (Figure 7), but the estimated Si content of the core is <1 wt% (Table 4).

Most of the model bulk compositions yield pyroxene-rich mantles with low Si abundances in the core. To explore whether any olivine-dominant models could be plausible for the bulk silicate composition of Mercury, we estimate a model bulk silicate Mercury assuming that the core has 5 wt% Si (Table 3). The bulk silicate portion is computed based on geophysical data that suggests the crust makes up about 8% (mass) of the bulk silicate portion of Mercury and the mantle is ~92% (mass) (computed from Margot et al., 2019). Furthermore, our mantle model considers the hypothesis that the HMR terrane is representative of a high-degree partial melt of Mercury's mantle that was induced by a large impact (as suggested by Weider et al., 2015). Consequently, we start with an HMR composition and add forsteritic olivine, enstatitic pyroxene, and diopsidic pyroxene until we yield enstatite chondrite ratios for Mg/Si, Al/Si, and Ca/Si for bulk Mercury. With 5 wt% Si in the core, we reach enstatite chondrite ratios for Mg/Si, Al/Si, and Ca/Si for bulk Mercury with a mantle comprised of 30% HMR, 67.5% Fo_{99}, and 2.5% Di_{99}. The addition of any enstatitic pyroxene to HMR-based compositions could not yield chondritic Mg/Si, Al/Si, and Ca/Si ratios, simultaneously. In the simplest sense, this model implies that the HMR was derived by high degrees of partial melting such that only olivine was left in the source after melting, which has also been proposed as one possible interpretation of the phase diagram for the BP-HMg lavas (Vander Kaaden and McCubbin, 2016). In other words, the average depth of melting may not correspond to a multiple saturation point on an HMR phase diagram. The model bulk silicate composition of Mercury based on this approach is reported in Table 4 as HMR+Fo_{99}-MB, and the corresponding core composition has the same name and is reported in Table 3. Following the approach of Nittler et al., (2018), we computed an additional model bulk silicate composition of Mercury on the basis of enstatite chondrites by determining what percentage of SiO_2 would need to be sequestered in the core before the bulk composition would be similar to our HMR+Fo_{99}-MB model. We determined that reduction of 40% of the total SiO_2 in EC yields a bulk composition that is strikingly similar to the HMR+Fo_{99}-MB model (Figure 7; Table 4). Our EC model composition is reported in Table 4 as EC-Si60%. Similar to the HMR+Fo_{99}-MB model, the EC-

Si60% yields an olivine-dominant hermean mantle with a core Si abundance in the range of 2.8–6.6 wt%.

In summary, we have insufficient information at this time to determine whether Mercury has an olivine- or pyroxene-dominant mantle composition because both are consistent with the data. Although the compositions of several of the surface terranes lie along a fractionation line consistent with a pyroxene-dominated mantle (Figure 7), two of our best candidates for primitive melt compositions from Mercury (i.e., HMR and IT terranes) lie on a fractionation line that is consistent with an olivine-dominated mantle (Figure 7). Furthermore, these models highlight how small changes in core Si abundance from 1.5 to 5 wt% can shift Mercury from a pyroxene-rich to an olivine-rich mantle if bulk Mercury has chondritic Mg/Si, Al/Si, and Ca/Si ratios. In fact, the Si abundance of the core cannot exceed about 7 wt% Si for any chondritic model without the need for highly silica-undersaturated hermean mantle mineralogy (e.g., periclase, melilite, hibonite). Future exploration of Mercury, and analysis of samples from Mercury in particular, will provide invaluable constraints on the bulk composition of Mercury that are not possible with the data available at this time (Ernst et al., 2022; Rothery et al., 2020; Vander Kaaden et al., 2019). However, the compositional differences among these models offer important testable hypotheses that can be interrogated with new datasets.

Thermochemical Evolution From Geochemistry

MESSENGER revealed that Mercury's surface is compositionally heterogeneous, including multiple geochemical terranes distinguished by their chemical and morphological differences (Lawrence et al., 2017; Peplowski et al., 2015b; Peplowski and Stockstill-Cahill, 2019; Vander Kaaden et al., 2017; Weider et al., 2015; Figure 2). The largest volcanic units, Borealis Planitia (BP) and the Intercratered Plains and Heavily Cratered Terrain (IcP-HCT), have been dated to between 4.1 and 3.5 Ga (Byrne et al., 2016; Denevi et al., 2009; Head et al., 2011; Marchi et al., 2013), which are thought to form from harzburgitic and lherzolitic mantle sources, respectively (Charlier et al., 2013). Experiments have shown that these different surface volcanic units cannot be directly related by different degrees of fractional crystallization, implying multiple-stage differentiation or re-melting processes (Charlier et al., 2013; Namur et al., 2016b; Vander Kaaden and McCubbin, 2016). These distinct mantle sources hint at a heterogenous mantle

preserved through Mercury's early history, which can be a remnant of the initial layering and/or subsequent mixing of cumulates that crystallized from a hermean magma ocean (Brown and Elkins-Tanton, 2009; Mouser et al., 2021; Riner et al., 2009). This section walks through our current understanding of the thermochemical evolution of Mercury's interior in chronological order.

Magma ocean

It is generally assumed that at the end stages of planetary accretion, the terrestrial planets were partially or entirely molten, primarily due to the large amount of accretionary heat and heat released during core formation (e.g., Canup and Asphaug, 2001; Elkins-Tanton, 2012; Elkins-Tanton et al., 2003; Solomon and Longhi, 1977). For the Earth-Moon system and Mercury, magma oceans could have been produced by giant impacts as well (Lock et al., 2018; Tonks and Melosh, 1993; Wetherill, 1980). A magma ocean allows for efficient separation of metal and silicate melt given the large density differences between the two phases, where the metal accumulates at the center of mass of the body to form a metallic core. As core formation proceeds, bulk silicate Mercury crystallizes into a cumulate mantle and primary crust, the latter of which could be a flotation crust if any of the minerals that crystallize from the magma ocean are buoyant. Depending on the composition of the bulk silicate and style of crystallization (e.g., fractional vs equilibrium crystallization), the resulting mantle could exhibit lateral and spatial heterogeneities that could be further complicated by density-driven cumulate overturn (e.g., Charlier et al., 2018; Elardo et al., 2011; Elardo et al., 2015; Elkins-Tanton, 2012; Elkins-Tanton and Grove, 2011; Elkins-Tanton et al., 2005a; Elkins-Tanton et al., 2003; Elkins-Tanton et al., 2002; Elkins-Tanton et al., 2005b; Mandler and Elkins-Tanton, 2013; Righter and Drake, 1996, 1997; Snyder et al., 1992; Solomatov, 2000; Solomatov et al., 1993; Solomatov and Stevenson, 1993; Solomon and Longhi, 1977).

Mercury's low Fe, high C, and high S abundances at the surface implies a new endmember case for magma ocean evolution among terrestrial planets because mineral and melt density-driven segregation is largely due to the abundance and distribution of Fe. Specifically, the low FeO abundance of the bulk silicate portion of Mercury does not permit the formation of a lunar-like anorthositic primary flotation crust because late-stage magma ocean liquids would have been less dense than plagioclase (Mouser et al., 2021; Riner et al., 2009; Vander Kaaden and McCubbin,

2015). In fact, the only rock-forming minerals that are buoyant with respect to late-stage Mercury magma ocean melts include graphite, oldhamite, and niningerite (Boukaré et al., 2019; Lark et al., 2022; Vander Kaaden and McCubbin, 2015). Of these minerals, there is evidence that Mercury had a primary graphite flotation crust (Klima et al., 2018; McCubbin et al., 2017; Murchie et al., 2015; Peplowski et al., 2016; Peplowski et al., 2015a; Vander Kaaden and McCubbin, 2015), and the presence and role of sulfides in this primary flotation crust is an active area of investigation (e.g., Boukaré et al., 2019; Lark et al., 2022). Mercury's global surface is much darker than expected from its measured elemental composition, with the brightest parts of Mercury's volcanic surface still darker than the darkest volcanic parts of the Moon (Denevi and Robinson, 2008; Riner et al., 2009). In fact, Mercury's most common spectral unit, the intermediate plains, reflects ~27% less sunlight than the lunar highlands and ~14% less than the mare-basalt dominated lunar nearside, with lunar reflectance varying inversely with the abundance of opaque minerals such as ilmenite ($FeTiO_3$) and Fe-rich pyroxene (Denevi and Robinson, 2008; Peplowski et al., 2016). Mercury's fresh material also has half the reflectance of similar material on the Moon that has not experienced extensive space weathering (Denevi and Robinson, 2008). These two observations require a darkening agent across the surface of Mercury that is distinct from the Fe-Ti oxide darkening agents on the Moon (Lucey and Riner, 2011; Riner et al., 2009; Riner et al., 2010). The global distribution of an opaque phase on Mercury (Murchie et al., 2015); the enrichment of that opaque phase in the LRM sourced from depth (Klima et al., 2018), the neutron absorption properties associated with the LRM (Peplowski et al., 2016), and the detection of carbon across the hermean surface by GRS (Peplowski et al., 2015a) all support the identity of the opaque phase as being graphitic carbon. The global distribution of the graphite layer at depth supports the hypothesis that Mercury had a primary flotation crust made of graphite that formed very early, prior to major magma ocean crystallization (Mouser et al., 2021; Peplowski et al., 2016; Vander Kaaden and McCubbin, 2015). Furthermore, the thickness of that graphite crust, estimated in this study to be at least ~1 km in thickness, is sufficient to induce a highly stratified cumulate mantle during magma ocean crystallization (Mouser et al., 2021).

The initial crystallization of silicates from the hermean magma ocean began at the core-mantle boundary and proceeded toward the surface because the slope of the adiabat in the magma ocean is steeper than the solidus of the bulk magma ocean, causing the first intersection of the adiabat with the solidus to occur at depth (Brown and Elkins-Tanton, 2009). This bottom-up

crystallization sequence would result in a stratified cumulate mantle, but the degree to which it is stratified throughout depends on the viscosity and cooling rate of the magma ocean, which determines the efficiency of crystal fractionation (Dygert et al., 2017; Elkins-Tanton et al., 2011; Mouser et al., 2021; Solomatov, 2007). The sulfur rich nature of bulk silicate Mercury results in a reduction in melt viscosity compared to otherwise equivalent S-free melts (Mouser et al., 2021). The cooling rate of a magma ocean is affected by the surface area-to-volume ratio of the body as well as the presence or absence of a primary flotation crust, with cooling rates about 150 times slower on Mercury when a primary flotation crust is present (Mouser et al., 2021). Using the CH bulk silicate composition from Table 4, Mouser et al. (2021) demonstrated that a primary flotation crust results in a highly stratified hermean mantle consisting of (from the core-mantle boundary to the surface) olivine, olivine + orthopyroxene, orthopyroxene + clinopyroxene, clinopyroxene + plagioclase, and finally a primary flotation crust. In contrast, the absence of a primary flotation crust resulted in limited compositional stratification with (from the core-mantle boundary to the surface) olivine, olivine + orthopyroxene, and then a homogenous lherzolitic mantle (Mouser et al., 2021). Notably, a lherzolitic mantle source is needed to produce the IcP-HCT lavas (Charlier et al., 2013; Namur et al., 2016b), and a lherzolitic layer is not produced through magma ocean crystallization alone in the primary flotation crust scenario described in Mouser et al. (2021). However, magma ocean solidification typically happens in two stages, with the first stage being crystallization and the second stage representing density-driven cumulate mantle overturn (Brown and Elkins-Tanton, 2009). Given the low FeO abundance in the bulk silicate portion of Mercury, density contrasts between early magma ocean cumulates and late magma ocean cumulates may not have been sufficient to induce downwelling Rayleigh-Taylor instabilities needed to drive large-scale cumulate mantle overturn (Mouser et al., 2021; Vander Kaaden and McCubbin, 2015); however, the density differences between Mg-rich clinopyroxene and Mg-rich olivine may have been sufficient to drive localized cumulate mixing in Mercury, resulting in the formation of a lherzolitic source from an initially stratified hermean mantle (Mouser et al., 2021).

Only one model bulk silicate composition has been evaluated to understand hermean magma ocean crystallization (Mouser et al., 2021), although some work has been done prior to the arrival of MESSENGER at Mercury using earlier estimates of the bulk silicate composition of Mercury (Brown and Elkins-Tanton, 2009). Additional studies using a wider array of bulk silicate compositional models are needed to place better constraints on the initial distribution and internal

structure of Mercury's mantle. Furthermore, dedicated studies to understand the role of sulfur during magma ocean crystallization will also be key to understanding the role of S in Mercury's mantle. For example, Boukaré et al. (2019) modeled the effect of S saturation in silicate melt to assess the production of sulfide layering in Mercury's mantle, where heat-producing elements such as U could concentrate (Boujibar et al., 2019; Wohlers and Wood, 2017). They found that the depth and thickness at which sulfides precipitate in the magma ocean is dependent on oxygen fugacity and initial sulfur content. For a given initial S content, decreasing fO_2 moves sulfide precipitation toward the surface, while for a given fO_2, increasing initial S content moves sulfide precipitation toward the core-mantle boundary. Additional experimental and modeling work is needed to better constrain the interior structure and physicochemical evolution of Mercury's mantle.

Volcanic secondary crust production

Three of the geochemical terranes (BP-LMg, BP-HMg, and the Caloris Basin interior plains) formed around the same time from 3.55–3.8 Ga, inferred from the cratering record (Marchi et al., 2013), yet have substantial geochemical differences that may reflect different mantle sources (Charlier et al., 2013; Namur et al., 2016b; Vander Kaaden and McCubbin, 2016; Figure 7). Geochemical differences in Na, Al, Mg, and Ca abundances could result from different degrees of partial melting of a common mantle reservoir (Stockstill-Cahill et al., 2012; Weider et al., 2012), from fractional crystallization of a common parent magma (Charlier et al., 2013), or from melting of a vertically and/or laterally heterogenous mantle (Namur et al., 2016b; Vander Kaaden et al., 2017; Weider et al., 2015), with implications for the interior structure subsequent to magma ocean crystallization. In particular, Charlier et al. (2013) found that the presence or absence of clinopyroxene, requiring lherzolitic and harzburgitic mantle sources, respectively, led to contrasting differentiation paths to account for the variation in surface lava compositions across Mercury. Namur et al. (2016b) considered the effect of S, Na, and pressure on the phase equilibria of hermean lavas and found that the high-Mg portion of the IcP-HCT terrane requires a clinopyroxene-bearing lherzolitic source at greater depth (>1.5 Gpa) compared with the BP-LMg and CB terranes, both of which require a clinopyroxene-free harzburgitic source at shallow depth. However, Vander Kaaden and McCubbin (2016) noted that the BP-HMg composition could have been derived by large-degree partial melting of a shallow source with only olivine left in the source

after melting. Vander Kaaden and McCubbin (2016) did not implicate the multiple saturation point as the average depth of melting for the source of the BP-HMg lavas because it would have required substantial Na abundances within the deep hermean interior given the inferred high-degree of melting required to account for the large volume of lava emplaced within the northern smooth plains through flood volcanism (Head et al., 2011; Ostrach et al., 2015). The results of Mouser et al. (2021) offer a potential solution to the contrasting interpretations on the basis of cumulate mantle overturn that was driven by formation of downwelling Raleigh-Taylor instabilities, provided that cumulate overturn did not occur uniformly at a global scale. At the end of magma ocean crystallization, the configuration of cumulate layers would yield an inverted, gravitationally unstable density structure because in Fe-poor systems, pyroxene (especially high-Ca pyroxene) is denser than olivine (Mouser et al., 2021). This gravitational-driven mixing would produce an appropriate lherzolitic source at depth for the high-Mg IcP-HCT composition at the higher pressures inferred from Namur et al. (2016b), and a shallow olivine-dominated, plagioclase-bearing source, inferred from Vander Kaaden and McCubbin (2016) for the BP-HMg composition, would exist where the cumulate overturn was more limited or did not occur.

At this time, we only have detailed chemical information about terranes in the northern hemisphere (Solomon and Byrne, 2019; Solomon et al., 2001). BepiColombo will have a more circular orbit (Benkhoff et al., 2021) compared to MESSENGER and will provide our first detailed information about the composition and identity of geochemical terranes in Mercury's southern hemisphere (Rothery et al., 2020). This information will be invaluable for deciphering the thermochemical evolution of Mercury and for better contextualizing the wealth of geochemical data on the hermean surface that was collected by MESSENGER.

Geochemistry of the Surface and Exosphere

Mercury's endmember surface geochemistry also manifests itself in unique geologic landforms that link Mercury's interior with its exosphere, especially with regards to volatiles (e.g., Blewett et al., 2011; Blewett et al., 2016; Blewett et al., 2013; Chabot et al., 2014a; Chabot et al., 2018b; Helbert et al., 2013; Phillips et al., 2021; Vilas et al., 2016). Mercury's proximity to the Sun, 3:2 spin orbit resonance, lack of a dense atmosphere, and weak magnetic field allows its surface to experience dramatic temperature variations and be subjected to intense space weathering

that can release and redistribute volatiles (Cintala, 1992; Domingue et al., 2014). Mercury has abundant hollows, which are unique rimless, flat-bottomed pits largely associated with craters in the LRM that are thought to form from sublimation of a volatile-rich phase (Blewett et al., 2011; Blewett et al., 2016; Blewett et al., 2013; Thomas et al., 2016; Thomas et al., 2014a). Mercury also has abundant ice deposits in permanently shadowed regions despite its high daytime temperatures due to its proximity to the Sun, with more widespread evidence for water ice than the Moon (Chabot et al., 2014a; Chabot et al., 2018b; Delitsky et al., 2017; Lawrence et al., 2013; Neumann et al., 2013; Paige et al., 2013). The composition of Mercury's tenuous exosphere also reflects the volatiles originating from the surface, vaporized and ionized by Mercury's intense space weathering environment and bound by Mercury's magnetosphere (Slavin et al., 2014; Vervack et al., 2010; Zurbuchen et al., 2008). The origin and evolution of these hermean surface features have important implications for hermean surface geochemistry and the geochemistry of airless bodies broadly. Given that future exploration of Mercury, including future landers and/or sample return missions (Ernst et al., 2022; Vander Kaaden et al., 2019), would necessarily focus on the surface, it is important to understand the geochemical processes that operate in the hermean surface environment.

Space weathering

The surface composition, proximity to the Sun, high density, and weak magnetosphere provides an intense and unique space weathering environment to study volatile geochemistry on Mercury's surface. Mercury experiences a more intense space weathering environment compared with other airless rocky bodies (Cintala, 1992; Domingue et al., 2014; Marchi et al., 2009). For example, impacts on Mercury are predicted to produce 13.5 times the melt and 19.5 times the vapor per unit area compared with similar impacts on the Moon (Cintala, 1992). Mercury also has extreme temperature regimes with daytime temperatures up to 430 °C and nighttime temperatures as low as -180 °C. Mercury's 3:2 spin-orbit resonance also causes longitudes 0° and 180 °E to experience noon on successive perihelia producing "hot pole" longitudes that are subjected to greater levels of solar radiation and reach higher temperatures compared with longitudes of 90 ° and 270 °. Due to its spin-orbit resonance and heavily cratered surface, Mercury also has numerous permanently shadowed regions in craters where ice is continuously stable (e.g., Chabot et al., 2018b).

While space weathering of the Moon and near-Earth S-type asteroids is well understood, insights into other planetary bodies are limited. One key difference is Mercury's low surface Fe, where Fe plays a critical role in the development of space weathering on other airless rocky bodies (e.g. npFe). Compared to the Moon and S-type asteroids, MESSENGER's XRS and GRS found substantially less Fe, with less than 2 wt.% Fe across the surface. MESSENGER found that Mercury's reflectance spectrum lacks diagnostic ferrous absorption bands implying Mercury's surface is poor in ferrous iron. Mercury's surface is also S rich, with 0.5–4 wt.% S detected on the surface. Mercury Is also enriched in carbon, likely graphite, with up to 4 wt.% in the LRM (Klima et al., 2018). Currently, there have only been limited investigations into space weathering on Fe-poor, S-rich, and C-rich materials relevant to Mercury.

Space weathering processes can be simulated in the laboratory to explore microstructural, chemical, and spectral characteristics of hermean surface materials. Sasaki & Kurahashi (2004) performed nanosecond pulse laser irradiation experiments to simulate dust impact heating on olivine and pyroxene and found that reflectance spectra darkened (up to 50% for San Carlos olivine and up to 16% for Bamble enstatite both with 8–10 wt.% FeO) and reddened, which was caused by production of nanophase iron particles within vapor-deposited rims (Sasaki et al., 2001). Recent work by Thompson et al. (2021) investigated the effect of FeO in olivine on space weathering of graphite-olivine mixtures using nanosecond pulse laser irradiation. They found a strong correlation between Fe content, spectral slope, and simulated space weathering pulses such that the resulting spectra range from flat to strongly red-sloped (Thompson et al., 2021). Sulfide space weathering has also been investigated using pulse laser irradiation for troilite (FeS) (Loeffler et al., 2008), as well as using photon-stimulated desorption (PSD) for CaS (Bennett et al., 2016) and MgS (Schaible et al., 2020). They find that FeS and MgS preferentially lose S at velocities lower than the escape velocity, which may be the dominant sources of S^0 in the hermean exosphere since micrometeorite and solar wind sputtering produces S at abundances that are several orders of magnitude too low (Killen and Hahn, 2015). On the other hand, CaS preferentially loses Ca where simulations of Ca^0 exospheric density are ~100 times higher than what was measured by MESSENGER. CaS and MgS are of special interest because they are candidate hollows-forming material formed through sublimation during space weathering (Blewett et al., 2016; Thomas et al., 2014a).

Hollows

Hollows are unique landforms on the surface of Mercury characterized by rimless, flat-bottomed pits that are 10s of meters deep and typically have a bright halo around them (Blewett et al., 2011; Blewett et al., 2016; Blewett et al., 2013; Thomas et al., 2014a; Vilas et al., 2016; Xiao et al., 2013). They are thought to be produced by sublimation of a volatile-rich layer of rock in response to the intense solar wind Mercury experiences. They are largely associated with craters and impact basins in LRM (Blewett et al., 2018; Blewett et al., 2016; Blewett et al., 2013; Thomas et al., 2016; Thomas et al., 2014a), with the largest fraction occurring between 0-30 °N and within the "hot-pole" latitudes of 300–320 °E (Thomas et al., 2014a). Hollows are also preferentially found on Sun-facing slopes (Blewett et al., 2011; Blewett et al., 2013; Thomas et al., 2014a). Hollows are among the youngest non-impact features on Mercury, estimated to have formed at either 1 Ga (Blewett et al., 2011) or <270 Ma (Xiao et al., 2012). The hollows are associated with young rayed craters possessing crisp morphology and a lack of superimposed craters that would degrade the crisp rims and flat floors (Blewett et al., 2018).

Hollows are identified by their unique reflectance and morphological properties. At lower spatial resolution, hollows appear as high-reflectance patches that have a relatively shallow increase in spectral reflectance with wavelength in the VIS-NIR compared with the global average (Robinson et al., 2008). Hollows are also largely associated with LRM that are thought to be darkened by graphite (Klima et al., 2018). At higher spatial resolution, their geomorphological characteristics can be recognized as shallow, rimless, flat-floored depressions with irregular, rounded outlines. Hollows are relatively small features ranging from a few tens of meters to several kilometers in length, or in extensive fields (Blewett et al., 2016). In particular, their rimless and flat-floored nature, rather than a bowl- or v-shaped bottom, distinguish them from craters. These geomorphological characteristics are uncommon among rocky landforms, with similarities only to some features on icy surfaces on Mars (Moore et al., 1996), icy satellites (Moore et al., 1999), Ceres (Nathues et al., 2015), and Pluto (Moore et al., 2017), suggesting hollows form in a manner similar to "sublimation degradation." Sublimation degradation refers to the loss of volatile phases causing the remaining material to weaken and collapse in lateral scarps. However, the specific process(es) driving volatile loss for hollows formation is not known, with possibilities including sublimation driven by solar heating or contact with impact melt or volcanic eruption products,

destruction of volatile-bearing phases by solar UV flux, solar wind ions, or magnetospheric ions, or heating and vaporization by micrometeroid bombardment (Blewett et al., 2018).

Based on the elevated abundances of S and C at Mercury's surface, various sulfides and graphite have been proposed as hollows-forming material (Blewett et al., 2016). A spectral signature similar to MgS or CaS powders has been found in hollows at Dominici crater (Vilas et al., 2016) and have been investigated through experimental space weathering experiments (Bennett et al., 2016; Schaible et al., 2020). However, pure MgS and CaS have extremely high melting temperatures in excess of 2000 °C, making them refractory phases. If the MgS and CaS are not pure and contain substituting minor elements, those melting temperature can decrease dramatically. Alternatively, alkali-sulfides, including K- and Cl-bearing djerfisherite and Na-bearing caswellsilverite and schollhornite have been proposed as potential sublimates since they have lower melting temperatures (Blewett et al., 2011; Helbert et al., 2013; Renggli et al., 2022). Graphite has also been proposed with ion bombardment or conversion to methane (Blewett et al., 2016). Graphite itself is highly refractory as well, but ion bombardment from solar wind or the magnetosphere can sputter carbon, and proton irradiation could convert graphite to methane. Graphite as a hollows-forming material is also supported by its implication as the primary darkening agent on Mercury, its enrichment in the LRM, and the spatial association of LRM and hollows (Blewett et al., 2016; Klima et al., 2018; Thomas et al., 2016; Thomas et al., 2014a).

Polar deposits

Mercury's abundant polar deposits appear to be several meter thick deposits composed of nearly pure water ice. Observations from both Earth-based radar (Rivera-Valentín et al., 2022; Slade et al., 1992) and MESSENGER neutron spectrometer, laser altimetry, and direct imaging measurements (Chabot et al., 2018b; Deutsch et al., 2016) have found that these polar deposits are in permanently shadowed regions (PSRs), which are thermally stable environments for water ice on geologic timescales (Paige et al., 2013; Vasavada et al., 1999). Modelling of radar data suggest these deposits are ~95% water ice (Butler et al., 1993), and MESSENGER neutron spectrometer data are consistent with near pure water-ice (Lawrence et al., 2013). The majority of ice deposits are consistent with insulation by 10–30 cm of LRM (Lawrence et al., 2013) that are interpreted to be sublimation lag composed of carbon-rich material (e.g., Zhang and Paige, 2009). Images

(Chabot et al., 2016; Deutsch et al., 2016) and reflectance measurements (Neumann et al., 2013) also reveal that spatially coherent ice deposits with distinct albedos and sharp reflectance boundaries align with the boundaries of PSRs, contrary to the patchiness of lunar polar deposits that are best explained by long exposure times in the space weathering environment (Deutsch et al., 2019). Consequently, Mercury polar deposits are among the youngest geologic features with conservative ages suggesting ice was delivered or refreshed within the last ~330 Myr, likely from impactors (Deutsch et al., 2019). Low-altitude polar deposit observations from MESSENGER also found that polar deposits either have high reflectance consistent with exposed surface ice, or low reflectance consistent with a lag deposit, with the low reflectance boundaries having an ~400 m wide transition zone (Chabot et al., 2016; Deutsch et al., 2016).

The inference of young ages for polar ice deposits, observations that all of Mercury's available polar cold traps are occupied by volatiles, and agreement between brightness variations and modelled biannual maximum temperature all support the conclusion that a substantial source of volatiles in Mercury's polar deposits are exogenic, sourced from large comets or volatile-rich asteroids that impacted Mercury within the last few tens of millions of years or sourced from the continuous and ongoing delivery of primitive micrometeorites. A key insight from MESSENGER is that Mercury's polar deposits are dominantly, but not completely, water ice (Chabot et al., 2018a; Lawrence et al., 2013; Paige et al., 2013), necessitating the presence of other volatile elements such as simple organic compounds (Paige et al., 2013; Zhang and Paige, 2009) or elemental S (Sprague et al., 1995). The presence of volatiles other than water ice provides evidence for a potential endogenic contribution from outgassing of volatiles from Mercury's interior through processes such as volcanic eruptions or liberation from crustal rocks by micrometeorites or large impact events (Chabot et al., 2018a; Deutsch et al., 2019; Deutsch et al., 2021). Another potential source of water-ice in polar deposits comes from interactions of surface regolith with protons from the solar wind, which would produce OH or H_2O, but not other volatiles (McCord et al., 2011).

The volatile-rich polar deposits on Mercury place critical constraints on the survivability and inevitability of water-rich ice deposits on the surfaces of airless planetary bodies, even bodies in close proximity to their host star. Direct measurement of those ices either by a future lander or in a lab on Earth after sample return could provide important constraints on the sources and processes of those volatiles, including the timescales over which they can survive at the surface.

Exosphere

Mercury is unique among the terrestrial planets in that it has a tenuous, surface bounded exosphere instead of a permanent, large atmosphere. An exosphere is defined as a thin gaseous atmospheric layer around a planetary body, bound by gravity, but where the gas density is so low that the particles are collisionless. Mercury's exosphere is produced through interactions of the surface with solar wind and meteorite impacts. Mercury's exosphere is known from Mariner 10 and MESSENGER data to consist of H, He, Na, K, Ca, and Mg along with Al and Mn (Killen et al., 2007; McClintock et al., 2008; McClintock et al., 2009; Merkel et al., 2017; Vervack et al., 2016; Vervack et al., 2010; Zurbuchen et al., 2008). H and He are lost through thermal escape as temperatures are high enough for atoms to reach their escape velocity, but all other elements identified in Mercury's exosphere must be lost through non-thermal escape, sticking to the surface of Mercury or entrainment into solar wind after photoionization (Killen et al., 2007). Oxygen was detected by Mariner 10 but not MESSENGER, which suggests O content either changed dramatically or there was an error in the first detections (Vervack et al., 2016). The Ultraviolet and Visible Spectrometer (UV-VIS) and Mercury Atmospheric and Surface Composition Spectrometer (MASCS) instruments on MESSENGER were used to map the distributions and seasonal variations of these constituents. The abundances, distributions, and seasonal variations for many of these elements are distinct, which suggests different source, transport, and loss processes (Merkel et al., 2017). Understanding the production of Mercury's exosphere can therefore allow inferences to be made about the surface chemistry and mineralogy.

Of the elements measured in Mercury's exosphere, Na, K, Ca, and Mg have been the most extensively studied. The sodium tail, which is escaping away from the Sun primarily due to radiation-pressure induced acceleration, was first imaged by Potter et al. (2002) and is remarkably constant. A northern enhancement in Na was observed in the second MESSENGER flyby, while in contrast Ca and Mg were enhanced at northern latitudes during the third flyby indicating different source processes, although this could be due to observational bias (Potter et al., 2006). Na content is also spatially variable on the surface, ranging from 2.8 wt.% at low northern latitudes (0–15°) to 4.9 wt.% at high latitudes (80–90° N), which may be due to preferential deposition at cold poles (Peplowski et al., 2014). Ca was observed to vary over yearly timescales and is highly concentrated in the dawn equatorial region (McClintock et al., 2009). Interestingly, an

enhancement in the Mg exosphere was observed over the Mg-rich geochemical terrane, providing the first direct link between surface regolith and the exosphere (Merkel et al., 2018).

Future Exploration of Mercury

Centuries of ground-based telescopic and orbital spacecraft observation have revealed a wealth of geochemical information about the planet Mercury. Those observations have revealed that Mercury is a geochemical endmember amongst the terrestrial planets, and to understand hermean geochemistry requires us to recalibrate our understanding of the geochemical behavior of the elements. Although we have gained much knowledge, there are still many open or poorly constrained questions that are fundamental to understanding Mercury's origin and its subsequent thermochemical evolution. Among the most pressing questions are the origin of Mercury's large core and the mineralogical make-up of its silicate mantle and crust. These questions require additional experimental and modeling work that can be completed today, but they also require the continued exploration of Mercury, to obtain better constraints and new datasets on hermean geochemistry.

BepiColombo will reach orbital insertion around Mercury in late 2025 (Benkhoff et al., 2021), representing our next great opportunity to gain new insights into the geochemistry of the innermost planet. BepiColombo has a suite of geochemical instruments that it will use to gather data across the surface of Mercury, particularly at a much greater resolution at the southern hemisphere than was possible with MESSENGER (Benkhoff et al., 2021; Rothery et al., 2020). Looking beyond BepiColombo, a Mercury lander could provide detailed insights into the surface of Mercury that are not possible from orbit, including a direct assessment of surface mineralogy by X-ray diffraction and chemical compositions of individual parcels of regolith or rocks (Ernst et al., 2022). Furthermore, insights into hermean surface volatiles, including the potential inventory of organics in permanently shadowed craters, would be particularly compelling targets for future exploration (e.g., Lawrence et al., 2013; Neumann et al. 2013; Paige et al., 2013). The greatest knowledge gains in hermean geochemistry will come through the study of samples, either through the identification of a hermean meteorite or from a Mercury sample return mission (Vander Kaaden et al., 2019). Regardless of what the future holds for Mercury exploration, it is already an important

endmember for understanding terrestrial planets in our own solar system, and it provides key insights into exoplanetary systems as well.

Acknowledgements

We are grateful to Sujoy Mukhopadhyay for the editorial handling of this chapter and to an anonymous reviewer that provided constructive and helpful comments that improved the overall quality of this work. We also thank Kathleen Vander Kaaden, Gordon Moore, Kayla Iacovino, Kelsey Prissel, Jeremy Boyce, and Kevin Righter for constructive feedback and helpful discussions during the course of writing this chapter. We also thank the MESSENGER Science Team for collecting much of the data that made this chapter possible. F.M.M. was supported by NASA's Planetary Science Division Research Program, through the Process Simulation ISFM work package at Johnson Space Center. B.A.A. was supported, in part, by NASA's Emerging Worlds Program and, in part, by the JETS contract at NASA Johnson Space Center.

References

Albarède, F., Albalat, E. and Lee, C.T.A. (2015) An intrinsic volatility scale relevant to the Earth and Moon and the status of water in the Moon. Meteoritics & Planetary Science 50, 568-577.

Anderson, J.D., Colombo, G., Esposito, P.B., Lau, E.L. and Trager, G.B. (1987) The mass, gravity field, and ephemeris of Mercury. Icarus 71, 337-349.

Anzures, B.A., Parman, S.W., Milliken, R.E., Namur, O., Cartier, C. and Wang, S. (2020) Effect of sulfur speciation on chemical and physical properties of very reduced mercurian melts. Geochimica et Cosmochimica Acta 286, 1-18.

Anzures B.A., McCubbin F.M., Erickson T.M., Jakubek R.S., Fries M.D., Le L. (In Press) First widespread occurrence of rare phosphate chladniite in a meteorite, winonaite Graves Nunataks (GRA) 12510: implications for phosphide – phosphate redox buffered genesis in meteorites. American Mineralogist, doi: 10.2138/am-2023-9195.

Ash, M.E., Shapiro, I.I. and Smith, W.B. (1967) Astronomical constants and planetary ephemerides deduced from radar and optical observations. Astronomical Journal 72, 338-350.

Ash, M.E., Shapiro, I.I. and Smith, W.B. (1971) The System of Planetary Masses. Science 174, 551-556.

Asphaug, E. and Reufer, A. (2014) Mercury and other iron-rich planetary bodies as relics of inefficient accretion. Nature Geoscience 7, 564-568.

Benedix, G.K., Lauretta, D.S., and McCoy, T.J. (2005) Thermodynamic constraints on the formation conditions of winonaites and silicate-bearing IAB irons. Geochimica et Cosmochimica Acta, 69, 5123-5131.

Benkhoff, J., Murakami, G., Baumjohann, W., Besse, S., Bunce, E., Casale, M., Cremosese, G., Glassmeier, K.H., Hayakawa, H., Heyner, D., Hiesinger, H., Huovelin, J., Hussmann, H., Iafolla, V., Iess, L., Kasaba, Y., Kobayashi, M., Milillo, A., Mitrofanov, I.G., Montagnon, E., Novara, M., Orsini, S., Quemerais, E., Reininghaus, U., Saito, Y., Santoli, F., Stramaccioni, D., Sutherland, O., Thomas, N., Yoshikawa, I. and Zender, J. (2021) BepiColombo–Mission Overview and Science Goals. Space Science Reviews 217, 90.

Bennett, C.J., McLain, J.L., Sarantos, M., Gann, R.D., DeSimone, A. and Orlando, T.M. (2016) Investigating potential sources of Mercury's exospheric Calcium: Photon-stimulated desorption of Calcium Sulfide. Journal of Geophysical Research: Planets 121, 137-146.

Benz, W., Anic, A., Horner, J. and Whitby, J.A. (2007) The origin of mercury. Space Science Reviews 132, 189-202.

Benz, W., Slattery, W.L. and Cameron, A.G.W. (1988) Collisional stripping of Mercury's mantle. Icarus 74, 516-528.

Berrada, M., Secco, R.A. and Yong, W. (2022) Resistivity of solid and liquid Fe–Ni–Si with applications to the cores of Earth, Mercury and Venus. Scientific Reports 12, 9941.

Berthet, S., Malavergne, V. and Righter, K. (2009) Melting of the Indarch meteorite (EH4 chondrite) at 1 gPa and variable oxygen fugacity: Implications for early planetary differentiation processes. Geochimica Et Cosmochimica Acta 73, 6402-6420.

Blewett, D.T., Chabot, N.L., Denevi, B.W., Ernst, C.M., Head, J.W., Izenberg, N.R., Murchie, S.L., Solomon, S.C., Nittler, L.R., McCoy, T.J., Xiao, Z., Baker, D.M.H., Fassett, C.I., Braden, S.E., Oberst, J., Scholten, F., Preusker, F. and Hurwitz, D.M. (2011) Hollows on Mercury: MESSENGER Evidence for Geologically Recent Volatile-Related Activity. Science 333, 1856-1859.

Blewett, D.T., Ernst, C.M., Murchie, S.L. and Vilas, F. (2018) Mercury's hollows, in: Solomon, S.C., Nittler, L.R., Anderson, B.J. (Eds.), Mercury: The view after MESSENGER. Cambridge University Press, Cambridge, UK, pp. 324-345.

Blewett, D.T., Lucey, P.G., Hawke, B.R., Ling, G.G. and Robinson, M.S. (1997) A comparison of Mercurian reflectance and spectral quantities with those of the Moon. Icarus 129, 217-231.

Blewett, D.T., Stadermann, A.C., Susorney, H.C., Ernst, C.M., Xiao, Z.Y., Chabot, N.L., Denevi, B.W., Murchie, S.L., McCubbin, F.M., Kinczyk, M.J., Gillis-Davis, J.J. and Solomon, S.C. (2016) Analysis of MESSENGER high-resolution images of Mercury's hollows and implications for hollow formation. Journal of Geophysical Research-Planets 121, 1798-1813.

Blewett, D.T., Vaughan, W.M., Xiao, Z.Y., Chabot, N.L., Denevi, B.W., Ernst, C.M., Helbert, J., D'Amore, M., Maturilli, A., Head, J.W. and Solomon, S.C. (2013) Mercury's hollows: Constraints on formation and composition from analysis of geological setting and spectral reflectance. Journal of Geophysical Research-Planets 118, 1013-1032.

Bouhifd, M.A., Gautron, L., Bolfan-Casanova, N., Malavergne, V., Hammouda, T., Andrault, D. and Jephcoat, A.P. (2007) Potassium partitioning into molten iron alloys at high-pressure: Implications for Earth's core. Physics of the Earth and Planetary Interiors 160, 22-33.

Boujibar, A., Andrault, D., Bouhifd, M.A., Bolfan-Casanova, N., Devidal, J.L. and Trcera, N. (2014) Metal-silicate partitioning of sulphur, new experimental and thermodynamic constraints on planetary accretion. Earth and Planetary Science Letters 391, 42-54.

Boujibar, A., Habermann, M., Righter, K., Ross, D.K., Pando, K., Righter, M., Chidester, B.A. and Danielson, L.R. (2019) U, Th, and K partitioning between metal, silicate, and sulfide and implications for Mercury's structure, volatile content, and radioactive heat production. American Mineralogist 104, 1221-1237.

Boukaré, C.-E., Parman, S.W., Parmentier, E.M. and Anzures, B.A. (2019) Production and Preservation of Sulfide Layering in Mercury's Mantle. Journal of Geophysical Research: Planets 124, 3354-3372.

Boyce, J.W., McCubbin, F.M., Lunning, N., and Anderson, T. (2024) Large carbonaceous chondrite parent bodies favored by abundance–volatility modeling: A possible chemical signature of pebble accretion. The Planetary Science Journal, 5, 53, doi: 10.3847/PSJ/ad1830.

Boyet, M. and Carlson, R.W. (2006) A new geochemical model for the Earth's mantle inferred from ^{146}Sm–^{142}Nd systematics. Earth and Planetary Science Letters, 250, 254-268.

Boynton, W.V., Taylor, G.J., Evans, L.G., Reedy, R.C., Starr, R., Janes, D.M., Kerry, K.E., Drake, D.M., Kim, K.J., Williams, R.M.S., Crombie, M.K., Dohm, J.M., Baker, V., Metzger, A.E., Karunatillake, S., Keller, J.M., Newsom, H.E., Arnold, J.R., Bruckner, J., Englert, P.A.J., Gasnault, O., Sprague, A.L., Mitrofanov, I., Squyres, S.W., Trombka, J.I., d'Uston, L., Wanke, H. and Hamara, D.K. (2007) Concentration of H, Si, Cl, K, Fe, and Th in the low- and mid-latitude regions of Mars. Journal of Geophysical Research-Planets 112.

Braukmüller, N., Wombacher, F., Hezel, D. C., Escoube, R., and Münker, C. (2018) The chemical composition of carbonaceous chondrites: Implications for volatile element depletion, complementarity and alteration. Geochimica et Cosmochimica Acta, 239, 17–48.

Broadfoot, A.L., Kumar, S., Belton, M.J.S. and McElroy, M.B. (1974) Mercury's Atmosphere from Mariner 10: Preliminary Results. Science 185, 166-169.

Brounce, M., Boyce, J.W. and McCubbin, F.M. (2022) Sulfur in apatite from the Nakhla meteorite record a late-stage oxidation event. Earth and Planetary Science Letters 595, 117784.

Brown, S.M. and Elkins-Tanton, L.T. (2009) Compositions of Mercury's earliest crust from magma ocean models. Earth and Planetary Science Letters 286, 446-455.

Burbine, T.H., McCoy, T.J., Nittler, L.R., Benedix, G.K., Cloutis, E.A. and Dickinson, T.L. (2002) Spectra of extremely reduced assemblages: Implications for Mercury. Meteoritics & Planetary Science 37, 1233-1244.

Butler, B.J., Muhleman, D.O. and Slade, M.A. (1993) Mercury: full-disk radar images and the detection and stability of ice at the North Pole. Journal of Geophysical Research: Planets 98, 15003-15023.

Byrne, P.K., Ostrach, L.R., Fassett, C.I., Chapman, C.R., Denevi, B.W., Evans, A.J., Klimczak, C., Banks, M.E., Head, J.W. and Solomon, S.C. (2016) Widespread effusive volcanism on Mercury likely ended by about 3.5Ga. Geophysical Research Letters 43, 7408-7416.

Byrne, P.K., Whitten, J.L., Klimczak, C., McCubbin, F.M. and Ostrach, L.R. (2018) The volcanic character of Mercury, in: Solomon, S.C., Nittler, L.R., Anderson, B.J. (Eds.), Mercury: The View after MESSENGER. Cambridge University Press, Cambridge, United Kingdom, pp. 287-323.

Cameron, A.G.W., Fegley, B., Benz, W. and Slattery (1988) The strange density of Mercury: Theoretical considerations, in: Vilas, F., Chapman, C.R., Matthews, M.S. (Eds.), Mercury. University of Arizona Press, Tuscon, AZ, pp. 692-708.

Canup, R.M. and Asphaug, E. (2001) Origin of the Moon in a giant impact near the end of the Earth's formation. Nature, 412, 708-712.

Caro, G., Bourdon, B., Halliday, A.N., and Quitté, G. (2008) Super-chondritic Sm/Nd ratios in Mars, the Earth and the Moon. Nature, 452, 336-339.

Cartier, C., Namur, O., Nittler, L.R., Weider, S.Z., Crapster-Pregont, E., Vorburger, A., Frank, E.A. and Charlier, B. (2020) No FeS layer in Mercury? Evidence from Ti/Al measured by MESSENGER. Earth and Planetary Science Letters 534, 116108.

Cartier, C. and Wood, B.J. (2019) The Role of Reducing Conditions in Building Mercury. Elements 15, 39-45.

Casanova, I., Keil, K. and Newsom, H.E. (1993) Composition of metal in Aubrites: Constraints on core formation. Geochimica Et Cosmochimica Acta 57, 675-682.

Chabot, N.L., Ernst, C.M., Denevi, B.W., Nair, H., Deutsch, A.N., Blewett, D.T., Murchie, S.L., Neumann, G.A., Mazarico, E., Paige, D.A., Harmon, J.K., Head, J.W. and Solomon, S.C. (2014a) Images of surface volatiles in Mercury's polar craters acquired by the MESSENGER spacecraft. Geology 42, 1051-1054.

Chabot, N.L., Ernst, C.M., Paige, D.A., Nair, H., Denevi, B.W., Blewett, D.T., Murchie, S.L., Deutsch, A.N., Head, J.W. and Solomon, S.C. (2016) Imaging Mercury's polar deposits during MESSENGER's low-altitude campaign. Geophysical Research Letters 43, 9461-9468.

Chabot, N.L., J., L.D., Neumann, G.A., Feldman, W.C. and Paige, D.A. (2018a) Mercury's polar deposits, in: Solomon, S.C., Nittler, L.R., Anderson, B.J. (Eds.), Mercury: The view after MESSENGER. Cambridge University Press, Cambridge, UK, pp. 346-370.

Chabot, N.L., Shread, E.E. and Harmon, J.K. (2018b) Investigating Mercury's South Polar Deposits: Arecibo Radar Observations and High-Resolution Determination of Illumination Conditions. Journal of Geophysical Research-Planets 123, 666-681.

Chabot, N.L., Wollack, E.A., Klima, R.L. and Minitti, M.E. (2014b) Experimental constraints on Mercury's core composition. Earth and Planetary Science Letters 390, 199-208.

Chabot, N.L., Wollack, E.A., Humayun, M., and Shank, E.M. (2015) The effect of oxygen as a light element in metallic liquids on partitioning behavior. Meteoritics & Planetary Science 50, 530-546.

Charlier, B., Grove, T.L., Namur, O. and Holtz, F. (2018) Crystallization of the lunar magma ocean and the primordial mantle-crust differentiation of the Moon. Geochimica et Cosmochimica Acta 234, 50-69.

Charlier, B., Grove, T.L. and Zuber, M.T. (2013) Phase equilibria of ultramafic compositions on Mercury and the origin of the compositional dichotomy. Earth and Planetary Science Letters 363, 50-60.

Chase, M.W. (1998) NIST-JANAF Thermochemical Tables. National Institute of Standards and Technology, Gaithersburg, MD.

Chen, B., Li, J. and Hauck II, S.A. (2008) Non-ideal liquidus curve in the Fe-S system and Mercury's snowing core. Geophysical Research Letters 35.

Christensen, U.R. and Wicht, J. (2008) Models of magnetic field generation in partly stable planetary cores: Applications to Mercury and Saturn. Icarus 196, 16-34.

Cintala, M.J. (1992) Impact-induced thermal effects in the lunar and mercurian regoliths. Journal of Geophysical Research-Planets 97, 947-973.

Cottrell, E., Kelley, K.A., Lanzirotti, A. and Fischer, R.A. (2009) High-precision determination of iron oxidation state in silicate glasses using XANES. Chemical Geology 268, 167-179.

Cottrell, E. and Kelley, K.A. (2011) The oxidation state of Fe in MORB glasses and the oxygen fugacity of the upper mantle. Earth and Planetary Science Letters, 305, 270-282.

Crozaz, G. and Lundberg, L.L. (1995) The origin of oldhamite in unequilibrated enstatite chondrites. Geochimica et Cosmochimica Acta 59, 3817-3831.

Dasgupta, R., Chi, H., Shimizu, N., Buono, A.S. and Walker, D. (2013) Carbon solution and partitioning between metallic and silicate melts in a shallow magma ocean: Implications for the origin and distribution of terrestrial carbon. Geochimica et Cosmochimica Acta 102, 191-212.

Dasgupta, R., Falksen, E., Pal, A. and Sun, C. (2022) The fate of nitrogen during parent body partial melting and accretion of the inner solar system bodies at reducing conditions. Geochimica et Cosmochimica Acta 336, 291-307.

Delitsky, M.L., Paige, D.A., Siegler, M.A., Harju, E.R., Schriver, D., Johnson, R.E. and Travnicek, P. (2017) Ices on Mercury: Chemistry of volatiles in permanently cold areas of Mercury's north polar region. Icarus 281, 19-31.

Denevi, B.W., Ernst, C.M., Meyer, H.M., Robinson, M.S., Murchie, S.L., Whitten, J.L., Head, J.W., Watters, T.R., Solomon, S.C., Ostrach, L.R., Chapman, C.R., Byrne, P.K., Klimczak, C. and Peplowski, P.N. (2013) The distribution and origin of smooth plains on Mercury. Journal of Geophysical Research-Planets 118, 891-907.

Denevi, B.W. and Robinson, M.S. (2008) Mercury's albedo from Mariner 10: Implications for the presence of ferrous iron. Icarus 197, 239-246.

Denevi, B.W., Robinson, M.S., Solomon, S.C., Murchie, S.L., Blewett, D.T., Domingue, D.L., McCoy, T.J., Ernst, C.M., Head, J.W., Watters, T.R. and Chabot, N.L. (2009) The Evolution of Mercury's Crust: A Global Perspective from MESSENGER. Science 324, 613-618.

Deng, L.W., Fei, Y.W., Liu, X., Gong, Z.Z. and Shahar, A. (2013) Effect of carbon, sulfur and silicon on iron melting at high pressure: Implications for composition and evolution of the planetary terrestrial cores. Geochimica Et Cosmochimica Acta 114, 220-233.

Deutsch, A.N., Chabot, N.L., Mazarico, E., Ernst, C.M., Head, J.W., Neumann, G.A. and Solomon, S.C. (2016) Comparison of areas in shadow from imaging and altimetry in the north polar region of Mercury and implications for polar ice deposits. Icarus 280, 158-171.

Deutsch, A.N., Head, J.W. and Neumann, G.A. (2019) Age constraints of Mercury's polar deposits suggest recent delivery of ice. Earth and Planetary Science Letters 520, 26-33.

Deutsch, A.N., Head, J.W., Parman, S.W., Wilson, L., Neumann, G.A. and Lowden, F. (2021) Degassing of volcanic extrusives on Mercury: Potential contributions to transient atmospheres and buried polar deposits. Earth and Planetary Science Letters 564, 116907.

Dickinson, T.L. and McCoy, T.J. (1997) Experimental rare-earth-element partitioning in oldhamite: Implications for the igneous origin of aubritic oldhamite. Meteoritics & Planetary Science 32, 395-412.

Domingue, D.L., Chapman, C.R., Killen, R.M., Zurbuchen, T.H., Gilbert, J.A., Sarantos, M., Benna, M., Slavin, J.A., Schriver, D., Travnicek, P.M., Orlando, T.M., Sprague, A.L., Blewett, D.T., Gillis-Davis, J.J., Feldman, W.C., Lawrence, D.J., Ho, G.C., Ebel, D.S., Nittler, L.R., Vilas, F., Pieters, C.M., Solomon, S.C., Johnson, C.L., Winslow, R.M., Helbert, J., Peplowski, P.N., Weider, S.Z., Mouawad, N., Izenberg, N.R. and McClintock, W.E. (2014) Mercury's Weather-Beaten Surface: Understanding Mercury in the Context of Lunar and Asteroidal Space Weathering Studies. Space Science Reviews 181, 121-214.

Drake, M.J. and Righter, K. (2002) Determining the composition of the Earth. Nature 416, 39-44.

Dreibus, G., Kruse, H., Spettel, B. and Wänke, H. (1977) The bulk composition of the Moon and eucrite parent body, Proceedings of the 8th Lunar Science Conference. Lunar and Planetary Institute, Houston, TX, pp. 211-227.

Dreibus, G. and Wänke, H. (1985) Mars, a Volatile-Rich Planet. Meteoritics 20, 367-381.

Dumoulin, C., Tobie, G., Verhoeven, O., Rosenblatt, P. and Rambaux, N. (2017) Tidal constraints on the interior of Venus. Journal of Geophysical Research: Planets 122, 1338-1352.

Dygert, N., Lin, J.-F., Marshall, E.W., Kono, Y. and Gardner, J.E. (2017) A Low Viscosity Lunar Magma Ocean Forms a Stratified Anorthitic Flotation Crust With Mafic Poor and Rich Units. Geophysical Research Letters 44, 11,282-211,291.

Ebel, D.S. and Sack, R.O. (2013) Djerfisherite: nebular source of refractory potassium. Contributions to Mineralogy and Petrology 166, 923-934.

Ebel, D.S. and Stewart, S.T. (2018) The elusive origin of Mercury, in: Solomon, S.C., Nittler, L.R., Anderson, B.J. (Eds.), Mercury: The view after MESSENGER. Cambridge University Press, Cambridge, UK, pp. 497-515.

Edmund, E., Morard, G., Baron, M.A., Rivoldini, A., Yokoo, S., Boccato, S., Hirose, K., Pakhomova, A. and Antonangeli, D. (2022) The Fe-FeSi phase diagram at Mercury's core conditions. Nature Communications 13, 387.

Ehlmann, B.L., Anderson, F.S., Andrews-Hanna, J., Catling, D.C., Christensen, P.R., Cohen, B.A., Dressing, C.D., Edwards, C.S., Elkins-Tanton, L.T., Farley, K.A., Fassett, C.I., Fischer, W.W., Fraeman, A.A., Golombek, M.P., Hamilton, V.E., Hayes, A.G., Herd, C.D.K., Horgan, B., Hu, R., Jakosky, B.M., Johnson, J.R., Kasting, J.F., Kerber, L., Kinch, K.M., Kite, E.S., Knutson, H.A., Lunine, J.I., Mahaffy, P.R., Mangold, N., McCubbin, F.M., Mustard, J.F., Niles, P.B., Quantin-Nataf, C., Rice, M.S., Stack, K.M., Stevenson, D.J., Stewart, S.T., Toplis, M.J., Usui, T., Weiss, B.P., Werner, S.C., Wordsworth, R.D., Wray, J.J., Yingst, R.A., Yung, Y.L. and Zahnle, K.J. (2016) The sustainability of habitability on terrestrial planets: Insights,

questions, and needed measurements from Mars for understanding the evolution of Earth-like worlds. Journal of Geophysical Research-Planets 121, 1927-1961.
Ehlmann, B.L., Mustard, J.F., Murchie, S.L., Poulet, F., Bishop, J.L., Brown, A.J., Calvin, W.M., Clark, R.N., Des Marais, D.J., Milliken, R.E., Roach, L.H., Roush, T.L., Swayze, G.A. and Wray, J.J. (2008) Orbital Identification of Carbonate-Bearing Rocks on Mars. Science 322, 1828-1832.
Einstein, V.A. (1915) Die Feldgleichungen der Gravitation. Sitzungsberichte der Königlich Preußischen Akademie der Wissenschaften, 844-847.
Elardo, S.M., Draper, D.S. and Shearer, C.K. (2011) Lunar magma ocean crystallization revisited: Bulk composition, early cumulate mineralogy, and the source regions of the highlands Mg-suite. Geochimica Et Cosmochimica Acta 75, 3024-3045.
Elardo, S.M., Shearer, C.K., Kaaden, K.E.V., McCubbin, F.M. and Bell, A.S. (2015) Petrogenesis of primitive and evolved basalts in a cooling Moon: Experimental constraints from the youngest known lunar magmas. Earth and Planetary Science Letters 422, 126-137.
Elkins-Tanton, L.T. (2012) Magma Oceans in the Inner Solar System, in: Jeanloz, R. (Ed.), Annual Review of Earth and Planetary Sciences, Vol 40, pp. 113-139.
Elkins-Tanton, L.T., Burgess, S. and Yin, Q.-Z. (2011) The lunar magma ocean: Reconciling the solidification process with lunar petrology and geochronology. Earth and Planetary Science Letters 304, 326-336.
Elkins-Tanton, L.T. and Grove, T.L. (2011) Water (hydrogen) in the lunar mantle: Results from petrology and magma ocean modeling. Earth and Planetary Science Letters 307, 173-179.
Elkins-Tanton, L.T., Hess, P.C. and Parmentier, E.M. (2005a) Possible formation of ancient crust on Mars through magma ocean processes. Journal of Geophysical Research-Planets 110.
Elkins-Tanton, L.T., Parmentier, E.M. and Hess, P.C. (2003) Magma ocean fractional crystallization and cumulate overturn in terrestrial planets: Implications for Mars. Meteoritics & Planetary Science 38, 1753-1771.
Elkins-Tanton, L.T., Van Orman, J.A., Hager, B.H. and Grove, T.L. (2002) Re-examination of the lunar magma ocean cumulate overturn hypothesis: melting or mixing is required. Earth and Planetary Science Letters 196, 239-249.
Elkins-Tanton, L.T., Zaranek, S.E., Parmentier, E.M. and Hess, P.C. (2005b) Early magnetic field and magmatic activity on Mars from magma ocean cumulate overturn. Earth and Planetary Science Letters 236, 1-12.
Ernst, C.M., Chabot, N.L., Klima, R.L., Kubota, S., Rogers, G., Byrne, P.K., Hauck, S.A., Vander Kaaden, K.E., Vervack, R.J., Besse, S., Blewett, D.T., Denevi, B.W., Goossens, S., Indyk, S.J., Izenberg, N.R., Johnson, C.L., Jozwiak, L.M., Korth, H., McNutt, R.L., Murchie, S.L., Peplowski, P.N., Raines, J.M., Rampe, E.B., Thompson, M.S. and Weider, S.Z. (2022) Science Goals and Mission Concept for a Landed Investigation of Mercury. The Planetary Science Journal 3, 68.
Ettmayer, P., Kieffer, R. and Hattinger, F. (1974) Determination of melting points of metal nitrides under nitrogen pressure. Metall 28, 1151-1156.
Evans, L.G., Peplowski, P.N., McCubbin, F.M., McCoy, T.J., Nittler, L.R., Zolotov, M.Y., Ebel, D.S., Lawrence, D.J., Starr, R.D., Weider, S.Z. and Solomon, S.C. (2015) Chlorine on the surface of Mercury: MESSENGER gamma-ray measurements and implications for the planet's formation and evolution. Icarus 257, 417-427.
Evans, L.G., Peplowski, P.N., Rhodes, E.A., Lawrence, D.J., McCoy, T.J., Nittler, L.R., Solomon, S.C., Sprague, A.L., Stockstill-Cahill, K.R., Starr, R.D., Weider, S.Z., Boynton, W.V., Hamara, D.K. and Goldsten, J.O. (2012) Major-element abundances on the surface of Mercury: Results from the MESSENGER Gamma-Ray Spectrometer. Journal of Geophysical Research-Planets 117, E00L07.
Filiberto, J. (2014) Magmatic diversity on Venus: Constraints from terrestrial analog crystallization experiments. Icarus, 231, 131-136.
Floss, C. and Crozaz, G. (1993) Heterogeneous REE patterns in oldhamite from Aubrites: Their nature and origin. Geochimica Et Cosmochimica Acta 57, 4039-4057.
Floss, C., Strait, M.M. and Crozaz, G. (1990) Rare earth elements and the petrogenesis of aubrites. Geochimica Et Cosmochimica Acta 54, 3553-3558.
Fogel, R.A., Hess, P.C., and Rutherford, M.J. (1989) Intensive parameters of enstatite chondrite metamorphism. Geochimica et Cosmochimica Acta, 53, 2735-2746.
Fogel, R.A. (1997) On the significance of diopside and oldhamite in enstatite chondrites and aubrites. Meteoritics & Planetary Science 32, 577-591.
Fogel, R.A. (2005) Aubrite basalt vitrophyres: The missing basaltic component and high-sulfur silicate melts. Geochimica Et Cosmochimica Acta 69, 1633-1648.

Frank, E.A., Potter, R.W.K., Abramov, O., James, P.B., Klima, R.L., Mojzsis, S.J. and Nittler, L.R. (2017) Evaluating an impact origin for Mercury's high-magnesium region. Journal of Geophysical Research-Planets 122, 614-632.

Fuchs, L.H. (1966) Djerfisherite alkali copper-iron sulfide: A new mineral from enstatite chondrites. Science 153, 166-.

Füri, E. and Marty, B. (2015) Nitrogen isotope variations in the Solar System. Nature Geoscience 8, 515-522.

Franch, B.M. and Eugster, H.P. (1965) Experimental control of oxygen fugacities by graphite-gas equilibriums. Journal of Geophysical research, 70, 1529-1539.

Gannoun, A., Boyet, M., El Goresy, A. and Devouard, B. (2011) REE and actinide microdistribution in Sahara 97072 and ALHA77295 EH3 chondrites: A combined cosmochemical and petrologic investigation. Geochimica et Cosmochimica Acta 75, 3269-3289.

Gessmann, C.K., Wood, B.J., Rubie, D.C. and Kilburn, M.R. (2001) Solubility of silicon in liquid metal at high pressure: implications for the composition of the Earth's core. Earth and Planetary Science Letters 184, 367-376.

Goldschmidt, V.M. (1937) The principles of distribution of chemical elements in minerals and rocks. The seventh Hugo Muller Lecture, delivered before the Chemical Society on March 17th, 1937. Journal of the Chemical Society, 655-673.

Goodrich, C.A., Sutton, S.R., Wirick, S., and Jercinovic, M.J. (2013) Chromium valences in ureilite olivine and implications for ureilite petrogenesis. Geochimica et Cosmochimica Acta, 122, 280-305.

Halliday, A.N. (2013) The origins of volatiles in the terrestrial planets. Geochimica et Cosmochimica Acta. 105, 146–171.

Hammouda, T., Boyet, M., Frossard, P. and Cartier, C. (2022) The message of oldhamites from enstatite chondrites. Progress in Earth and Planetary Science 9, 13.

Hanson, B. and Jones, J.H. (1998) The systematics of Cr^{3+} and Cr^{2+} partitioning between olivine and liquid in the presence of spinel. American Mineralogist 83, 669-684.

Hauck II, S.A., Margot, J.-L., Solomon, S.C., Phillips, R.J., Johnson, C.L., Lemoine, F.G., Mazarico, E., McCoy, T.J., Padovan, S., Peale, S.J., Perry, M.E., Smith, D.E. and Zuber, M.T. (2013) The curious case of Mercury's internal structure. Journal of Geophysical Research: Planets 118, 1204-1220.

Hauck, S.A. and Johnson, C.L. (2019) Mercury: Inside the Iron Planet. Elements 15, 21-26.

Head, J.W., Chapman, C.R., Strom, R.G., Fassett, C.I., Denevi, B.W., Blewett, D.T., Ernst, C.M., Watters, T.R., Solomon, S.C., Murchie, S.L., Prockter, L.M., Chabot, N.L., Gillis-Davis, J.J., Whitten, J.L., Goudge, T.A., Baker, D.M.H., Hurwitz, D.M., Ostrach, L.R., Xiao, Z., Merline, W.J., Kerber, L., Dickson, J.L., Oberst, J., Byrne, P.K., Klimczak, C. and Nittler, L.R. (2011) Flood Volcanism in the Northern High Latitudes of Mercury Revealed by MESSENGER. Science 333, 1853-1856.

Head, J.W., Murchie, S.L., Prockter, L.M., Robinson, M.S., Solomon, S.C., Strom, R.G., Chapman, C.R., Watters, T.R., McClintock, W.E., Blewett, D.T. and Gillis-Davis, J.J. (2008) Volcanism on Mercury: Evidence from the first MESSENGER flyby. Science 321, 69-72.

Head, J.W., Murchie, S.L., Prockter, L.M., Solomon, S.C., Chapman, C.R., Strom, R.G., Watters, T.R., Blewett, D.T., Gillis-Davis, J.J., Fassett, C.I., Dickson, J.L., Morgan, G.A. and Kerber, L. (2009) Volcanism on Mercury: Evidence from the first MESSENGER flyby for extrusive and explosive activity and the volcanic origin of plains. Earth and Planetary Science Letters 285, 227-242.

Helbert, J., Maturilli, A. and D'Amore, M. (2013) Visible and near-infrared reflectance spectra of thermally processed synthetic sulfides as a potential analog for the hollow forming materials on Mercury. Earth and Planetary Science Letters 369-370, 233-238.

Helffrich, G., Brasser, R. and Shahar, A. (2019) The chemical case for Mercury mantle stripping. Progress in Earth and Planetary Science 6, 66.

Herd, C.D.K. (2008) Basalts as probes of planetary interior redox state. Oxygen in the Solar System 68, 527-553.

Herd, C.D.K., Borg, L.E., Jones, J.H. and Papike, J.J. (2002) Oxygen fugacity and geochemical variations in the martian basalts: Implications for martian basalt petrogenesis and the oxidation state of the upper mantle of Mars. Geochimica Et Cosmochimica Acta 66, 2025-2036.

Hirschmann, M.M. and Withers, A.C. (2008) Ventilation of CO_2 from a reduced mantle and consequences for the early martian greenhouse. Earth and Planetary Science Letters 270, 147-155.

Hofmann, A.W. (1988) Chemical differentiation of the Earth: The relationship between mantle, continental crust, and oceanic crust. Earth and Planetary Science Letters 90, 297-314.

Howard, H.T., Tyler, G.L., Esposito, P.B., Anderson, J.D., Reasenberg, R.D., Shapiro, I.I., Fjeldbo, G., Kliore, A.J., Levy, G.S., Brunn, D.L., Dickinson, R., Edelson, R.E., Martin, W.L., Postal, R.B., Seidel, B., Sesplaukis,

T.T., Shirley, D.L., Stelzried, C.T., Sweetnam, D.N., Wood, G.E. and Zygielbaum, A.I. (1974) Mercury: Results on Mass, Radius, Ionosphere, and Atmosphere from Mariner 10 Dual-Frequency Radio Signals. Science 185, 179-180.

Iacovino, K., McCubbin, F.M., Vander Kaaden, K.E., Clark, J., Wittmann, A., Jakubek, R.S., Moore, G.M., Fries, M.D., Archer, D. and Boyce, J.W. (2023) Carbon as a key driver of super-reduced explosive volcanism on Mercury: Evidence from graphite-melt smelting experiments. Earth and Planetary Science Letters 602, 117908.

Izenberg, N.R., Klima, R.L., Murchie, S.L., Blewett, D.T., Holsclaw, G.M., McClintock, W.E., Malaret, E., Mauceri, C., Vilas, F., Sprague, A.L., Helbert, J., Domingue, D.L., Head, J.W., Goudge, T.A., Solomon, S.C., Hibbitts, C.A. and Dyar, M.D. (2014) The low-iron, reduced surface of Mercury as seen in spectral reflectance by MESSENGER. Icarus 228, 364-374.

Jackson, C.R.M., Bennett, N.R., Du, Z., Cottrell, E., and Fei, Y. (2018) Early episodes of high-pressure core formation preserved in plume mantle. Nature, 553, 491-495.

Jagoutz, E., Palme, H., Baddenhausen, H., Blum, K., Cendales, M., Dreibus, G., Spettel, B., Lorenz, V. and Wänke, H. (1979) The abundances of major, minor, and trace elements in the Earth's mantle as derived from primitive ultramafic nodules. Proceedings of the 10th Lunar and Planetary Science Conference, 2031-2050.

Javoy, M., Kaminski, E., Guyot, F., Andrault, D., Sanloup, C., Moreira, M., Labrosse, S., Jambon, A., Agrinier, P., Davaille, A. and Jaupart, C. (2010) The chemical composition of the Earth: Enstatite chondrite models. Earth and Planetary Science Letters 293, 259-268.

Jochum, K.P., Hofmann, A.W., Ito, E., Seufert, H.M. and White, W.M. (1983) K, U AND Th in mid-ocean ridge basalt glasses and heat-production, K/U, and K/Rb in the mantle. Nature 306, 431-436.

Jolliff, B.L., Gillis, J.J., Haskin, L.A., Korotev, R.L. and Wieczorek, M.A. (2000) Major lunar crustal terranes: Surface expressions and crust-mantle origins. Journal of Geophysical Research-Planets 105, 4197-4216.

Karner, J.M., Papike, J.J., Shearer, C.K., McKay, G., Le, L. and Burger, P. (2007) Valence state partitioning of Cr and V between pyroxene-melt: Estimates of oxygen fugacity for martian basalt QUE 94201. American Mineralogist 92, 1238-1241.

Karner, J.M., Papike, J.J., Sutton, S.R., Burger, P.V., Shearer, C.K., Le, L., Newville, M. and Choi, Y. (2010) Partitioning of Eu between augite and a highly spiked martian basalt composition as a function of oxygen fugacity (IW-1 to QFM): Determination of Eu2+/Eu3+ ratios by XANES. American Mineralogist 95, 410-413.

Keil, K. (2010) Enstatite achondrite meteorites (aubrites) and the histories of their asteroidal parent bodies. Chemie Der Erde-Geochemistry 70, 295-317.

Keil, K. and Brett, R. (1974) Heideite, $(Fe, Cr)_1(Ti,Fe)_2S_4$, a new mineral in the Bustee enstatite achondrite. American Mineralogist 59, 465-470.

Keil, K., McCoy, T.J., Wilson, L., Barrat, J.-A., Rumble, D., Meier, M.M.M., Wieler, R. and Huss, G.R. (2011) A composite Fe, Ni-FeS and enstatite-forsterite-diopside-glass vitrophyre clast in the Larkman Nunatak 04316 aubrite: Origin by pyroclastic volcanism. Meteoritics & Planetary Science 46, 1719-1741.

Kelemen, P.B. and Manning, C.E. (2015) Reevaluating carbon fluxes in subduction zones, what goes down, mostly comes up. Proceedings of the National Academy of Sciences 112, E3997-E4006.

Kelley, K.A. and Cottrell, E. (2009) Water and the oxidation state of subduction zone magmas. Science 325, 605-607.

Killen, R., Cremonese, G., Lammer, H., Orsini, S., Potter, A.E., Sprague, A.L., Wurz, P., Khodachenko, M.L., Lichtenegger, H.I.M., Milillo, A. and Mura, A. (2007) Processes that Promote and Deplete the Exosphere of Mercury. Space Science Reviews 132, 433-509.

Killen, R.M. and Hahn, J.M. (2015) Impact vaporization as a possible source of Mercury's calcium exosphere. Icarus 250, 230-237.

Kim, D.-H., Paek, M.-K., Kim, T.-J., Won, S.-Y. and Pak, J.-J. (2014) Carbon Solubility in Liquid Iron Containing V, Mo and Ni. MATERIALS TRANSACTIONS 55, 610-615.

Klima, R.L., Denevi, B.W., Ernst, C.M., Murchie, S.L. and Peplowski, P.N. (2018) Global Distribution and Spectral Properties of Low-Reflectance Material on Mercury. Geophysical Research Letters 45, 2945-2953.

Knibbe, J.S., Rivoldini, A., Luginbuhl, S.M., Namur, O., Charlier, B., Mezouar, M., Sifre, D., Berndt, J., Kono, Y., Neuville, D.R., van Westrenen, W. and Van Hoolst, T. (2021) Mercury's Interior Structure Constrained by Density and P-Wave Velocity Measurements of Liquid Fe-Si-C Alloys. Journal of Geophysical Research: Planets 126, e2020JE006651.

Knibbe, J.S. and van Westrenen, W. (2018) The thermal evolution of Mercury's Fe–Si core. Earth and Planetary Science Letters 482, 147-159.

Kress, V.C. and Carmichael, I.S.E. (1991) The compressibility of silicate liquids containing Fe_2O_3 and the effect of composition, temperature, oxygen fugacity and pressure on their redox states. Contributions to Mineralogy and Petrology 108, 82-92.

Lam, K.W.F., Csizmadia, S., Astudillo-Defru, N., Bonfils, X., Gandolfi, D., Padovan, S., Esposito, M., Hellier, C., Hirano, T., Livingston, J., Murgas, F., Smith, A.M.S., Collins, K.A., Mathur, S., Garcia, R.A., Howell, S.B., Santos, N.C., Dai, F., Ricker, G.R., Vanderspek, R., Latham, D.W., Seager, S., Winn, J.N., Jenkins, J.M., Albrecht, S., Almenara, J.M., Artigau, E., Barragán, O., Bouchy, F., Cabrera, J., Charbonneau, D., Chaturvedi, P., Chaushev, A., Christiansen, J.L., Cochran, W.D., De Meideiros, J.R., Delfosse, X., Díaz, R.F., Doyon, R., Eigmüller, P., Figueira, P., Forveille, T., Fridlund, M., Gaisné, G., Goffo, E., Georgieva, I., Grziwa, S., Guenther, E., Hatzes, A.P., Johnson, M.C., Kabáth, P., Knudstrup, E., Korth, J., Lewin, P., Lissauer, J.J., Lovis, C., Luque, R., Melo, C., Morgan, E.H., Morris, R., Mayor, M., Narita, N., Osborne, H.L.M., Palle, E., Pepe, F., Persson, C.M., Quinn, S.N., Rauer, H., Redfield, S., Schlieder, J.E., Ségransan, D., Serrano, L.M., Smith, J.C., Šubjak, J., Twicken, J.D., Udry, S., Van Eylen, V. and Vezie, M. (2021) GJ 367b: A dense, ultrashort-period sub-Earth planet transiting a nearby red dwarf star. Science 374, 1271-1275.

Lark, L.H., Parman, S., Huber, C., Parmentier, E.M. and Head III, J.W. (2022) Sulfides in Mercury's Mantle: Implications for Mercury's Interior as Interpreted From Moment of Inertia. Geophysical Research Letters 49, e2021GL096713.

Lark, L.H., Head III, J.W., and Huber, C. (2023) Evidence for a carbon-rich Mercury from the distribution of low-reflectance material (LRM) associated with large impact basins. Earth and Planetary Science Letters 613, 118192.

Lauretta, D.S., Goreva, J.S., Hill, D.H., Killgore, M., La Blue, A.R., Campbell, A., Greenwood, R.C., Verchovsky, A.B. and Franchi, I.A. (2009) The Fountain Hills unique CB chondrite: Insights into thermal processes on the CB parent body. Meteoritics & Planetary Science 44, 823-838.

Lawrence, D.J., Feldman, W.C., Goldsten, J.O., Maurice, S., Peplowski, P.N., Anderson, B.J., Bazell, D., McNutt, R.L., Nittler, L.R., Prettyman, T.H., Rodgers, D.J., Solomon, S.C. and Weider, S.Z. (2013) Evidence for Water Ice Near Mercury's North Pole from MESSENGER Neutron Spectrometer Measurements. Science 339, 292-296.

Lawrence, D.J., Peplowski, P.N., Beck, A.W., Feldman, W.C., Frank, E.A., McCoy, T.J., Nittler, L.R. and Solomon, S.C. (2017) Compositional terranes on Mercury: Information from fast neutrons. Icarus 281, 32-45.

Lee, C.-T. (2018) Geochemical Classification of Elements, in: White, W.M. (Ed.), Encyclopedia of Geochemistry: A Comprehensive Reference Source on the Chemistry of the Earth. Springer International Publishing, Cham, pp. 545-549.

Li, Y., Dasgupta, R. and Tsuno, K. (2017) Carbon contents in reduced basalts at graphite saturation: Implications for the degassing of Mars, Mercury, and the Moon. Journal of Geophysical Research: Planets, In press.

Libourel, G., Marty, B., and Humbert, F. (2003) Nitrogen solubility in basaltic melt. Part I. Effect of oxygen fugacity. Geochimica et Cosmochimica Acta, 67, 4123-4135.

Lock, S.J., Stewart, S.T., Petaev, M.I., Leinhardt, Z., Mace, M.T., Jacobsen, S.B. and Cuk, M. (2018) The Origin of the Moon Within a Terrestrial Synestia. Journal of Geophysical Research-Planets 123, 910-951.

Lodders, K. (1996) An experimental and theoretical study of rare-earth-element partitioning between sulfides (FeS, CaS) and silicate and applications to enstatite achondrites. Meteoritics & Planetary Science 31, 749-766.

Lodders, K. (2003) Solar system abundances and condensation temperatures of the elements. Astrophysical Journal 591, 1220-1247.

Lodders, K. and Fegley, B. (1998) The Planetary Scientist's Companion. Oxford University Press, New York.

Lodders, K., Palme, H. and Wlotzka, F. (1993) Trace elements in mineral seperates of the Pena-Blanca Spring Aubrite: Implications for the evolution of the aubrite parent body. Meteoritics 28, 538-551.

Loeffler, M.J., Dukes, C.A., Chang, W.Y., McFadden, L.A. and Baragiola, R.A. (2008) Laboratory simulations of sulfur depletion at Eros. Icarus 195, 622-629.

Lucey, P., Korotev, R.L., Gillis, J.J., Taylor, L.A., Lawrence, D., Campbell, B.A., Elphic, R., Feldman, B., Hood, L.L., Hunten, D., Mendillo, M., Noble, S., Papike, J.J., Reedy, R.C., Lawson, S., Prettyman, T., Gasnault, O. and Maurice, S. (2006) Understanding the lunar surface and space-moon interactions, New Views of the Moon, pp. 83-220.

Lucey, P.G. and Riner, M.A. (2011) The optical effects of small iron particles that darken but do not redden: Evidence of intense space weathering on Mercury. Icarus 212, 451-462.

Malavergne, V., Berthet, S. and Righter, K. (2007a) Formation of CaS-MgS in enstatite chondrites and achondrites as a function of redox conditions and temperature: constraints on their evolution in a planetesimal and in a proto-

planet, 38th Lunar and Planetary Science Conference. Lunar and Planetary Institute, Houston, TX, p. Abstract #1737.
Malavergne, V., Cordier, P., Righter, K., Brunet, F., Zanda, B., Addad, A., Smith, T., Bureau, H., Surble, S., Raepsaet, C., Charon, E. and Hewins, R.H. (2014) How Mercury can be the most reduced terrestrial planet and still store iron in its mantle. Earth and Planetary Science Letters 394, 186-197.
Malavergne, V., Tarrida, M., Combes, R., Bureau, H., Jones, J. and Schwandt, C. (2007b) New high-pressure and high-temperature metal/silicate partitioning of U and Pb: Implications for the cores of the Earth and Mars. Geochimica Et Cosmochimica Acta 71, 2637-2655.
Malavergne, V., Toplis, M.J., Berthet, S. and Jones, J. (2010) Highly reducing conditions during core formation on Mercury: Implications for internal structure and the origin of a magnetic field. Icarus 206, 199-209.
Mandler, B.E. and Elkins-Tanton, L.T. (2013) The origin of eucrites, diogenites, and olivine diogenites: Magma ocean crystallization and shallow magma chamber processes on Vesta. Meteoritics & Planetary Science 48, 2333-2349.
Marchi, S., Chapman, C.R., Fassett, C.I., Head, J.W., Bottke, W.F. and Strom, R.G. (2013) Global resurfacing of Mercury 4.0-4.1 billion years ago by heavy bombardment and volcanism. Nature 499, 59-61.
Marchi, S., Mottola, S., Cremonese, G., Massironi, M. and Martellato, E. (2009) A new chronology for the Moon and Mercury. Astronomical Journal 137, 4936-4948.
Margot, J.-L., Hauck II, S.A., Mazarico, E., Padovan, S. and Peale, S.J. (2019) Mercury's Internal Structure, in: Solomon, S.C., Nittler, L.R., Anderson, B.J. (Eds.), Mercury: The View after MESSENGER. Cambridge University Press, pp. 85-113.
Margot, J.L., Peale, S.J., Jurgens, R.F., Slade, M.A. and Holin, I.V. (2007) Large Longitude Libration of Mercury Reveals a Molten Core. Science 316, 710-714.
Marty, B. (2012) The origins and concentrations of water, carbon, nitrogen and noble gases on Earth. Earth and Planetary Science Letters 313, 56-66.
Mathew, K.J. and Marti, K. (2001a) Early evolution of Martian volatiles: Nitrogen and noble gas components in ALH84001 and Chassigny. Journal of Geophysical Research-Planets 106, 1401-1422.
Mathew, K.J. and Marti, K. (2001b) Lunar nitrogen: indigenous signature and cosmic-ray production rate. Earth and Planetary Science Letters 184, 659-669.
Mathew, K.J. and Marti, K. (2002) Martian atmospheric and interior volatiles in the meteorite Nakhla. Earth and Planetary Science Letters 199, 7-20.
Mavrogenes, J.A. and O'Neill, H.S.C. (1999) The relative effects of pressure, temperature and oxygen fugacity on the solubility of sulfide in mafic magmas. Geochimica Et Cosmochimica Acta 63, 1173-1180.
McClintock, W.E., Izenberg, N.R., Holsclaw, G.M., Blewett, D.T., Domingue, D.L., Head, J.W., III, Helbert, J., McCoy, T.J., Murchie, S.L., Robinson, M.S., Solomon, S.C., Sprague, A.L. and Vilas, F. (2008) Spectroscopic observations of Mercury's surface reflectance during MESSENGER's first mercury flyby. Science 321, 62-65.
McClintock, W.E., Vervack, R.J., Bradley, E.T., Killen, R.M., Mouawad, N., Sprague, A.L., Burger, M.H., Solomon, S.C. and Izenberg, N.R. (2009) MESSENGER Observations of Mercury's Exosphere: Detection of Magnesium and Distribution of Constituents. Science 324, 610-613.
McCord, T.B. and Adams, J.B. (1972) Mercury: Surface Composition from the Reflection Spectrum. Science 178, 745-747.
McCord, T.B. and Clark, R.N. (1979) Mercury soil: Presence of Fe^{2+}. Journal of Geophysical Research 84, 7664-7668.
McCord, T.B., Taylor, L.A., Combe, J.P., Kramer, G., Pieters, C.M., Sunshine, J.M. and Clark, R.N. (2011) Sources and physical processes responsible for OH/H2O in the lunar soil as revealed by the Moon Mineralogy Mapper (M-3). Journal of Geophysical Research-Planets 116.
McCoy, T.J. (1998) A pyroxene-oldhamite clast in Bustee: Igneous aubritic oldhamite and a mechanism for the Ti-enrichment in aubritic troilite. Antarctic Meteorite Research 11, 34-50.
McCoy, T.J., Dickinson, T.L. and Lofgren, G.E. (1999) Partial melting of the Indarch (EH4) meteorite: A textural, chemical, and phase relations view of melting and melt migration. Meteoritics & Planetary Science 34, 735-746.
McCoy, T.J. and Nittler, L.R. (2014) Mercury, in: Holland, H.D., Turekian, K.K. (Eds.), Treatise on Geochemistry (Second Edition). Elsevier, Oxford, pp. 119-126.
McCoy, T.J., Peplowski, P.N., McCubbin, F.M. and Weider, S.Z. (2018) The geochemical and mineralogical diversity of Mercury, in: Solomon, S.C., Nittler, L.R., Anderson, B.J. (Eds.), Mercury: The View after MESSENGER. Cambridge University Press, Cambridge, United Kingdom, pp. 176-190.

McCoy, T.J., Corrigan, C.M., Dickinson, T.L., Benedix, G.K., Schrader, D.L., and Davidson, J. (2019) Grove Mountains (GRV) 020043: Insights into acapulcoite-lodranite genesis from the most primitive member. Geochemistry, 79, 125536, https://doi.org/10.1016/j.chemer.2019.125536

McCubbin, F.M. and Barnes, J.J. (2019) Origin and abundances of H_2O in the terrestrial planets, Moon, and asteroids. Earth and Planetary Science Letters 526, 115771.

McCubbin, F.M. and Jones, R.H. (2015) Extraterrestrial Apatite: Planetary Geochemistry to Astrobiology. Elements 11, 183-188.

McCubbin, F.M., Kaaden, K.E.V., Tartèse, R., Klima, R.L., Liu, Y., Mortimer, J., Barnes, J.J., Shearer, C.K., Treiman, A.H., Lawrence, D.J., Elardo, S.M., Hurley, D.M., Boyce, J.W. and Anand, M. (2015) Magmatic volatiles (H, C, N, F, S, Cl) in the lunar mantle, crust, and regolith: Abundances, distributions, processes, and reservoirs. American Mineralogist 100, 1668-1707.

McCubbin, F.M., Riner, M.A., Vander Kaaden, K.E. and Burkemper, L.K. (2012) Is Mercury a volatile-rich planet? Geophysical Research Letters 39.

McCubbin, F.M., Vander Kaaden, K.E., Peplowski, P.N., Bell, A.S., Nittler, L.R., Boyce, J.W., Evans, L.G., Keller, L.P., Elardo, S.M. and McCoy, T.J. (2017) A Low O/Si Ratio on the Surface of Mercury: Evidence for Silicon Smelting? Journal of Geophysical Research: Planets 122, 2053-2076.

McDonough, W.F. (2003) Compositional Model for the Earth's core, in: Holland, H.D., Turekian, K.K. (Eds.), Treatise on Geochemistry Volume 2: The Mantle and Core. Elsevier, pp. 547-568.

McDonough, W.F. and Sun, S.S. (1995) The composition of the Earth. Chemical Geology 120, 223-253.

McLennan, S.M. (2003) Large-ion lithophile element fractionation during the early differentiation of Mars and the composition of the martian primitive mantle. Meteoritics & Planetary Science 38, 895-904.

Merkel, A.W., Cassidy, T.A., Vervack, R.J., McClintock, W.E., Sarantos, M., Burger, M.H. and Killen, R.M. (2017) Seasonal variations of Mercury's magnesium dayside exosphere from MESSENGER observations. Icarus 281, 46-54.

Merkel, A.W., Vervack Jr., R.J., Killen, R.M., Cassidy, T.A., McClintock, W.E., Nittler, L.R. and Burger, M.H. (2018) Evidence Connecting Mercury's Magnesium Exosphere to Its Magnesium-Rich Surface Terrane. Geophysical Research Letters 45, 6790-6797.

Mikhail, S. and Sverjensky, D.A. (2014) Nitrogen speciation in upper mantle fluids and the origin of Earth's nitrogen-rich atmosphere. Nature Geoscience 7, 816-819.

Mittlefehldt, D.W., McCoy, T.J., Goodrich, C.A. and Kracher, A. (1998) Non-chondritic meteorites from asteroidal bodies. Planetary Materials 36, D1-D195.

Mojzsis, S.J., Abramov, O., Frank, E.A. and Brasser, R. (2018) Thermal effects of late accretion to the crust and mantle of Mercury. Earth and Planetary Science Letters 482, 536-544.

Moore, J.M., Asphaug, E., Morrison, D., Spencer, J.R., Chapman, C.R., Bierhaus, B., Sullivan, R.J., Chuang, F.C., Klemaszewski, J.E., Greeley, R., Bender, K.C., Geissler, P.E., Helfenstein, P. and Pilcher, C.B. (1999) Mass Movement and Landform Degradation on the Icy Galilean Satellites: Results of the Galileo Nominal Mission. Icarus 140, 294-312.

Moore, J.M., Howard, A.D., Umurhan, O.M., White, O.L., Schenk, P.M., Beyer, R.A., McKinnon, W.B., Spencer, J.R., Grundy, W.M., Lauer, T.R., Nimmo, F., Young, L.A., Stern, S.A., Weaver, H.A., Olkin, C.B. and Ennico, K. (2017) Sublimation as a landform-shaping process on Pluto. Icarus 287, 320-333.

Moore, J.M., Mellon, M.T. and Zent, A.P. (1996) Mass Wasting and Ground Collapse in Terrains of Volatile-Rich Deposits as a Solar System-Wide Geological Process: The Pre-Galileo View. Icarus 122, 63-78.

Morgan, J.W. and Anders, E. (1980) Chemical composition of Earth, Venus, and Mercury. Proceedings of the National Academy of Sciences of the United States of America 77, 6973-6977.

Mortimer, J., Verchovsky, A.B. and Anand, M. (2016) Predominantly non-solar origin of nitrogen in lunar soils. Geochimica Et Cosmochimica Acta 193, 36-53.

Mouser, M.D., Dygert, N., Anzures, B.A., Grambling, N.L., Hrubiak, R., Kono, Y., Shen, G. and Parman, S.W. (2021) Experimental Investigation of Mercury's Magma Ocean Viscosity: Implications for the Formation of Mercury's Cumulate Mantle, Its Subsequent Dynamic Evolution, and Crustal Petrogenesis. Journal of Geophysical Research: Planets 126, e2021JE006946.

Murchie, S.L., Klima, R.L., Denevi, B.W., Ernst, C.M., Keller, M.R., Domingue, D.L., Blewett, D.T., Chabot, N.L., Hash, C.D., Malaret, E., Izenberg, N.R., Vilas, F., Nittler, L.R., Gillis-Davis, J.J., Head, J.W. and Solomon, S.C. (2015) Orbital multispectral mapping of Mercury with the MESSENGER Mercury Dual Imaging System: Evidence for the origins of plains units and low-reflectance material. Icarus 254, 287-305.

Murray, B.C., Belton, M.J.S., Danielson, G.E., Davies, M.E., Gault, D.E., Hapke, B., O'Leary, B., Strom, R.G., Suomi, V. and Trask, N. (1974) Mercury's Surface: Preliminary Description and Interpretation from Mariner 10 Pictures. Science 185, 169-179.

Mysen, B. (2019) Nitrogen in the Earth: abundance and transport. Progress in Earth and Planetary Science 6, 38.

Nakamura-Messenger, K., Clemett, S.J., Rubin, A.E., Choi, B.-G., Zhang, S., Rahman, Z., Oikawa, K. and Keller, L.P. (2012) Wassonite: A new titanium monosulfide mineral in the Yamato 691 enstatite chondrite. American Mineralogist, 97, 807-815.

Namur, O. and Charlier, B. (2017) Silicate mineralogy at the surface of Mercury. Nature Geosci 10, 9-13.

Namur, O., Charlier, B., Holtz, F., Cartier, C. and McCammon, C. (2016a) Sulfur solubility in reduced mafic silicate melts: Implications for the speciation and distribution of sulfur on Mercury. Earth and Planetary Science Letters 448, 102-114.

Namur, O., Collinet, M., Charlier, B., Grove, T.L., Holtz, F. and McCammon, C. (2016b) Melting processes and mantle sources of lavas on Mercury. Earth and Planetary Science Letters 439, 117-128.

Nathues, A., Hoffmann, M., Schaefer, M., Le Corre, L., Reddy, V., Platz, T., Cloutis, E.A., Christensen, U., Kneissl, T., Li, J.Y., Mengel, K., Schmedemann, N., Schaefer, T., Russell, C.T., Applin, D.M., Buczkowski, D.L., Izawa, M.R.M., Keller, H.U., O'Brien, D.P., Pieters, C.M., Raymond, C.A., Ripken, J., Schenk, P.M., Schmidt, B.E., Sierks, H., Sykes, M.V., Thangjam, G.S. and Vincent, J.B. (2015) Sublimation in bright spots on (1) Ceres. Nature 528, 237-240.

Ness, N.F., Behannon, K.W., Lepping, R.P., Whang, Y.C. and Schatten, K.H. (1974) Magnetic Field Observations near Mercury: Preliminary Results from Mariner 10. Science 185, 151-160.

Neumann, G.A., Cavanaugh, J.F., Sun, X., Mazarico, E.M., Smith, D.E., Zuber, M.T., Mao, D., Paige, D.A., Solomon, S.C., Ernst, C.M. and Barnouin, O.S. (2013) Bright and Dark Polar Deposits on Mercury: Evidence for Surface Volatiles. Science 339, 296-300.

Nittler, L.R., Boujibar, A., Crapster-Pregont, E., Frank, E.A., McCoy, T.J., McCubbin, F.M., Starr, R.D., Vorburger, A. and Weider, S.Z. (2023) Chromium on Mercury: New results from the MESSENGER X-Ray Spectrometer and implications for the innermost planet's geochemical evolution. Journal of Geophysical Research: Planets In Press.

Nittler, L.R., Chabot, N.L., Grove, T.L. and Peplowski, P.N. (2018) The Chemical Composition of Mercury, in: Solomon, S.C., Nittler, L.R., Anderson, B.J. (Eds.), Mercury: The View after MESSENGER. Cambridge University Press, pp. 30-51.

Nittler, L.R., Frank, E.A., Weider, S.Z., Crapster-Pregont, E., Vorburger, A., Starr, R.D. and Solomon, S.C. (2020) Global major-element maps of Mercury from four years of MESSENGER X-Ray Spectrometer observations. Icarus 345, 113716.

Nittler, L.R., Starr, R.D., Weider, S.Z., McCoy, T.J., Boynton, W.V., Ebel, D.S., Ernst, C.M., Evans, L.G., Goldsten, J.O., Hamara, D.K., Lawrence, D.J., McNutt, R.L., Schlemm, C.E., Solomon, S.C. and Sprague, A.L. (2011) The Major-Element Composition of Mercury's Surface from MESSENGER X-ray Spectrometry. Science 333, 1847-1850.

O'Neill, H.S.C. and Eggins, S.M. (2002) The effect of melt composition on trace element partitioning: an experimental investigation of the activity coefficients of FeO, NiO, CoO, MoO_2 and MoO_3 in silicate melts. Chemical Geology 186, 151-181.

O'Neill, H.S.C., Berry, A.J., and Mallmann, G. (2018) The oxidation state of iron in Mid-Ocean Ridge Basaltic (MORB) glasses: Implications for their petrogenesis and oxygen fugacities. Earth and Planetary Science Letters, 504, 152-162.

Okada, A. and Keil, K. (1982) Caswellsilverite, $NaCrS_2$: A new mineral in the Norton County enstatite achondrite. American Mineralogist 67, 132-136.

Ostrach, L.R., Robinson, M.S., Whitten, J.L., Fassett, C.I., Strom, R.G., Head, J.W. and Solomon, S.C. (2015) Extent, age, and resurfacing history of the northern smooth plains on Mercury from MESSENGER observations. Icarus 250, 602-622.

Paige, D.A., Siegler, M.A., Harmon, J.K., Neumann, G.A., Mazarico, E.M., Smith, D.E., Zuber, M.T., Harju, E., Delitsky, M.L. and Solomon, S.C. (2013) Thermal Stability of Volatiles in the North Polar Region of Mercury. Science 339, 300-303.

Palme, H., Lodders, K. and Jones, A. (2014) Solar System Abundances of the Elements, in: Davis, A.M. (Ed.), Planets, Asteriods, Comets and The Solar System, pp. 15-36.

Palme, H. and Nickel, K.G. (1985) CaAl ratio and composition of the Earth's upper mantle. Geochimica et Cosmochimica Acta 49, 2123-2132.

Papike, J.J., Karner, J.M. and Shearer, C.K. (2004) Comparative planetary mineralogy: V/(Cr+Al) systematics in chromite as an indicator of relative oxygen fugacity. American Mineralogist 89, 1557-1560.

Papike, J.J., Karner, J.M. and Shearer, C.K. (2005) Comparative planetary mineralogy: Valence state partitioning of Cr, Fe, Ti, and V among crystallographic sites in olivine, pyroxene, and spinel from planetary basalts. American Mineralogist 90, 277-290.

Papike, J.J., Simon, S.B., Burger, P.V., Bell, A.S., Shearer, C.K. and Karner, J.M. (2016) Chromium, vanadium, and titanium valence systematics in Solar System pyroxene as a recorder of oxygen fugacity, planetary provenance, and processes. American Mineralogist 101, 907-918.

Pasek, M.A. (2015) Phosphorus as a lunar volatile. Icarus 255, 18-23.

Pasek, M.A. (2019) Phosphorus volatility in the early solar nebula. Icarus 317, 59-65.

Peplowski, P.N. (2016) The global elemental composition of 433 Eros: First results from the NEAR gamma-ray spectrometer orbital dataset. Planetary and Space Science 134, 36-51.

Peplowski, P.N., Evans, L.G., Hauck, S.A., McCoy, T.J., Boynton, W.V., Gillis-Davis, J.J., Ebel, D.S., Goldsten, J.O., Hamara, D.K., Lawrence, D.J., McNutt, R.L., Nittler, L.R., Solomon, S.C., Rhodes, E.A., Sprague, A.L., Starr, R.D. and Stockstill-Cahill, K.R. (2011) Radioactive Elements on Mercury's Surface from MESSENGER: Implications for the Planet's Formation and Evolution. Science 333, 1850-1852.

Peplowski, P.N., Evans, L.G., Stockstill-Cahill, K.R., Lawrence, D.J., Goldsten, J.O., McCoy, T.J., Nittler, L.R., Solomon, S.C., Sprague, A.L., Starr, R.D. and Weider, S.Z. (2014) Enhanced sodium abundance in Mercury's north polar region revealed by the MESSENGER Gamma-Ray Spectrometer. Icarus 228, 86-95.

Peplowski, P.N., Klima, R.L., Lawrence, D.J., Ernst, C.M., Denevi, B.W., Frank, E.A., Goldsten, J.O., Murchie, S.L., Nittler, L.R. and Solomon, S.C. (2016) Remote sensing evidence for an ancient carbon-bearing crust on Mercury. Nature Geoscience 9, 273-276.

Peplowski, P.N., Lawrence, D.J., Evans, L.G., Klima, R.L., Blewett, D.T., Goldsten, J.O., Murchie, S.L., McCoy, T.J., Nittler, L.R., Solomon, S.C., Starr, R.D. and Weider, S.Z. (2015a) Constraints on the abundance of carbon in near-surface materials on Mercury: Results from the MESSENGER Gamma-Ray Spectrometer. Planetary and Space Science 108, 98-107.

Peplowski, P.N., Lawrence, D.J., Feldman, W.C., Goldsten, J.O., Bazell, D., Evans, L.G., Head, J.W., Nittler, L.R., Solomon, S.C. and Weider, S.Z. (2015b) Geochemical terranes of Mercury's northern hemisphere as revealed by MESSENGER neutron measurements. Icarus 253, 346-363.

Peplowski, P.N., Lawrence, D.J., Rhodes, E.A., Sprague, A.L., McCoy, T.J., Denevi, B.W., Evans, L.G., Head, J.W., Nittler, L.R., Solomon, S.C., Stockstill-Cahill, K.R. and Weider, S.Z. (2012) Variations in the abundances of potassium and thorium on the surface of Mercury: Results from the MESSENGER Gamma-Ray Spectrometer. Journal of Geophysical Research – Planets 117.

Peplowski, P.N. and Stockstill-Cahill, K. (2019) Analytical Identification and Characterization of the Major Geochemical Terranes of Mercury's Northern Hemisphere. Journal of Geophysical Research: Planets 124, 2414-2429.

Petaev, M.I., Wood, J.A., Meibom, A., Krot, A.N. and Keil, K. (2003) The ZONMET thermodynamic and kinetic model of metal condensation. Geochimica et Cosmochimica Acta 67, 1737-1751.

Phillips, M.S., Moersch, J.E., Viviano, C.E. and Emery, J.P. (2021) The lifecycle of hollows on Mercury: An evaluation of candidate volatile phases and a novel model of formation. Icarus 359, 114306.

Pirotte, H., C. Cartier, O. Namur, A. Pommier, Y. Zhang, J. Berndt, S. Klemme, B. Charlier, Internal differentiation and volatile budget of Mercury inferred from the partitioning of heat-producing elements at highly reduced conditions, Icarus, https://doi.org/10.1016/j.icarus.2023.115699

Pommier, A., M.J. Tauber, H. Pirotte, G. Cody, A. Steele, E.S. Bullock, B. Charlier, and B.O. Mysen (2023) Experimental Investigation of the Bonding of Sulfur in Highly Reduced Silicate Glasses and Melts, Geochimica et Cosmochimica Acta, 363, 114-128.

Potter, A.E., Killen, R.M. and Morgan, T.H. (2002) The sodium tail of Mercury. Meteoritics & Planetary Science 37, 1165-1172.

Potter, A.E., Killen, R.M. and Sarantos, M. (2006) Spatial distribution of sodium on Mercury. Icarus 181, 1-12.

Prettyman, T.H., Hagerty, J.J., Elphic, R.C., Feldman, W.C., Lawrence, D.J., McKinney, G.W. and Vaniman, D.T. (2006) Elemental composition of the lunar surface: Analysis of gamma ray spectroscopy data from Lunar Prospector. Journal of Geophysical Research-Planets 111.

Prettyman, T.H., Yamashita, N., Reedy, R.C., McSween, H.Y., Jr., Mittlefehldt, D.W., Hendricks, J.S. and Toplis, M.J. (2015) Concentrations of potassium and thorium within Vesta's regolith. Icarus 259, 39-52.

Procketr, L.M., and Bedini, P.D. (2010) The Study of Mercury. Proceedings of IAU Symposium No. 269, 141-154.

Renggli, C.J., Klemme, S., Morlok, A., Berndt, J., Weber, I., Hiesinger, H. and King, P.L. (2022) Sulfides and hollows formed on Mercury's surface by reactions with reducing S-rich gases. Earth and Planetary Science Letters 593, 117647.

Righter, K. and Drake, M.J. (1996) Core formation in Earth's Moon, Mars, and Vesta. Icarus 124, 513-529.

Righter, K. and Drake, M.J. (1997) A magma ocean on Vesta: Core formation and petrogenesis of eucrites and diogenites. Meteoritics & Planetary Science 32, 929-944.

Righter, K., Drake, M.J. and Scott, E. (2006) Compositional relationships between meteorites and terrestrial planets, Meteorites and the Early Solar System II. University of Arizona Press, Tucson, AZ, pp. 803-828.

Righter, K., Sutton, S.R., Danielson, L., Pando, K., and Newville, M. (2016) Redox variations in the inner solar system with new constraints from vanadium XANES in spinels. American Mineralogist, 101, 1928–1942.

Righter, K., Pando, K., Ross, D.K., Righter, M. and Lapen, T.J. (2019) Effect of silicon on activity coefficients of Bi, Cd, Sn, and Ag in liquid Fe-Si, and implications for differentiation and core formation. Meteoritics & Planetary Science 54, 1379-1394.

Riner, M.A., Bina, C.R., Robinson, M.S. and Desch, S.J. (2008) Internal structure of Mercury: Implications of a molten core. Journal of Geophysical Research-Planets 113.

Riner, M.A., Lucey, P.G., Desch, S.J. and McCubbin, F.M. (2009) Nature of opaque components on Mercury: Insights into a Mercurian magma ocean. Geophysical Research Letters 36.

Riner, M.A., McCubbin, F.M., Lucey, P.G., Talyor, G.J. and Gillis-Davis, J.J. (2010) Mercury surface composition: Integrating petrologic modeling and remote sensing data to place constraints on FeO abundance. Icarus 209, 301-313.

Ringwood, A.E. (1979) Origin of the Earth and Moon. Springer, New York, NY.

Rivera-Valentín, E.G., Meyer, H.M., Taylor, P.A., Mazarico, E., Bhiravarasu, S.S., Virkki, A.K., Nolan, M.C., Chabot, N.L. and Giorgini, J.D. (2022) Arecibo S-band Radar Characterization of Local-scale Heterogeneities within Mercury's North Polar Deposits. The Planetary Science Journal 3, 62.

Robinson, M.S. and Lucey, P.G. (1997) Recalibrated Mariner 10 color mosaics: Implications for Mercurian volcanism. Science 275, 197-200.

Robinson, M.S., Murchie, S.L., Blewett, D.T., Domingue, D.L., Hawkins, S.E., III, Head, J.W., Holsclaw, G.M., McClintock, W.E., McCoy, T.J., McNutt, R.L., Jr., Prockter, L.M., Solomon, S.C. and Watters, T.R. (2008) Reflectance and color variations on Mercury: Regolith processes and compositional heterogeneity. Science 321, 66-69.

Robinson, M.S. and Taylor, G.J. (2001) Ferrous oxide in Mercury's crust and mantle. Meteoritics & Planetary Science 36, 841-847.

Rose-Weston, L., Brenan, J.M., Fei, Y.W., Secco, R.A. and Frost, D.J. (2009) Effect of pressure, temperature, and oxygen fugacity on the metal-silicate partitioning of Te, Se, and S: Implications for earth differentiation. Geochimica Et Cosmochimica Acta 73, 4598-4615.

Rothery, D.A., Massironi, M., Alemanno, G., Barraud, O., Besse, S., Bott, N., Brunetto, R., Bunce, E., Byrne, P., Capaccioni, F., Capria, M.T., Carli, C., Charlier, B., Cornet, T., Cremonese, G., D'Amore, M., De Sanctis, M.C., Doressoundiram, A., Ferranti, L., Filacchione, G., Galluzzi, V., Giacomini, L., Grande, M., Guzzetta, L.G., Helbert, J., Heyner, D., Hiesinger, H., Hussmann, H., Hyodo, R., Kohout, T., Kozyrev, A., Litvak, M., Lucchetti, A., Malakhov, A., Malliband, C., Mancinelli, P., Martikainen, J., Martindale, A., Maturilli, A., Milillo, A., Mitrofanov, I., Mokrousov, M., Morlok, A., Muinonen, K., Namur, O., Owens, A., Nittler, L.R., Oliveira, J.S., Palumbo, P., Pajola, M., Pegg, D.L., Penttilä, A., Politi, R., Quarati, F., Re, C., Sanin, A., Schulz, R., Stangarone, C., Stojic, A., Tretiyakov, V., Väisänen, T., Varatharajan, I., Weber, I., Wright, J., Wurz, P. and Zambon, F. (2020) Rationale for BepiColombo Studies of Mercury's Surface and Composition. Space Science Reviews 216, 66.

Russell, C.T., Raymond, C.A., Ammannito, E., Buczkowski, D.L., De Sanctis, M.C., Hiesinger, H., Jaumann, R., Konopliv, A.S., McSween, H.Y., Nathues, A., Park, R.S., Pieters, C.M., Prettyman, T.H., McCord, T.B., McFadden, L.A., Mottola, S., Zuber, M.T., Joy, S.P., Polanskey, C., Rayman, M.D., Castillo-Rogez, J.C., Chi, P.J., Combe, J.P., Ermakov, A., Fu, R.R., Hoffmann, M., Jia, Y.D., King, S.D., Lawrence, D.J., Li, J.-Y., Marchi, S., Preusker, F., Roatsch, T., Ruesch, O., Schenk, P., Villarreal, M.N. and Yamashita, N. (2016) Dawn arrives at Ceres: Exploration of a small, volatile-rich world. Science 353, 1008-1010.

Russell, C.T., Raymond, C.A., Coradini, A., McSween, H.Y., Zuber, M.T., Nathues, A., De Sanctis, M.C., Jaumann, R., Konopliv, A.S., Preusker, F., Asmar, S.W., Park, R.S., Gaskell, R., Keller, H.U., Mottola, S., Roatsch, T., Scully, J.E.C., Smith, D.E., Tricarico, P., Toplis, M.J., Christensen, U.R., Feldman, W.C., Lawrence, D.J., McCoy, T.J., Prettyman, T.H., Reedy, R.C., Sykes, M.E. and Titus, T.N. (2012) Dawn at Vesta: Testing the Protoplanetary Paradigm. Science 336, 684-686.

Santerne, A., Brugger, B., Armstrong, D.J., Adibekyan, V., Lillo-Box, J., Gosselin, H., Aguichine, A., Almenara, J.M., Barrado, D., Barros, S.C.C., Bayliss, D., Boisse, I., Bonomo, A.S., Bouchy, F., Brown, D.J.A., Deleuil, M., Delgado Mena, E., Demangeon, O., Díaz, R.F., Doyle, A., Dumusque, X., Faedi, F., Faria, J.P., Figueira, P., Foxell, E., Giles, H., Hébrard, G., Hojjatpanah, S., Hobson, M., Jackman, J., King, G., Kirk, J., Lam, K.W.F., Ligi, R., Lovis, C., Louden, T., McCormac, J., Mousis, O., Neal, J.J., Osborn, H.P., Pepe, F., Pollacco, D., Santos, N.C., Sousa, S.G., Udry, S. and Vigan, A. (2018) An Earth-sized exoplanet with a Mercury-like composition. Nature Astronomy 2, 393-400.

Sarafian, A.R., Nielsen, S.G., Marschall, H.R., McCubbin, F.M. and Monteleone, B.D. (2014) Early accretion of water in the inner solar system from a carbonaceous chondrite-like source. Science 346, 623-626.

Sasaki, S. and Kurahashi, E. (2004) Space weathering on Mercury. Advances in Space Research 33, 2152-2155.

Sasaki, S., Nakamura, K., Hamabe, Y., Kurahashi, E. and Hiroi, T. (2001) Production of iron nanoparticles by laser irradiation in a simulation of lunar-like space weathering. Nature 410, 555-557.

Saxena, S.K. and Fei, Y. (1987) High pressure and high temperature fluid fugacities. Geochimica Et Cosmochimica Acta 51, 783-791.

Schaible, M.J., Sarantos, M., Anzures, B.A., Parman, S.W. and Orlando, T.M. (2020) Photon-Stimulated Desorption of MgS as a Potential Source of Sulfur in Mercury's Exosphere. Journal of Geophysical Research: Planets 125, e2020JE006479.

Scheller, E.L., Razzell Hollis, J., Cardarelli, E.L., Steele, A., Beegle, L.W., Bhartia, R., Conrad, P., Uckert, K., Sharma, S., Ehlmann, B.L., Abbey, W.J., Asher, S.A., Benison, K.C., Berger, E.L., Beyssac, O., Bleefeld, B.L., Bosak, T., Brown, A.J., Burton, A.S., Bykov, S.V., Cloutis, E., Fairén, A.G., DeFlores, L., Farley, K.A., Fey, D.M., Fornaro, T., Fox, A.C., Fries, M., Hickman-Lewis, K., Hug, W.F., Huggett, J.E., Imbeah, S., Jakubek, R.S., Kah, L.C., Kelemen, P., Kennedy, M.R., Kizovski, T., Lee, C., Liu, Y., Mandon, L., McCubbin, F.M., Moore, K.R., Nixon, B.E., Núñez, J.I., Rodriguez Sanchez-Vahamonde, C., Roppel, R.D., Schulte, M., Sephton, M.A., Sharma, S.K., Siljeström, S., Shkolyar, S., Shuster, D.L., Simon, J.I., Smith, R.J., Stack, K.M., Steadman, K., Weiss, B.P., Werynski, A., Williams, A.J., Wiens, R.C., Williford, K.H., Winchell, K., Wogsland, B., Yanchilina, A., Yingling, R. and Zorzano, M.-P. (2022) Aqueous alteration processes in Jezero crater, Mars: Implications for organic geochemistry. Science 378, 1105-1110.

Schrader, D.L., Connolly, H.C., Lauretta, D.S., Nagashima, K., Huss, G.R., Davidson, J., and Domanik, K.J. (2013) The formation and alteration of the Renazzo-like carbonaceous chondrites II: linking O-isotope composition and oxidation state of chondrule olivine. Geochimica et Cosmochimica Acta, 101, 302–327.

Schubert, G., Ross, M.N., Stevenson, D.J. and Spohn, T. (1988) Mercury's thermal history and the generation of its magnetic field, in: Vilas, F. (Ed.), Mercury. University of Arizona Press, Tucson, AZ, pp. 429-460.

Shannon, R. (1976) Revised effective ionic radii and systematic studies of interatomic distances in halides and chalcogenides. Acta Crystallographica Section A 32, 751-767.

Sharp, Z.D. and Draper, D.S. (2013) The chlorine abundance of Earth: Implications for a habitable planet. Earth and Planetary Science Letters 369-370, 71-77.

Shimizu, M., Yoshida, H., and Mandarino, J.A. (2002) The new mineral species keilite, (Fe,Mg)S, the iron-dominant analogue of niningerite. Canadian Mineralogist, 40, 1687-1692.

Siegfried II, R.W., and Solomon, S.C. (1974) Mercury: Internal structure and thermal evolution. Icarus, 23, 192-205.

Skinner, B.J. and Luce, F.D. (1971) Solid Solutions of the Type (Ca,Mg,Mn,Fe)S and their use as Geothermometers for the Enstatite Chondrites. American Mineralogist 56, 1269-1296.

Slade, M.A., Butler, B.J. and Muhleman, D.O. (1992) Mercury Radar Imaging: Evidence for Polar Ice. Science 258, 635-640.

Slavin, J.A., DiBraccio, G.A., Gershman, D.J., Imber, S.M., Poh, G.K., Raines, J.M., Zurbuchen, T.H., Jia, X., Baker, D.N., Glassmeier, K.-H., Livi, S.A., Boardsen, S.A., Cassidy, T.A., Sarantos, M., Sundberg, T., Masters, A., Johnson, C.L., Winslow, R.M., Anderson, B.J., Korth, H., McNutt Jr., R.L. and Solomon, S.C. (2014) MESSENGER observations of Mercury's dayside magnetosphere under extreme solar wind conditions. Journal of Geophysical Research: Space Physics 119, 8087-8116.

Smith, J.V. (1979) Mineralogy of the planets: Voyage in space and time. Mineralogical Magazine 43, 1-89.

Snyder, G.A., Taylor, L.A. and Neal, C.R. (1992) A Chemical-Model for Generating the Sources of Mare Basalts - Combined Equilibrium and Fractional Crystallization of the Lunar Magmasphere. Geochimica Et Cosmochimica Acta 56, 3809-3823.

Solomatov, V. (2007) 9.04 - Magma Oceans and Primordial Mantle Differentiation, in: Schubert, G. (Ed.), Treatise on Geophysics. Elsevier, Amsterdam, pp. 91-119.

Solomatov, V.S. (2000) Fluid dynamics of a terrestrial magma ocean, in: Canup, R.M., Righter, K. (Eds.), Origin of the Earth and Moon. University of Arizona Press, Tucson, AZ, pp. 323-338.

Solomatov, V.S., Olson, P. and Stevenson, D.J. (1993) Entrainment from a bed of particles by thermal convection. Earth and Planetary Science Letters 120, 387-393.
Solomatov, V.S. and Stevenson, D.J. (1993) Nonfractional crystallization of a terrestrial magma ocean. Journal of Geophysical Research: Planets 98, 5391-5406.
Solomon, S.C. (2003) Mercury: the enigmatic innermost planet. Earth and Planetary Science Letters 216, 441-455.
Solomon, S.C. and Byrne, P.K. (2019) The Exploration of Mercury by Spacecraft. Elements 15, 15-20.
Solomon, S.C. and Longhi, J. (1977) Magma oceanography: 1. Thermal evolution, Proceedings of the 8th Lunar Science Conference, Houston, TX, pp. 583-599.
Solomon, S.C., McNutt, R.L., Gold, R.E., Acuna, M.H., Baker, D.N., Boynton, W.V., Chapman, C.R., Cheng, A.F., Gloeckler, G., Head, J.W., Krimigis, S.M., McClintock, W.E., Murchie, S.L., Peale, S.J., Phillips, R.J., Robinson, M.S., Slavin, J.A., Smith, D.E., Strom, R.G., Trombka, J.I. and Zuber, M.T. (2001) The MESSENGER mission to Mercury: scientific objectives and implementation. Planetary and Space Science 49, 1445-1465.
Sprague, A.L., Hanna, K.L.D., Kozlowski, R.W.H., Helbert, J., Maturilli, A., Warell, J.B. and Hora, J.L. (2009) Spectral emissivity measurements of Mercury's surface indicate Mg- and Ca-rich mineralogy, K-spar, Na-rich plagioclase, rutile, with possible perovskite, and garnet. Planetary and Space Science 57, 364-383.
Sprague, A.L., Hunten, D.M. and Lodders, K. (1995) Sulfur at Mercury, elemental at the poles and sulfides in the regolith. Icarus 118, 211-215.
Sprague, A.L., Kozlowski, R.W.H., Witteborn, F.C., Cruikshank, D.P. and Wooden, D.H. (1994) Mercury: Evidence for Anorthosite and Basalt from Mid-infrared (7.3-13.5 μm) Spectroscopy. Icarus 109, 156-167.
Sprague, A.L. and Roush, T.L. (1998) Comparison of Laboratory Emission Spectra with Mercury Telescopic Data. Icarus 133, 174-183.
Stähler, S.C., Khan, A., Banerdt, W.B., Lognonné, P., Giardini, D., Ceylan, S., Drilleau, M., Duran, A.C., Garcia, R.F., Huang, Q., Kim, D., Lekic, V., Samuel, H., Schimmel, M., Schmerr, N., Sollberger, D., Stutzmann, É., Xu, Z., Antonangeli, D., Charalambous, C., Davis, P.M., Irving, J.C.E., Kawamura, T., Knapmeyer, M., Maguire, R., Marusiak, A.G., Panning, M.P., Perrin, C., Plesa, A.-C., Rivoldini, A., Schmelzbach, C., Zenhäusern, G., Beucler, É., Clinton, J., Dahmen, N., van Driel, M., Gudkova, T., Horleston, A., Pike, W.T., Plasman, M. and Smrekar, S.E. (2021) Seismic detection of the martian core. Science 373, 443-448.
Steele, A., Benning, L.G., Wirth, R., Schreiber, A., Araki, T., McCubbin, F.M., Fries, M.D., Nittler, L.R., Wang, J., Hallis, L.J., Conrad, P.G., Conley, C., Vitale, S., O'Brien, A.C., Riggi, V. and Rogers, K. (2022) Organic synthesis associated with serpentinization and carbonation on early Mars. Science 375, 172-177.
Steele, A., McCubbin, F.M. and Fries, M.D. (2016) The provenance, formation, and implications of reduced carbon phases in Martian meteorites. Meteoritics & Planetary Science 51, 2203-2225.
Steenstra, E.S., Berndt, J., Rohrbach, A., Bullock, E.S., van Westrenen, W., Klemme, S. and Walter, M.J. (2022) Partitioning of Ru, Pd, Ag, Re, Pt, Ir and Au between sulfide-, metal- and silicate liquid at highly reduced conditions: Implications for terrestrial accretion and aubrite parent body evolution. Geochimica et Cosmochimica Acta 336, 15-32.
Steenstra, E.S., Dankers, D., Berndt, J., Klemme, S., Matveev, S. and van Westrenen, W. (2019) Significant depletion of volatile elements in the mantle of asteroid Vesta due to core formation. Icarus 317, 669-681.
Steenstra, E.S., Knibbe, J.S., Rai, N. and van Westrenen, W. (2016) Constraints on core formation in Vesta from metal–silicate partitioning of siderophile elements. Geochimica et Cosmochimica Acta 177, 48-61.
Steenstra, E.S., Seegers, A.X., Putter, R., Berndt, J., Klemme, S., Matveev, S., Bullock, E.S. and van Westrenen, W. (2020a) Metal-silicate partitioning systematics of siderophile elements at reducing conditions: A new experimental database. Icarus 335.
Steenstra, E.S., Trautner, V.T., Berndt, J., Klemme, S. and van Westrenen, W. (2020b) Trace element partitioning between sulfide-, metal- and silicate melts at highly reduced conditions: Insights into the distribution of volatile elements during core formation in reduced bodies. Icarus 335.
Steenstra, E.S., van Haaster, F., van Mulligen, R., Flemetakis, S., Berndt, J., Klemme, S. and van Westrenen, W. (2020c) An experimental assessment of the chalcophile behavior of F, Cl, Br and I: Implications for the fate of halogens during planetary accretion and the formation of magmatic ore deposits. Geochimica et Cosmochimica Acta, 273, 275-290.
Steenstra, E.S. and van Westrenen, W. (2020) Geochemical constraints on core-mantle differentiation in Mercury and the aubrite parent body. Icarus 340.
Stockstill-Cahill, K.R., McCoy, T.J., Nittler, L.R., Weider, S.Z. and Hauck, S.A. (2012) Magnesium-rich crustal compositions on Mercury: Implications for magmatism from petrologic modeling. Journal of Geophysical Research-Planets 117, 13.

Takahashi, F., Shimizu, H. and Tsunakawa, H. (2019) Mercury's anomalous magnetic field caused by a symmetry-breaking self-regulating dynamo. Nature Communications 10, 208.
Taylor, G.J. (2013) The bulk composition of Mars. Chemie Der Erde-Geochemistry 73, 401-420.
Taylor, G.J. and Scott, E.R.D. (2003) Mercury, in: Davis, A.M. (Ed.), Treatise on Geochemistry: Meteorites, Comets and Planets. Elsevier, Amsterdam, The Netherlands, pp. 477-485.
Taylor, G.J., Stopar, J.D., Boynton, W.V., Karunatillake, S., Keller, J.M., Bruckner, J., Wänke, H., Dreibus, G., Kerry, K.E., Reedy, R.C., Evans, L.G., Starr, R.D., Martel, L.M.V., Squyres, S.W., Gasnault, O., Maurice, S., d'Uston, C., Englert, P., Dohm, J.M., Baker, V.R., Hamara, D., Janes, D., Sprague, A.L., Kim, K.J., Drake, D.M., McLennan, S.M. and Hahn, B.C. (2006) Variations in K/Th on Mars. Journal of Geophysical Research-Planets 111.
Taylor, G.J. and Wieczorek, M.A. (2014) Lunar bulk chemical composition: a post-Gravity Recovery and Interior Laboratory reassessment. Philosophical Transactions of the Royal Society a-Mathematical Physical and Engineering Sciences 372.
Taylor, S.R. (2001) Solar System Evolution: A new Perspective., 2nd edition ed. Cambridge University Press.
Taylor, S.R. and McLennan, S.M. (1985) The continental crust: Its composition and evolution. Blackwell Scientific Publishers, London.
Taylor, S.R. and McLennan, S.M. (2008) Planetary Crusts: Their Composition, Oigin and Evolution. Cambridge University Press.
Thomas, R.J., Hynek, B.M., Rothery, D.A. and Conway, S.J. (2016) Mercury's low-reflectance material: Constraints from hollows. Icarus 277, 455-465.
Thomas, R.J., Rothery, D.A., Conway, S.J. and Anand, M. (2014a) Hollows on Mercury: Materials and mechanisms involved in their formation. Icarus 229, 221-235.
Thomas, R.J., Rothery, D.A., Conway, S.J. and Anand, M. (2014b) Long-lived explosive volcanism on Mercury. Geophysical Research Letters 41, 6084-6092.
Thomas, R.J., Rothery, D.A., Conway, S.J. and Anand, M. (2014c) Mechanisms of explosive volcanism on Mercury: Implications from its global distribution and morphology. Journal of Geophysical Research-Planets 119, 2239-2254.
Thompson, M.S., Vander Kaaden, K.E., Loeffler, M.J. and McCubbin, F.M. (2021) Understanding the space weathering of Mercury through laboratory experiments, Proceedings of the 52nd Lunar and Planetary Science Conference. Lunar and Planetary Institute, Woodlands, TX, p. #1496.
Tonks, W.B. and Melosh, H.J. (1993) Magma ocean formation due to giant impacts. Journal of Geophysical Research-Planets 98, 5319-5333.
Udry, A., Wilbur, Z.E., Rahib, R.R., McCubbin, F.M., Vander Kaaden, K.E., McCoy, T.J., Ziegler, K., Gross, J., DeFelice, C., Combs, L. and Turrin, B.D. (2019) Reclassification of four aubrites as enstatite chondrite impact melts: Potential geochemical analogs for Mercury. Meteoritics & Planetary Science 54, 785-810.
Vander Kaaden, K.E., M. McCubbin, F., R. Nittler, L., N. Peplowski, P., Z. Weider, S., A. Frank, E. and J. McCoy, T. (2017) Geochemistry, mineralogy, and petrology of boninitic and komatiitic rocks on the mercurian surface: Insights into the mercurian mantle. Icarus 285, 155-168.
Vander Kaaden, K.E. and McCubbin, F.M. (2015) Exotic crust formation on Mercury: Consequences of a shallow, FeO-poor mantle. Journal of Geophysical Research-Planets 120, 195-209.
Vander Kaaden, K.E. and McCubbin, F.M. (2016) The origin of boninites on Mercury: An experimental study of the northern volcanic plains lavas. Geochimica Et Cosmochimica Acta 173, 246-263.
Vander Kaaden, K.E., McCubbin, F.M., Byrne, P.K., Chabot, N.L., Ernst, C.M., Johnson, C.L. and Thompson, M.S. (2019) Revolutionizing Our Understanding of the Solar System via Sample Return from Mercury. Space Science Reviews 215.
Vander Kaaden, K.E., McCubbin, F.M., Turner, A.A. and Ross, D.K. (2020) Constraints on the Abundances of Carbon and Silicon in Mercury's Core From Experiments in the Fe-Si-C System. Journal of Geophysical Research: Planets 125, e2019JE006239.
Vasavada, A.R., Paige, D.A. and Wood, S.E. (1999) Near-surface temperatures on mercury and the moon and the stability of polar ice deposits. Icarus 141, 179-193.
Vervack, R.J., Killen, R.M., McClintock, W.E., Merkel, A.W., Burger, M.H., Cassidy, T.A. and Sarantos, M. (2016) New discoveries from MESSENGER and insights into Mercury's exosphere. Geophysical Research Letters 43, 11,545-511,551.
Vervack, R.J., McClintock, W.E., Killen, R.M., Sprague, A.L., Anderson, B.J., Burger, M.H., Bradley, E.T., Mouawad, N., Solomon, S.C. and Izenberg, N.R. (2010) Mercury's Complex Exosphere: Results from MESSENGER's Third Flyby. Science 329, 672-675.

Vilas, F. (1988) Surface composition of Mercury from reflectance spectrophotometry in: Vilas, F., Chapman, C.R., Matthews, M.S. (Eds.), Mercury. The University of Arizona Press, Tucson, AZ, pp. 59-76.
Vilas, F., Domingue, D.L., Helbert, J., D'Amore, M., Maturilli, A., Klima, R.L., Stockstill-Cahill, K.R., Murchie, S.L., Izenberg, N.R., Blewett, D.T., Vaughan, W.M. and Head, J.W. (2016) Mineralogical indicators of Mercury's hollows composition in MESSENGER color observations. Geophysical Research Letters 43, 1450-1456.
Vilas, F. and McCord, T.B. (1976) Mercury: Spectral reflectance measurements (0.33–1.06 μm) 1974/1975. Icarus 28, 593-599.
Wade, J. and Wood, B.J. (2005) Core formation and the oxidation state of the Earth. Earth and Planetary Science Letters 236, 78-95.
Wade, J., Wood, B.J. and Tuff, J. (2012) Metal-silicate partitioning of Mo and W at high pressures and temperatures: evidence for late accretion of sulphur to the Earth. Geochimica et Cosmochimica Acta 85, 58-74.
Wadhwa, M. (2001) Redox state of Mars' upper mantle and crust from Eu anomalies in shergottite pyroxenes. Science 291, 1527-1530.
Wadhwa, M. (2008) Redox conditions on small bodies, the Moon, and Mars. Oxygen in the Solar System 68, 493-510.
Wallace, P. and Carmichael, I.S.E. (1992) Sulfur in Basaltic Magmas. Geochimica Et Cosmochimica Acta 56, 1863-1874.
Wänke, H. and Dreibus, G. (1994) Chemistry and Accretion History of Mars. Philosophical Transactions of the Royal Society of London Series a-Mathematical Physical and Engineering Sciences 349, 285-293.
Wasson, J. (1988) The building stones of the planets, in: Vilas, F., Chapman, C.R., Matthews, M.S. (Eds.), Mercury. University of Arizona Press, Tucson, AZ, pp. 622-650.
Weber, R.C., Lin, P.-Y., Garnero, E.J., Williams, Q. and Lognonné, P. (2011) Seismic Detection of the Lunar Core. Science 331, 309-312.
Weider, S.Z., Nittler, L.R., Murchie, S.L., Peplowski, P.N., McCoy, T.J., Kerber, L., Klimczak, C., Ernst, C.M., Goudge, T.A., Starr, R.D., Izenberg, N.R., Klima, R.L. and Solomon, S.C. (2016) Evidence from MESSENGER for sulfur- and carbon-driven explosive volcanism on Mercury. Geophysical Research Letters 43, 3653-3661.
Weider, S.Z., Nittler, L.R., Starr, R.D., Crapster-Pregont, E.J., Peplowski, P.N., Denevi, B.W., Head, J.W., Byrne, P.K., Hauck, S.A., II, Ebel, D.S. and Solomon, S.C. (2015) Evidence for geochemical terranes on Mercury: Global mapping of major elements with MESSENGER's X-Ray Spectrometer. Earth and Planetary Science Letters 416, 109-120.
Weider, S.Z., Nittler, L.R., Starr, R.D., McCoy, T.J. and Solomon, S.C. (2014) Variations in the abundance of iron on Mercury's surface from MESSENGER X-Ray Spectrometer observations. Icarus 235, 170-186.
Weider, S.Z., Nittler, L.R., Starr, R.D., McCoy, T.J., Stockstill-Cahill, K.R., Byrne, P.K., Denevi, B.W., Head, J.W. and Solomon, S.C. (2012) Chemical heterogeneity on Mercury's surface revealed by the MESSENGER X-Ray Spectrometer. Journal of Geophysical Research - Planets 117.
Weisberg, M.K. and Kimura, M. (2012) The unequilibrated enstatite chondrites. Geochemistry 72, 101-115.
Weisberg, M.K., Prinz, M., Clayton, R.N., Mayeda, T.K., Sugiura, N., Zashu, S. and Ebihara, M. (2001) A new metal-rich chondrite grouplet. Meteoritics & Planetary Science 36, 401-418.
Weisberg, M.K., Prinz, M. and Nehru, C.E. (1988) Petrology of ALH85085: a chondrite with unique characteristics. Earth and Planetary Science Letters 91, 19-32.
Wetherill, G.W. (1980) Formation of the Terrestrial Planets. Annual Review of Astronomy and Astrophysics 18, 77-113.
Wetherill, G.W. (1988) Accumulation of Mercury from planetesimals, in: Vilas, F., Chapman, C.R., Matthews, M.S. (Eds.), Mercury. University of Arizona Press, Tucson, AZ, pp. 670-691.
Wheelock, M.M., Keil, K., Floss, C., Taylor, G.J. and Crozaz, G. (1994) REE geochemistry of oldhamite-dominated clasts from the Norton County aubrite: Igneous origin of oldhamite. Geochimica et Cosmochimica Acta 58, 449-458.
Wilbur, Z.E., Udry, A., McCubbin, F.M., vander Kaaden, K.E., DeFelice, C., Ziegler, K., Ross, D.K., McCoy, T.J., Gross, J., Barnes, J.J., Dygert, N., Zeigler, R.A., Turrin, B.D. and McCoy, C. (2022) The effects of highly reduced magmatism revealed through aubrites. Meteoritics & Planetary Science 57, 1387-1420.
Wohlers, A. and Wood, B.J. (2015) A Mercury-like component of early Earth yields uranium in the core and high mantle 142Nd. Nature 520, 337-340.
Wohlers, A. and Wood, B.J. (2017) Uranium, thorium and REE partitioning into sulfide liquids: Implications for reduced S-rich bodies. Geochimica et Cosmochimica Acta 205, 226-244.

Wood, B.J. and Kiseeva, E.S. (2015) Trace element partitioning into sulfide: How lithophile elements become chalcophile and vice versa. American Mineralogist 100, 2371-2379.
Wood, B.J., Smythe, D.J. and Harrison, T. (2019) The condensation temperatures of the elements: A reappraisal. American Mineralogist 104, 844-856.
Wood, B.J., Walter, M.J. and Wade, J. (2006) Accretion of the Earth and segregation of its core. Nature 441, 825-833.
Xiao, Z., Strom, R.G., Blewett, D.T., Byrne, P.K., Solomon, S.C., Murchie, S.L., Sprague, A.L., Domingue, D.L. and Helbert, J. (2013) Dark spots on Mercury: A distinctive low-reflectance material and its relation to hollows. Journal of Geophysical Research: Planets 118, 1752-1765.
Xiao, Z., Strom, R.G., Blewett, D.T., Chapman, C.R., Denevi, B.W., Head III, J.W., Fassett, C.I., Braden, S.E., Gwinner, K., Solomon, S.C., Murchie, S.L., Watters, T.R. and Banks, M.E. (2012) The youngest geologic terrains on Mercury, Proceedings of the 43rd Lunar and Planetary Science Conference. Lunar and Planetary Institute, Woodlands, TX, p. #2143.
Yoder, C.F. (1995) Astrometric and Geodetic Properties of Earth and the Solar System, Global Earth Physics, pp. 1-31.
Zhang, J.A. and Paige, D.A. (2009) Cold-trapped organic compounds at the poles of the Moon and Mercury: Implications for origins. Geophysical Research Letters 36.
Zhang, L. and Fei, Y. (2008) Effect of Ni on Fe–FeS phase relations at high pressure and high temperature. Earth and Planetary Science Letters, 268, 212-218.
Zhang, Z., Hastings, P., Von der Handt, A., and Hirschmann, M.M. (2018) Experimental determination of carbon solubility in Fe-Ni-S melts. Geochimica et Cosmochimica Acta, 225, 66-79.
Zolotov, M.Y. (2011) On the chemistry of mantle and magmatic volatiles on Mercury. Icarus 212, 24-41.
Zolotov, M.Y., Sprague, A.L., Hauck, S.A., Nittler, L.R., Solomon, S.C. and Weider, S.Z. (2013) The redox state, FeO content, and origin of sulfur-rich magmas on Mercury. Journal of Geophysical Research-Planets 118, 138-146.
Zurbuchen, T.H., Raines, J.M., Gloeckler, G., Krimigis, S.M., Slavin, J.A., Koehn, P.L., Killen, R.M., Sprague, A.L., McNutt, R.L. and Solomon, S.C. (2008) MESSENGER Observations of the Composition of Mercury's Ionized Exosphere and Plasma Environment. Science 321, 90-92.

Figures

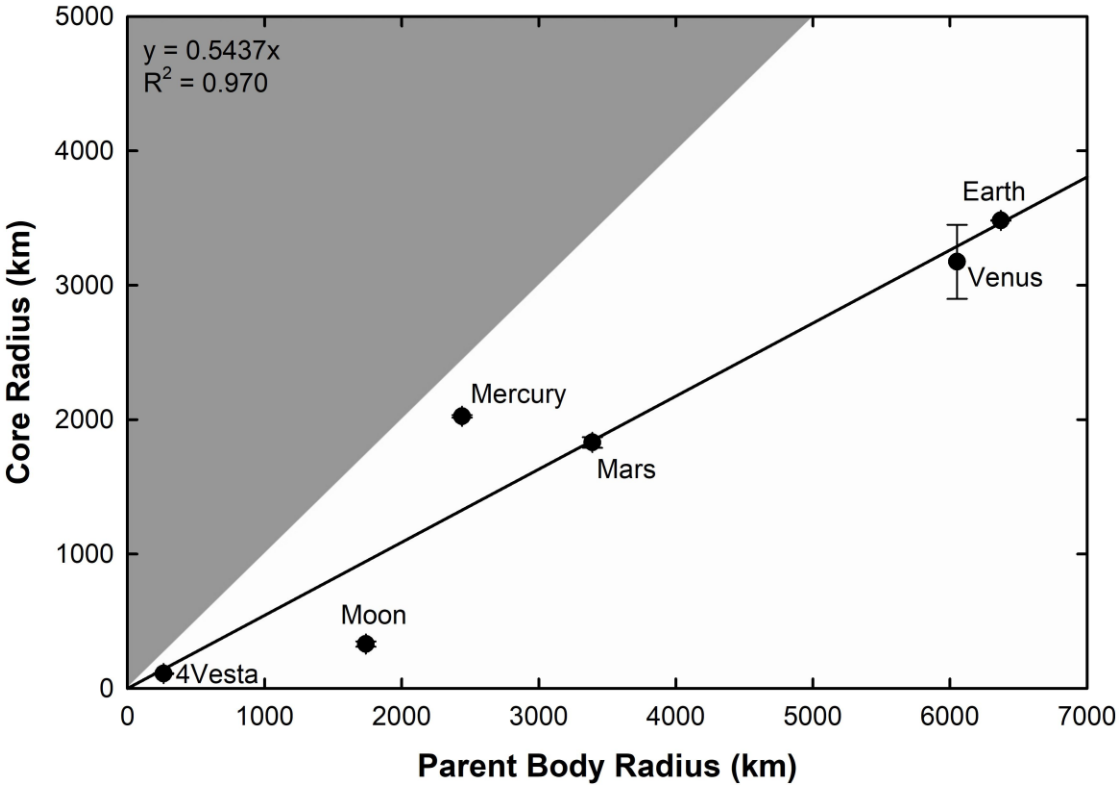

Figure 1. Core radius versus parent body radius for several terrestrial bodies from the inner Solar System. The gray shaded region of the figure shows a forbidden region where core radius would be larger than parent body radius. A line of best fit through the data and the origin is represented by the black line. The slope of the line and its R^2 are displayed in the upper left portion of the plot. Data sources for the radii of each body are as follows: Earth (Yoder, 1995), Moon (Weber et al., 2011; Yoder, 1995), Mars (Stähler et al., 2021; Yoder, 1995), Mercury (Margot et al., 2019), Venus (Dumoulin et al., 2017; Yoder, 1995), 4 Vesta (Russell et al., 2012).

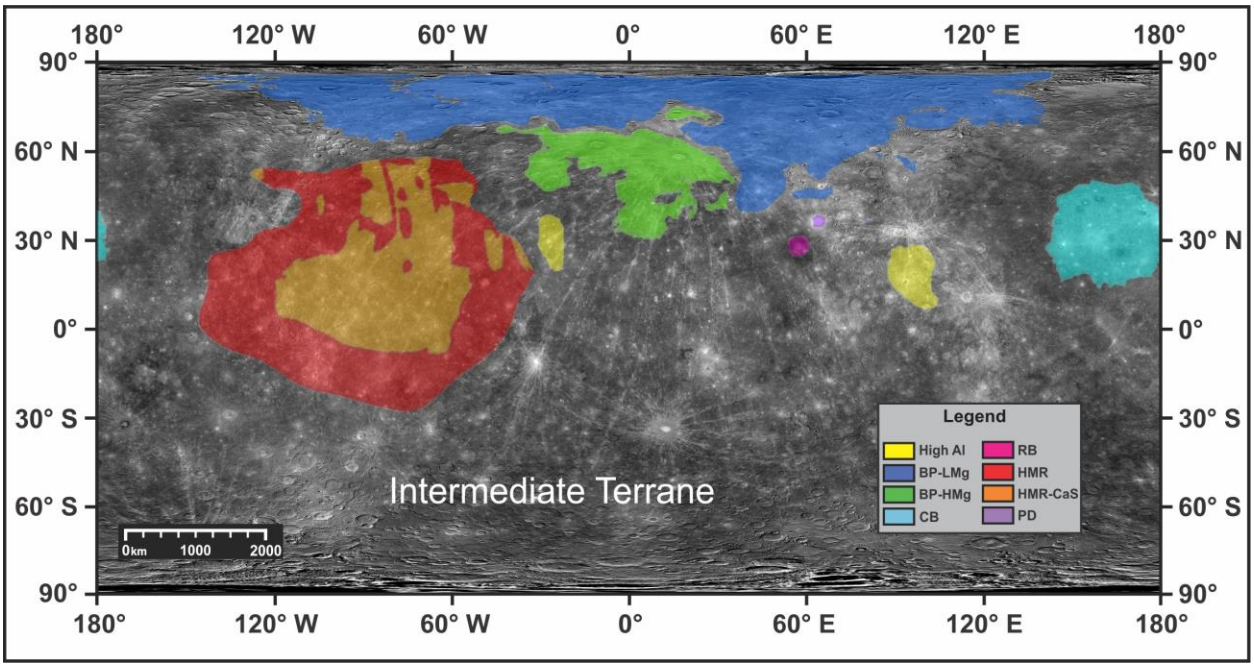

Figure 2. Map of Mercury showing nine geochemical regions, consisting of terranes and deposits, defined on the basis of MESSENGER XRS data. The locations of the regions are reported in Vander Kaaden et al. (2017). The terranes are superimposed on a low incidence angle mosaic of Mercury displayed as a simple cylindrical projection, centered on 0° latitude and 0° longitude. Image credit for mosaic: NASA/Johns Hopkins University Applied Physics Laboratory/Carnegie Institution of Washington. The region abbreviations are as follows: HMR – High-Mg Region, HMR-CaS – portion of High-Mg Region with elevated Ca and S, BP-HMg – High-Mg lavas of Borealis Planitia, BP-LMg – Low-Mg lavas of Borealis Planitia, RB – Rachmaninoff Basin, PD – Pyroclastic deposit NE of Rachmaninoff Basin, High Al – High-aluminum Plains, CB – Caloris Basin, IT – Intermediate Terrane. Scale bar is in kilometers.

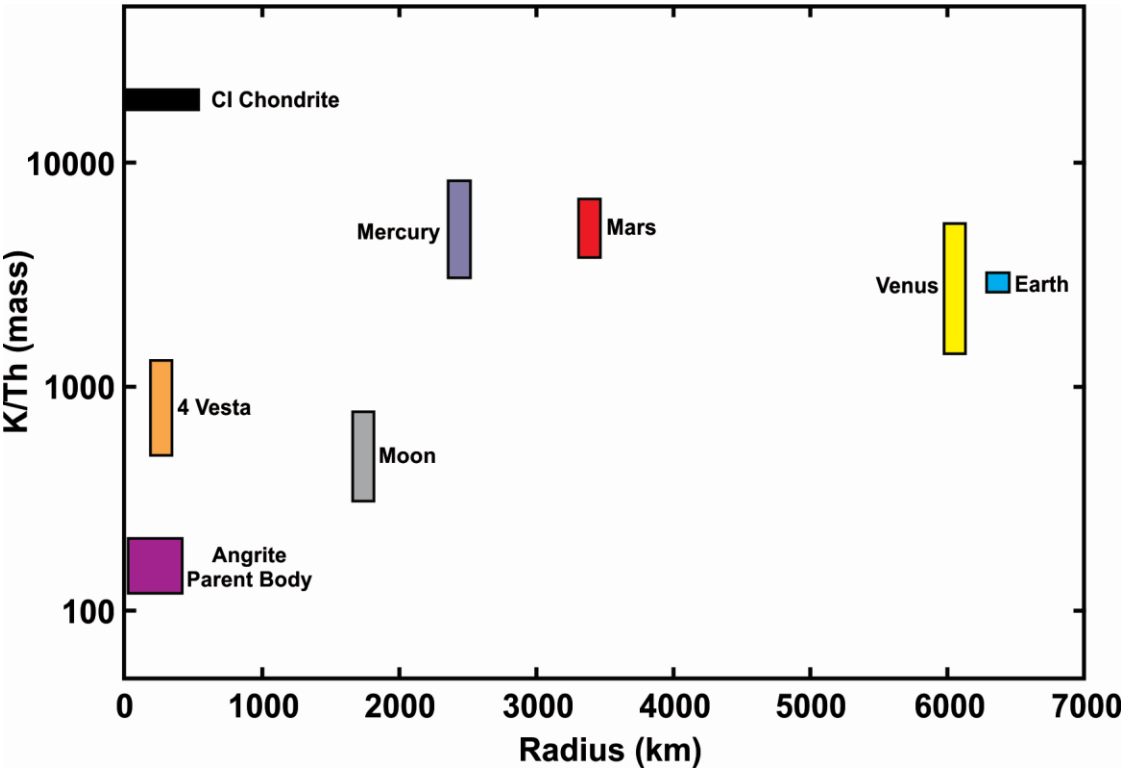

Figure 3. Bulk K/Th ratio versus mean radius (km) of parent body for Solar System bodies. The range in radius for the angrite parent body (APB) represents the range in estimates in the literature (Sarafian et al., 2014). The range in radius for the CI chondrite parent body represents a range from 0 km to the radius of Ceres (Russell et al., 2016). Parent body radius for 4 Vesta is from (Russell et al., 2012), and all other radii are from the sources identified in Figure 1. The K/Th data for each parent body are as follows: Mercury (Table 1), Angrite parent body (McCubbin and Barnes, 2019), 4 Vesta (Prettyman et al., 2015), CI chondrite (Lodders and Fegley, 1998), Mars (Determined by combining data on martian meteorites from the martian meteorite compendium wih GRS data from Taylor et al., 2006), Earth (McDonough and Sun, 1995), Moon (Lucey et al., 2006), and Venus (average of the K/Th values reported for Vanera 8, Vanera 9, Vanera 10, Vega 1, and Vega 2, as summarized by Lodders and Fegley, 1998).

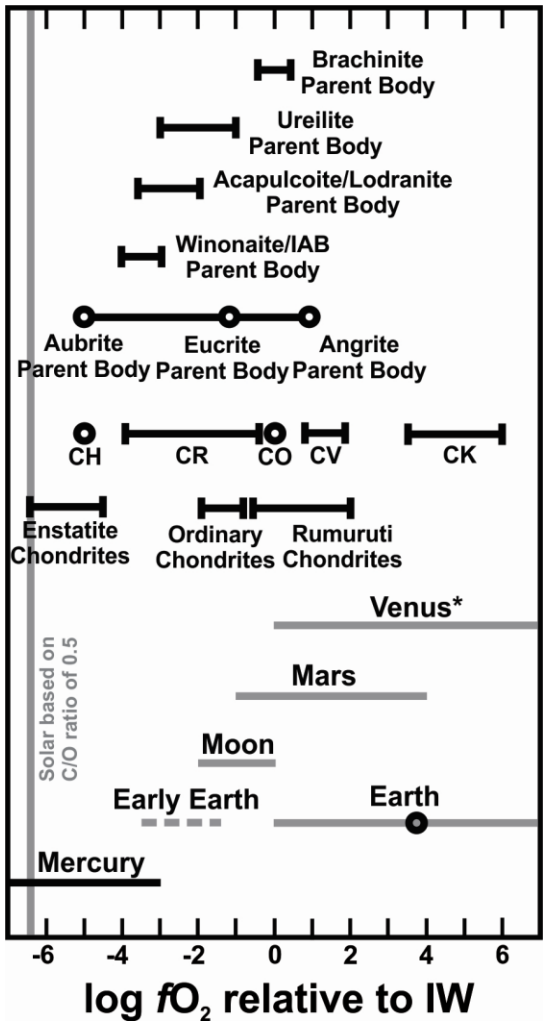

Figure 4. Plot showing the range in fO_2 exhibited by various parent bodies in the Solar System relative to the IW reaction. The absolute log fO_2 value of the IW reaction changes as a function of temperature, and the fO_2 estimates in this plot relate to the temperature ranges at which fO_2 equilibrated on each of the parent bodies. Consequently, this plot does not represent a single temperature or absolute log fO_2 value at any given point along the x-axis. Terrestrial planets and meteorites cover a range of fO_2 relative to IW (Anzures et al., in press; Benedix et al., 2005; Cartier and Wood, 2019; Ehlmann et al., 2016; Goodrich et al., 2013; McCoy et al., 2019; McCubbin and Barnes, 2019; Righter et al., 2016; Wadhwa, 2008). The fO_2 for typical magmas (MORB) on Earth is denoted by a gray circle with black outline (Cottrell and Kelley, 2011; O'Neill et al., 2018). The gray lines for Mercury, Venus, Earth, Moon, and Mars represent fO_2 ranges for their respective magmas. Low fO_2 (i.e., ≤IW–3) is observed for Mercury (McCubbin et al., 2017; Namur et al., 2016a; Zolotov et al., 2013), enstatite chondrites (Fogel et al., 1989), aubrites (Casanova et al., 1993), the winonaite/IAB parent body (Anzures et al., in press; Benedix et al., 2005), the acapulcoite-lodranite parent body (McCoy et al., 2019; Righter et al., 2016), some CR chondrites (Schrader et al., 2013), CH chondrite metal (Petaev et al., 2003), and early Earth (Javoy et al., 2010). *Venus is presumed to have the same range in magmatic fO_2 as Earth based on similar core fraction and similar FeO abundances in surface basalts (Filiberto, 2014).

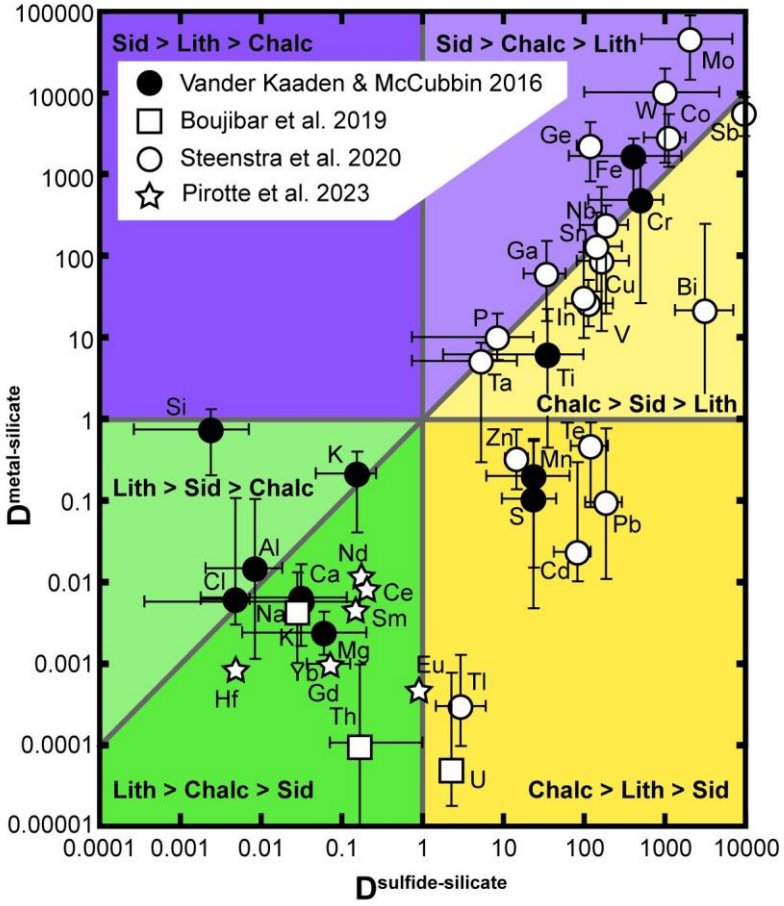

Figure 5. Partitioning of elements between metal, sulfide, and silicate melt under reducing conditions relevant to Mercury (i.e., ≤IW–3) from experimental data (Boujibar et al., 2019; Pirotte et al., 2023; Steenstra et al., 2020b; Vander Kaaden and McCubbin, 2016). The symbol for each element is the average D value reported in each study, and the error bars represent the maximum and minimum D values from all experimental charges. The affinity of an element is depicted by the region of the graph in which it falls. Sid: Siderophile (purple), Lith: Lithophile (green), Chalc: Chalcophile (yellow).

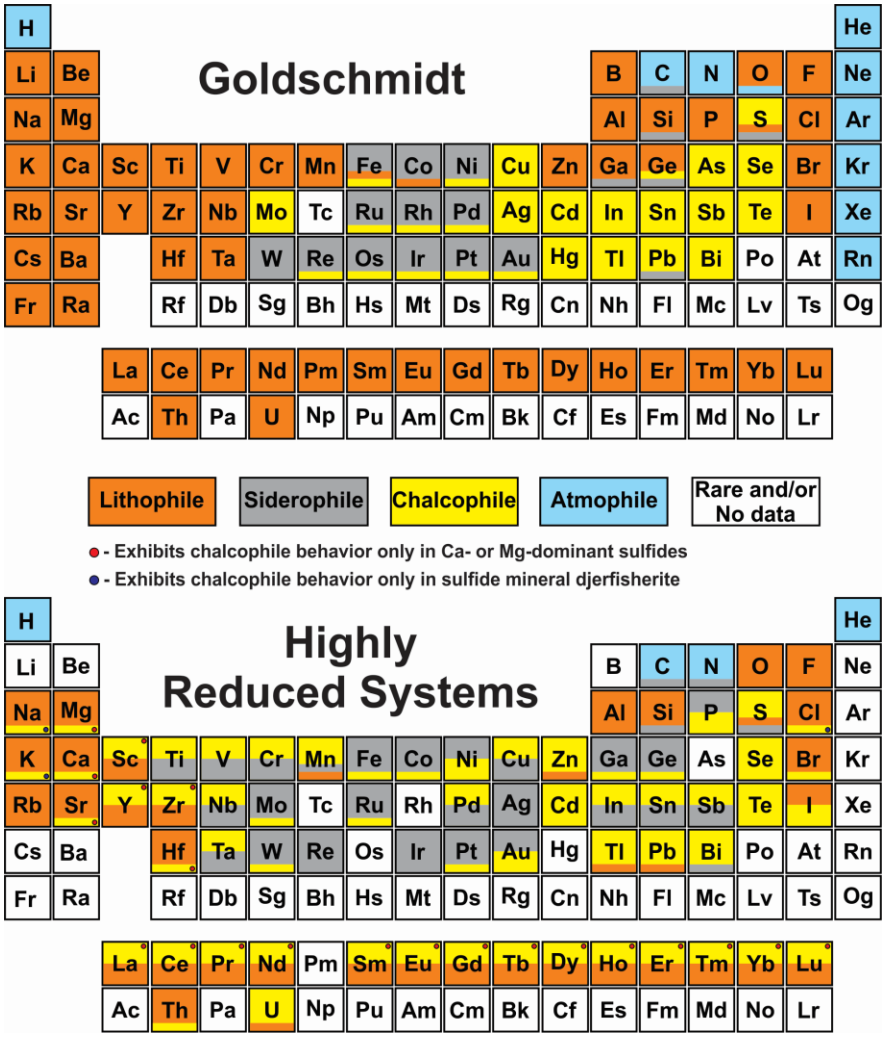

Figure 6. Geochemical classification of element affinity developed from (Top) distributions of elements in Earth rocks and meteorites based on original classifications from Goldschmidt (Goldschmidt, 1937; Lee, 2018) and (bottom) from experimental partitioning studies of elements among metal, sulfide, and silicate phases (Boujibar et al., 2019; Jackson et al., 2018; Pirotte et al., 2023; Steenstra et al., 2022; Steenstra et al., 2020a,c; Vander Kaaden and McCubbin, 2016; Wohlers and Wood, 2015, 2017) as well as the distributions of elements amongst sulfides, silicates, oxides, and metals in highly reduced meteorites (Crozaz and Lundberg 1995; Dickinson and McCoy, 1997; Floss and Crozaz, 1993; Keil, 2010; Lodders et al., 1993; Udry et al., 2019; Weisberg and Kimura, 2012; Wheelock et al., 1994; Wilbur et al., 2022). The geochemical affinity is indicated by color as labelled between the upper and lower periodic tables and listed here as lithophile (orange), siderophile (gray), chalcophile (yellow), atmophile (blue), and rare and/or no data (white). For element boxes with two or more colors, the dominant area represents the primary affinity, and the minor areas represent minor affinities. Element boxes filled with approximately equal area of two colors indicates that the element has dual affinities. Red or blue circles indicate elements that only exhibit chalcophile behavior in Ca- and/or Mg-dominant sulfides (red circles) or that only exhibit chalcophile behavior in the sulfide mineral djerfisherite (blue circles), respectively.

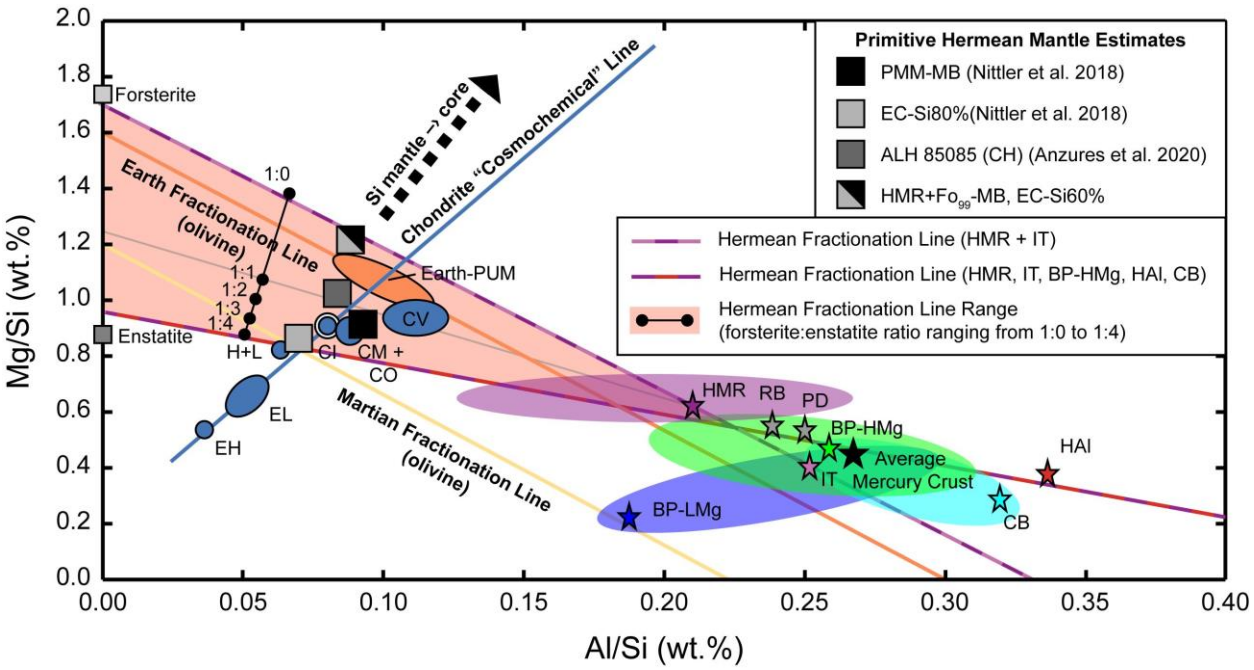

Figure 7. Plot of Al/Si vs. Mg/Si showing bulk chemical fractionation lines for Earth (Drake and Righter, 2002), Mars (Wänke and Dreibus, 1994), and Mercury (after Anzures et al., 2020; this study) used to determine the initial bulk silicate composition of a terrestrial planet. Several potential Mercury fractionation lines are shown that correspond to olivine:pyroxene ratios ranging from 1:0 to 1:4. Different geochemical terrains on the surface are shown in colored fields (Weider et al., 2015), and terrane compositions from Tables 1–2 are shown as star symbols. Model bulk silicate compositions of Mercury from Table 4 are shown as square symbols. In Al/Si vs. Mg/Si space, chondrites form a linear trend that represents the chemically primitive building blocks of the Solar System (Taylor, 2001). The bulk silicate composition is then determined as the intersection between the bulk fractionation line and the chondrite line, where higher Mg/Si ratio identifies more primitive magmatic compositions. For Earth, this primitive upper mantle composition agrees well with a fractionation line through primitive ultramafic rocks with primarily olivine fractionation (Jagoutz et al., 1979; Palme and Nickel, 1985; Ringwood, 1979).

Tables

Table 1. Global average surface composition of Mercury[†] from MESSENGER XRS and GRS data.

Element (ratio)	XRS	GRS[‡]	Oxide	Average Surface[⁑] (wt%)
Mg/Si	0.436 (0.106)		SiO_2	52.99
Al/Si	0.268 (0.048)	$0.29^{+0.05}_{-0.13}$	TiO_2	0.34
Ca/Si	0.165 (0.030)	0.24 ± 0.05	Al_2O_3	13.06
Fe/Si	0.053 (0.013)	0.077 ± 0.013	Cr_2O_3	0.03
Mn/Si	0.004 (0.001)		FeO	2.18
Ti/Si	0.0083 (0.0040)		MnO	0.12
Cr/Si	0.0008 (0.0002)		MgO	17.90
Na/Si		0.12 ± 0.01	CaO	6.67
S/Si	0.076 (0.019)	0.092 ± 0.015	Na_2O	4.01
Cl/Si		0.0057 ± 0.0010	K_2O	0.15
O/Si		1.2 ± 0.1	S	2.08
K (ppm)		1288 ± 234	Cl	0.14
Th (ppm)		0.155 ± 0.054	C	1.4
U (ppb)		90 ± 20	-O = Cl + S	1.07
C (wt%)		1.4 ± 0.9	Total	100.00

[†]All ratios are by mass. Parenthetical numbers represent the standard deviation of XRS measurements, which represent abundance variation across the surface; Values after the ± symbol refer to the 1σ statistical uncertainty.

[‡]All GRS data are from the northern hemisphere.

[⁑]Average surface compositions computed on the basis of 25 wt% Si on the surface as reported by Evans et al. (2012). For elements with both XRS and GRS values, an average was computed from both values with the exception of Ca, where the value was chosen on the basis of the midpoint in overlapping values when taking into account uncertainty (i.e., Ca/Si = 0.1925).

Values reported here from Cartier et al., 2020, Nittler et al., 2023, and Nittler et al. 2018. The data in Nittler et al. 2018 were compiled from Nittler et al., (2011, 2016); Peplowski et al. (2011, 2012b, 2014, 2015a, 2016); Evans et al. (2012, 2015); Weider et al. (2014, 2015); Frank et al. (2015); and McCubbin et al. (2017)

Table 2. Average compositions† (wt%) for eight distinct geochemical regions on Mercury based on the terranes and deposits identified in Figure 2 (Vander Kaaden et al 2017; Peplowski and Stockstill-Cahill, 2019; Weider et al., 2015).

	HMR	BP-HMg	BP-LMg	RB	PD	HAl	CB	IT
SiO_2	51.05	54.99	62.38	53.25	53.07	55.24	58.72	56.56
TiO_2	0.00	0.00	0.00	0.00	0.00	0.00	0.46	0.00
Al_2O_3	9.44	12.61	10.33	11.20	11.72	16.42	16.58	12.59
FeO	2.11	2.01	1.97	1.95	1.98	1.48	1.02	1.96
MgO	24.84	20.17	11.22	22.62	21.81	16.36	12.89	18.29
CaO	7.47	5.49	5.86	6.25	7.46	5.75	5.73	5.87
Na_2O	3.52	3.67	7.07	3.63	3.51	3.67	3.79	3.74
K_2O	0.16	0.18	0.20	0.15	0.16	0.11	0.09	0.15
S	2.83	1.80	1.99	1.92	0.57	1.97	1.45	1.71
-O=S	1.41	0.90	0.99	0.96	0.28	0.98	0.72	0.85
Total	100.00	100.00	100.00	100.00	100.00	100.00	100.00	100.00

†Compositions of each deposit or terrane is based on average composition between similar regions reported in Vander Kaaden et al., (2017) and Peplowski and Stockstill-Cahill (2019). See Vander Kaaden et al., (2017) and Peplowski and Stockstill-Cahill (2019) for information about the uncertainties on these terrane and deposit compositions.

Terrane abbreviations as follows: HMR – High-Mg Region (includes HMR and HMR-CaS from Figure 2), BP-HMg – High-Mg lavas of Borealis Planitia, BP-LMg – Low-Mg lavas of Borealis Planitia, RB – Rachmaninoff Basin, PD – Pyroclastic deposit NE of Rachmaninoff Basin, Hal – High-aluminum Plains, CB – Caloris Basin, IT – Intermediate Terrane

Table 3. Estimated elemental abundances (wt%) in Mercury's core

Basis of model estimate	Fe	Ni[a]	Co	Cr	Mn	P	Ti	Si	S	C
Geophysical Models[1]	75–95	4.3–5.5	-	-	-	-	-	>0–17	0–20	-
Graphite Flotation Crust[2]	-	-	-	-	-	-	-	-	-	>0
Metal-rich chondrite differentiation[3]	75–89	4.3–5.1	-	-	-	-	-	>5	~1–15	-
Core Formation Experiments[4]	75–83	4.3–4.8	-	-	-	-	-	>1	0–20	-
S solubility experiments[5]	-	-	-	-	-	-	-	>0	<1.5	-
Core-dynamo[6] simulations	-	-	-	-	-	-	-	<7.5		
Fe-Si-C experiments[7]	61–94	3.6–5.5	-	-	-	-	-	0.3–25	≤5.0	≤5.0
HMR+Fo_{99}-MB[8]	81–87	4.7–5.1	0.22–0.24	0.94–1.0	0.02	0.37–0.40	0.05	5.0	0–4.0	0.8–4.0

[a]Value assumed on the basis of a chondritic Fe/Ni ratio of ~17.3 (Lodders and Fegley, 1998).
Data sources: 1) Hauck et al. (2013) 2) Vander Kaaden and McCubbin (2015) 3) Malavergne et al., (2010) 4) Chabot et al (2014b) 5) Namur et al (2016a) 6) Knibbe et al. (2021) 7) Vander Kaaden et al., (2020) 8) This study with Co, Cr, Mn, Ti, and P computed using chondritic ratios with Fe and $D^{metal/Silicate}$ values from Steenstra et al., (2020b), Si assumed to be 5 wt% for bulk silicate model (see Table 4), C and S ranges are from Vander Kaaden et al., (2020), and Fe and Ni computed by difference assuming a chondritic Fe/Ni ratio.

Table 4. Model bulk silicate compositions for Mercury†

Oxide	PMM-MB	EC-Si80%	CH	HMR+Fo_{99}-MB	EC-Si60%
SiO_2	53.10	55.75	51.42	45.97	47.13
TiO_2	0.23	0.19	0.21	0.03	0.18
Al_2O_3	4.43	3.45	3.79	3.63	3.69
FeO	0.03	0.00	0.54	1.40	0.00
MnO	-	-	0.09	0.01	-
MgO	37.46	37.20	40.80	43.83	44.53
CaO	3.07	1.84	2.74	3.18	2.79
Na_2O	1.64	1.43	0.40	1.29	1.52
K_2O	0.05	0.14	0.02	0.06	0.16
S	-	-	-	0.94	-
Cl	-	-	-	0.05	-
C	-	-	-	0.11	-
-O=S+Cl	-	-	-	0.48	-
Total	100.00	100.00	100.00	100.00	100.00
Mg/Si	0.910	0.861	1.024	1.23	1.219
Al/Si	0.094	0.070	0.083	0.089	0.089
Ca/Si	0.088	0.050	0.081	0.106	0.090
Na/Si	0.049	0.041	0.012	0.044	0.051
Si in Core[1] MB	~1.5	1.46	0.38‡	5	2.84
Si in Core[2] MB	~3.5	3.43	0.89	-	6.64

[1]Assuming chondritic Si and 74% core mass fraction is a primordial feature
[2]Assuming chondritic Si and 74% core mass fraction is from large impact(s) and original core was 40% planet mass, similar to other terrestrial planets (Anderson et al., 1987)
†PMM-MB from Nittler et al., (2018) based on mass balance and experiments from Namur et al., (2016b); EC-Si80% from Nittler et al., (2018) based on enstatite chondrite composition with 20% of total SiO_2 reduced to Si and sequestered in the core; CH from Anzures et al. (2020) based on bulk silicate portion of CH chondrite ALH 85085; HMR+Fo_{99}-MB from this study based on HMR upper mantle, 5% Si in core, and chondritic Si; EC-Si60% from this study based on enstatite chondrite composition with 40% of total SiO_2 reduced to Si and sequestered in the core.
‡Computed based on average of 41 analyses of Si in metal in ALH 85085 where 38 of them yielded Si abundances below detection and 3 analyses were reported to have 3.3, 4.8, and 7.5 wt.% Si, respectively (Weisberg et al., 1988).